Astronomy & Astrophysics manuscript no. survey
March 26, 2020

Exocomets: A spectroscopic survey

I. Rebollido[1], C. Eiroa[1,2], B. Montesinos[3], J. Maldonado[4], E. Villaver[1], O. Absil[5], A. Bayo[6,7], H. Canovas[8], A. Carmona[9], Ch. Chen[10], S. Ertel[11], Th. Henning[12], D. P. Iglesias[6,7], R. Launhardt[12], R. Liseau[13], G. Meeus[1], A. Moór[14,15], A. Mora[16], J. Olofsson[6,7], G. Rauw[5], and P. Riviere-Marichalar[17]

[1] Dpto. Física Teórica, Universidad Autónoma de Madrid, Cantoblanco,28049 Madrid, Spain, e-mail: isabel.rebollido@uam.es
[2] Observatorio Astrónomico de Calar Alto, CAHA, 04550 Gérgal, Almería, Spain
[3] Centro de Astrobiología (CAB, CSIC-INTA), ESAC Campus Camino Bajo del Castillo, s/n, Villanueva de la Cañada, 28692, Madrid, Spain
[4] INAF, Osservatorio Astronomico di Palermo, Piazza del Parlamento 1, 90134 Palermo, Italy
[5] STAR Institute, Université de Liège, F.R.S.-FNRS, 19c Allée du Six Août, B-4000 Liège, Belgium
[6] Instituto de Física y Astronomía, Facultad de Ciencias, Universidad de Valparaíso, 5030 Casilla, Valparaíso, Chile
[7] Núcleo Milenio de Formación Planetaria - NPF, Universidad de Valparaíso, Av. Gran Bretaña 1111, Valparaíso, Chile
[8] European Space Astronomy Centre (ESA), PO Box, 78, 28691 Villanueva de la Cañada, Madrid, Spain
[9] Université de Toulouse, UPS-OMP, IRAP, Toulouse F-31400, France
[10] Space Telescope Science Institute, 3700 San Martin Drive, Baltimore, MD 21212, USA
[11] Steward Observatory, Department of Astronomy, University of Arizona, Tucson, AZ 85721, USA
[12] Max-Planck-Institut für Astronomie (MPIA), Königstuhl 17, D-69117 Heidelberg, Germany
[13] Department of Space, Earth and Environment, Chalmers University of Technology, Onsala Space Observatory, 439 92 Onsala, Sweden
[14] Konkoly Observatory, Research Centre for Astronomy and Earth Sciences, Konkoly-Thege Miklós út 15-17, 1121 Budapest, Hungary
[15] ELTE Eötvös Loránd University, Institute of Physics, Pázmány Péter sétány 1/A, 1117 Budapest, Hungary
[16] Aurora Technology B.V. for ESA, ESA-ESAC, Villanueva de la Cañada, 28691, Madrid, Spain
[17] Observatorio Astronómico Nacional (OAN-IGN)-Observatorio de Madrid, Alfonso XII, 3, 28014 Madrid, Spain

ABSTRACT

Context. While exoplanets are now routinely detected, the detection of small bodies in extrasolar systems remains challenging. Since the discovery of sporadic events interpreted as exocomets (Falling Evaporating Bodies) around β Pic in the early 80s, only ∼20 stars have been reported to host exocomet-like events.

Aims. We aim to expand the sample of known exocomet-host stars, as well as to monitor the hot-gas environment around stars with previously known exocometary activity.

Methods. We have obtained high-resolution optical spectra of a heterogeneous sample of 117 main-sequence stars in the spectral type range from B8 to G8. The data have been collected in 14 observing campaigns expanding over 2 years from both hemispheres. We have analysed the Ca ii K&H and Na i D lines in order to search for non-photospheric absorptions originated in the circumstellar environment, and for variable events that could be caused by outgassing of exocomet-like bodies.

Results. We have detected non-photospheric absorptions towards 50% of the sample, attributing a circumstellar origin to half of the detections (i.e. 26% of the sample). Hot circumstellar gas is detected in the metallic lines inspected via narrow stable absorptions, and/or variable blue-/red-shifted absorption events. Such variable events were found in 18 stars in the Ca ii and/or Na i lines; 6 of them are reported in the context of this work for the first time. In some cases the variations we report in the Ca ii K line are similar to those observed in β Pic. While we do not find a significant trend with the age or location of the stars, we do find that the probability of finding CS gas in stars with larger $v \sin i$ is higher. We also find a weak trend with the presence of near-infrared excess, and with anomalous (λ Boo-like) abundances, but this would require confirmation by expanding the sample.

Key words. stars: general - planetary systems - comets:general - ISM: clouds - circumstellar matter

1. Introduction

Main sequence (MS) stars are known to host a complex circumstellar (CS) environment populated by a plethora of planets, debris discs, and minor bodies, inherited from the physics that regulates the formation of stars. Later, the mutual dynamical interaction among those bodies and their host stars determines the evolution of the planetary systems.

Since the discovery of a giant planet orbiting the solar-type star 51 Peg (Mayor & Queloz 1995), thousands of planets have been detected, which make up planetary systems with diversified architectures (see e.g. The Extrasolar Planets Encyclopaedia[1]). Minor bodies, such as asteroids and comets, are expected in these planetary systems. Their study is relevant as they provide clues for understanding the formation and dynamical evolution of planetary systems (e.g. Armitage 2010). However, evidences of their presence are practically limited to indirect observations, such as the detection of circumstellar dust and gas in debris discs and, to a considerable less extent, to more direct evidences such as observations of some metallic line absorptions.

[1] exoplanet.eu

Hundreds of debris discs are currently known to surround MS stars across practically all spectral types, and ages from around 10 Myr to several Gyr. Debris discs are detected as thermal emission at mid-/far-IR/(sub-)mm wavelengths, as well as scattered light in the optical and near-IR, from small dust particles, which are mainly originated in collisions among km-sized planetesimals and other destructive processes (e.g Matthews et al. 2014, and references therein). It has been suggested that at least a fraction of debris discs posseses both warm (T $\sim$ 200 K) and cold (T $\lesssim$ 100 K) dust belts (e.g. Ballering et al. 2013; Chen et al. 2014; Kennedy & Wyatt 2014; Pawellek et al. 2014; Morales et al. 2016), reminiscent of the Solar asteroid and Kuiper belts respectively. The two-belt structure could be created by a chain of planets, while comets scattered by those planets could constitute a relevant source feeding the warm exozodiacal belt (Schüppler et al. 2016; Geiler & Krivov 2017; Marino et al. 2018). In our own solar system cometary material from Jupiter family comets is responsible for replenishing the zodiacal cloud (Nesvorný et al. 2010).

Interferometric studies (Absil et al. 2006, 2013; Ertel et al. 2014; Nuñez et al. 2017) have revealed near-IR excesses also attributed in most cases to the combination of thermal emission and scattered light from small submicron-sized, hot (T $\sim$ 1500-2000 K) dust particles located within $\sim$ 0.01 - 1 AU from the stars (depending on the luminosity, see Kirchschlager et al. 2017), very close to the dust sublimation zone. Again, cometary bodies scattered inwards from an outer reservoir is a likely scenario for the origin and persistence of the hot dust (Beust & Morbidelli 2000; Thébault & Beust 2001; Bonsor et al. 2014; Marboeuf et al. 2016; Faramaz et al. 2017; Marino et al. 2018; Sezestre et al. 2019).

Significant amounts of cold gas at several tens AU from the central stars (most young A-type stars) have been detected around $\sim$ 20 bright debris discs (e.g. Moór et al. 2015a, 2017; Riviere-Marichalar et al. 2012, 2014; Roberge et al. 2013; Greaves et al. 2016; Lieman-Sifry et al. 2016; Marino et al. 2016).

The cold gas most likely has a secondary origin (e.g. Marino et al. 2016; Matrà et al. 2017; Kral et al. 2019), but in some cases a remnant of the primordial protoplanetary disc has been suggested (Kóspál et al. 2013; Moór et al. 2015a; Kral et al. 2017). A variety of physical processes, including outgassing of cometary objects, have been invoked to explain the secondary cold gas, all of them related to the presence of planetesimals (e.g. Matthews et al. 2014, and references therein). In parallel, UV/optical high resolution spectroscopy reveals non-photospheric stable absorption features of elements such as C, O, Ca, Na or Fe at or close to the radial velocity of the star, as well as weak sporadic red- or blue-shifted absorption events with respect to the stellar radial velocity (Vidal-Madjar et al. 1994, 2017; Lagrange et al. 1998; Brandeker et al. 2004; Roberge et al. 2006; Iglesias et al. 2018; Rebollido et al. 2018). This gas would be hot with temperatures $\sim$ 1000 – 2000 K (Hobbs et al. 1988; Beust et al. 1998; Vidal-Madjar et al. 2017). The transient absorptions have been interpreted as hot gas released by the evaporation of exocomets grazing or falling onto the star, the "Falling Evaporating Bodies" scenario or FEBs (e.g. Ferlet et al. 1987; Beust et al. 1990), while additionally grain evaporation in the circumstellar disc has also been proposed to explain the stable absorption components (e.g. Fernández et al. 2006). A trend between the detection of this hot gas and the edge-on orientation of cold-gas-bearing debris discs has been found by Rebollido et al. (2018), who attributed it to a geometrical effect. It is remarkable that this hot gas would be located at distances $\lesssim$ 0.5 AU from the star, i.e., at similar distances as the hot exozodiacal dust.

The first direct evidence for the presence of exocomets (FEBs) was found around β Pic, which remains unique and the best studied theoretically and observationally (e.g. Ferlet et al. 1987; Beust et al. 1991; Kiefer et al. 2014b; Vidal-Madjar et al. 2017, and references therein). Several hundreds of cometary transits in β Pic have been detected, revealing two families of exocomets with distinct dynamical and compositional properties; one likely formed by old comets strongly depleted in volatiles, and a second one related to the recent fragmentation of one or few parent bodies (Kiefer et al. 2014b). It is worth to note that very recently β Pic transiting exocomets have likely been detected by means of *TESS* broadband photometry (Zieba et al. 2019). Those exocomets would have been driven into the vicinity of the star by a larger body, i.e., a planet (Beust et al. 1991; Beust & Morbidelli 2000). Thus, FEBs constitute an indicator of the plausible presence of planets; we recall that the Jupiter-like planet β Pic b, was later revealed by imaging (Lagrange et al. 2010).

In addition to β Pic, absorption events, mainly in the Ca II K line accompanied in most cases by a stable component, have been detected towards more than 20 stars (e.g. Redfield 2007; Kiefer et al. 2014a; Welsh & Montgomery 2015, 2018). Those stars are usually young (< 100 Myr) A-type stars, but transient features have also been found around older stars. Also, Welsh & Montgomery (2019) have recently reported the first detection of an exocomet-like event with a 2.9σ signal around the F2 V type star η Crv. In addition, *Kepler* photometric light curves have been explained as due to transiting exocomets in a few F- and later spectral type stars (Rappaport et al. 2018; Ansdell et al. 2019) and maybe Boyajian's star (Boyajian et al. 2016). Exocomet-host stars have large projected rotational velocities, most with $v \sin i \gtrsim$100 km/s, in principle suggesting that the systems are viewed close to edge-on, which is the favoured orientation to detect non-photospheric absorptions from comet-like bodies passing in front of the star, and consistent with the trend suggested by Rebollido et al. (2018). In some cases, the stars hosting exocomets are associated with a debris disc. We note, however, that scattering of exocomets by eccentric planets can take place in planetary systems with low luminous, non-detectable debris discs with flux levels comparable to the Kuiper belt (Faramaz et al. 2017).

This work presents the observational results of a high spectral resolution survey of a large sample of stars with the primary aim of detecting and monitoring non-photospheric absorption features due to the passing of exocomets in front of the stars, and as secondary goal to assess any potential trend between the presence of exocomets and the properties of the host stars. The paper is structured as follows. Section 2 describes the sample of stars, the criteria to select them, and some basic properties. Section 3 presents our spectroscopic observations and data analysis. Section 4 presents our spectroscopic results concerning non-photospheric stable and variable features, their plausible interstellar (ISM) or circumstellar (CS) origin, and comments to some individual stars. Section 5 discusses the detection of the non-photospheric absorptions regarding some stellar properties, as well as with respect to the selection criteria. Finally, Section 6 presents the conclusions of this work.

2. Sample

As mentioned above the primary goals of our study are the detection and monitoring of variable, non-photospheric absorption features that, as in the case of β Pic, could be attributed to the evaporation of solid bodies in the immediate surroundings of main-sequence stars. The observed stellar sample is formed by a heterogeneous and biased set of 117 MS stars in the spectral type range from B8 to G8, aiming at optimising those goals. The targets have been selected according to the following criteria: i) stars with previously reported Ca ii H&K and/or Na i D events attributed to exocomets; ii) debris disc stars, seen edge-on when known; iii) debris disc stars where the presence of cold gas has been detected at far-IR and (sub-)mm wavelengths; iv) stars with near-IR excesses that could be due to hot dust; v) stars belonging to young associations, namely Upper Scorpius (UpSco), Tucana-Horologium (Tuc-Hor), and the β Pictoris moving group (BPMG); vi) shell stars with circumstellar Ti ii absorptions; vii) λ Bootis stars. The Ti ii stars have been selected because those lines denote the presence of discs seen at nearly right angles to the rotational axes (Abt & Moyd 1973; Abt et al. 1997), i.e. hot discs seen near edge-on - we note that in general shell stars are a heterogenous group of late B- to early F-type with the distinct characteristic of enhanced lines of Fe ii and Ti ii denoting the presence of a gaseous circumstellar shell (Gray & Corbally 2009, and references therein). In addition, λ Bootis stars are A and early F spectral type stars strongly depleted in heavier elements (such as Fe, Al, Mg, Ca...), and relatively normal abundances of volatile elements like C, N, O, and S (Paunzen 2004), and some of them show clear evidences of accreting CS gas in their UV/optical spectra (Grady et al. 1996a; Holweger et al. 1999). The λ Bootis abundance pattern is most likely due to selective accretion of the volatile elements onto the star, material that could be provided by exocomets, although other sources could also be an alternative (Jura 2015; Draper et al. 2016). We note that some stars in the sample share several of the selection criteria.

Table B.1 lists the observed stars. Columns 1 to 9 provide HD number, other names, 2000.0 equatorial coordinates, spectral types, distances, apparent V-magnitudes, $B-V$ colour indexes, and radial velocities v_{rad}, all taken from SIMBAD (Wenger et al. 2000). In addition, column 10 gives ages; column 11 gives the fractional luminosity of the dust, L_{IR}/L_{star}, for those stars where a debris disc has been detected; column 12 gives the corresponding stellar association; and column 13 gives the primary selection criteria. The corresponding references for columns 10-13 are given within brackets. Fig. 1 shows the spatial distribution of the sample in galactic coordinates. Given the characteristics of the selection criteria, there is no preferencial location with the exception of stars in the UpSco and Tuc-Hor young associations, although most stars are in the Southern Hemisphere.

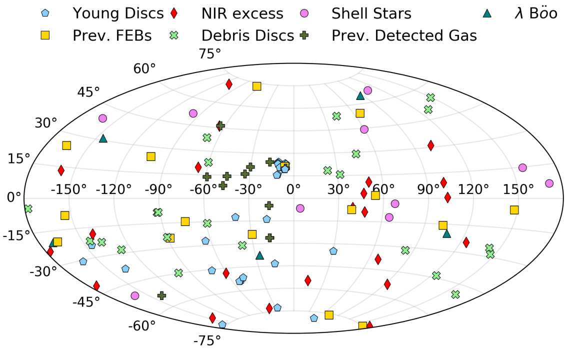

Fig. 1: All sky plot of the sample in galactic coordinates. Although most stars are in the Southern Hemisphere, there is no preferential spatial location, with the exception of stars in the UpSco and Tuc-Hor young associations.

3. Observations and data analysis

High-resolution observations were taken in a series of campaigns from August 2015 to September 2017 from both the Northern and Southern hemispheres, using different fiber-fed spectrographs and telescopes. The spectrographs HERMES (Raskin et al. 2011) attached at the 1.5 m Mercator Telescope, and FIES (Frandsen & Lindberg 2000) at the 2.5 m Nordic Optical Telescope (NOT) were used in El Roque de los Muchachos Observatory (Canary Islands, Spain). In La Silla Observatory (Chile), the FEROS spectrograph (Kaufer et al. 1999) at the MPG/ESO 2.2 telescope was used. Complementary observations were obtained at La Luz Observatory (México) with the TIGRE telescope and the HEROS spectrograph (Schmitt et al. 2014). Table 1 summarizes the resolutions and wavelength ranges of the various instruments, and the observing campaigns. A total of 1575 spectra for the 117 stars were obtained; a detailed observing log with the specific dates (UT) of the spectra for each star and the corresponding spectrograph is given in the Appendix in Table C.1. Due to the nature of the irregular, sporadic exocometary-like events, we aimed at obtaining time-series spectra, with at least one spectrum per night per object when possible. Integration times never exceeded 30 minutes and were mainly selected depending on the telescope and brightness of the star with the general goal of obtaining a S/N ratio $\gtrsim 100$ in the Ca ii H&K lines. That goal was not always achieved due to either poor weather conditions or the faintness of the star. Signal to noise (S/N) of the median spectra for each star measured in the continuum close to Ca ii K line is given in Table C.1.

Data reduction was performed by the available pipelines of the different spectrographs. The reduction includes the usual steps for echelle spectra as bias subtraction, flat-field correction, cosmic ray removal, and order extraction; wavelength calibration is carried out by means of Th-Ar lamp spectra. In addition, barycentric corrections for the HERMES and FIES spectra were carried out as the corresponding pipelines do not include such correction. All spectra were normalised and the continuum set to 1.0 in the regions between spectral lines.

3.1. Telluric subtraction

The observed wavelength range includes regions of the visible spectra heavily affected by telluric lines; in particular the region around the 5890/5896 Å Na i D lines, which are highly relevant for both interstellar and circumstellar absorptions. Removal of telluric lines was performed by means of MOLECFIT[2](Smette et al. 2015, Kausch et al. 2015), a tool that generates an atmosphere model accounting for the most common absorbing molecules in the optical range (H_2O, O_2, O_3). Residuals after subtraction of the atmosphere model in the telluric line region are comparable to the noise level, and therefore negligible. An example of telluric subtraction is shown in Fig. 2.

3.2. Stellar parameters

Stellar parameters $T_{\rm eff}$, $\log g$ and $v \sin i$ for the early type stars (up to F2) in the sample were computed using the procedure described by Rebollido et al. (2018). Solar abundances were used

[2] http://www.eso.org/sci/software/pipelines/skytools/molect

Table 1: Instruments and observing campaings.

	HERMES	FIES	FEROS	HEROS[!]
Resolution	~ 85000	~ 67000	~ 48000	~ 20000
Range (nm)	377-900	364-736	352-920	374-884
Observations	03-06/Sep/2015	26-27/Jan/2016	21-24/Oct/2015	Aug 2015
	20-23/Dec/2015	16-19/Jul/2016	25-28/Mar/2016	Sept 2015
	27-30/Jan/2016	03/Mar/2016*	31/Mar-08/Apr/2017	Oct 2015
	03-06/Mar/2016	21/Mar/2016*	23/Sep-01/Oct/2017	Nov 2015
	08-11/May/2016			Dec 2015
	11-14/Jul/2016			Jan 2016
	06-03/Apr/2017			
	28/Mar-03/Apr/2017			

(*) On March 3^{rd} and 21^{st} during service mode only one spectrum was obtained each night. (!) HEROS spectra were taken in robotic mode during several months as complementary observations.

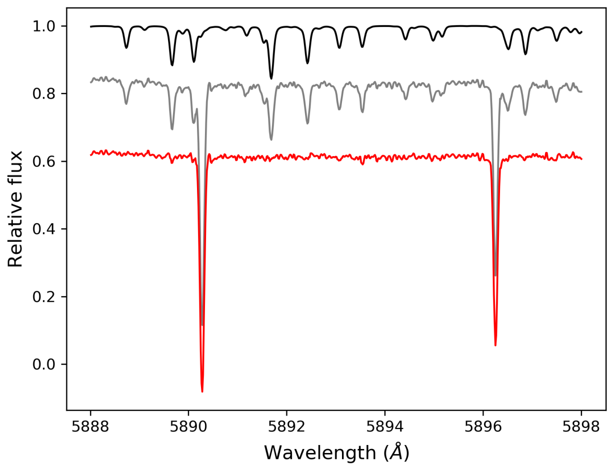

Fig. 2: Example of telluric subtraction in HD 21620 in the Na I D spectral region. Black line shows the MOLECFIT atmospheric model; grey line shows the observed spectrum; and red line shows the final telluric-free HD 21620 spectrum.

initially to iterate the solutions for all objects, the solutions being consistent with that metallicity for most of the stars. For the 15 objects with [M/H]≤ -0.5 according to our estimates, eight of them, namely HD 31295, HD 74873, HD 110411, HD 125162 (λ Boo), HD 183324, HD 198160 (HR 7959), HD 198161 (HR 7960) and HD 221756, were classified as λ Boo stars by Murphy et al. (2015a), consistently with their expected underabundace in heavier elements.

For cooler stars (later than F2), a different approach was used to calculate parameters. In those cases we have followed the procedure described in detail by Maldonado & Villaver (2017) and Maldonado et al. (2018), which is based on the iron ionisation and excitation equilibrium, and match of the curve of growth conditions.

Radial velocities (v_{rad}) were estimated by measuring the shift between the synthetic spectrum, which is computed using a database of rest wavelengths, and the observed spectrum, corrected for barycentric velocity. Individual shifts were measured for the Balmer lines from Hγ to H9. Hϵ, which is blended with Ca II H, was excluded. Lines bluer than H10 were discarded since the lower part of the absorptions were usually noisy. Most of the stars have large values of the projected rotational velocity, $v \sin i$, therefore the cores of the lines, and in particular the Balmer ones, are fairly rounded; thus, a direct evaluation of the wavelength at which the minimum intensity occurs introduces large uncertainties. The procedure we have followed is to slightly smooth the spectra, and then take as the reference wavelength that of the bisector corresponding to 10% of the line intensity measured from the bottom of the absorption. The same was done on the synthetic profile and the difference was converted into v_{rad}; the results do not change significantly if instead of using the synthetic spectrum, the rest laboratory wavelength of the particular Balmer line was taken as reference. The v_{rad} uncertainties come from the standard deviation of the set of displacements. Fig. 3 shows the method explicitly.

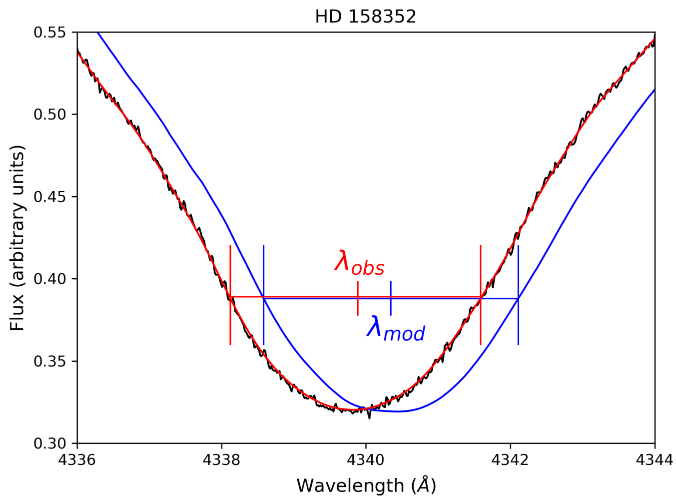

Fig. 3: Radial velocities are measured as the difference between the synthetic model at rest (blue line) and the smoothed spectra at the radial velocity of the star (red line). The method is illustrated in the plot by means of the observed Hγ line in the star HD 158352 (black line). A detailed description is given in the text.

3.3. Non-photospheric absorptions

The Ca II H&K and Na I D lines were visually inspected to search for the presence of non-photospheric, stable or variable, absorption features at the core of the photospheric lines, which would suggest the presence of circumstellar gas. A median spectra (when data from different telescopes were available, all spectra were converted to the FEROS resolution in order to construct the median) was constructed for each star to improve the signal to noise ratio in order to analyse the potential stable absorption, This analysis has been carried out by estimating the photospheric contribution with splines fitted to the bottom of the lines, and then dividing the observed profiles by the estimated photospheric lines, and finally fitting Gaussians to the residuals.

A total of 60 stars show stable, non-photospheric Ca ii and/or Na i absorptions (Table B.3); at the same time, irregular, variable features are seen in individual spectra of 18 stars (Table 2). For these latter stars, when no variations were detected in a range of hours/days, a median was constructed including all the consecutive non-variating spectra. The stable absorptions, when arising in the CS environment (see Sect 4.1.1), appear at the radial velocity (v_{rad}) of the stars or close to it, while the variable ones appear red- and/or blue-shifted.

In the following we present a separate analysis for stars only showing stable non-photospheric absorptions, and stars with variable components regardless of whether they also have stable absorptions.

4. Results

4.1. Narrow, stable absorption features

As mentioned above, a total of 60 out of the 117 stars in the sample show narrow, stable absorption features superimposed on the photosphere, either in the Ca ii and/or the Na i lines. Fig. 1 (Cont.) shows the observed line profiles for both the Ca ii H&K and Na i D lines of the 60 stars, along with their residuals, once the photosphere has been divided. Table B.3 lists radial velocities (RVs), equivalent widths (EWs), column densities (N), and the velocity dispersion (FWHM of the Gaussian fits) of the non-photospheric median stable absorptions, as estimated for the Ca ii H&K and Na i D lines. EWs were calculated with respect to the adjacent continuum, once divided the photospheric contribution. The EW ratio for the Ca ii and Na i doublets expected from the atomic properties of the transition (range 0.5 – 1.0 in both cases encompassing the optically thin and optically thick regimes) is not always maintained, due to the EW uncertainties and the very complex geometry and composition of the CS gas. Column densities were estimated following Somerville (1988) in order to deal with the saturated lines. Uncertainties for the features' radial velocities are estimated as two pixels of the median spectra corresponding to ~2.5 km/s in Ca ii lines and ~1.5 km/s in Na i lines, and being this value consistent with the FWHM of the lines of the calibration lamps. In the case of the EWs, we estimate an uncertainty of 10% in our measurements. Uncertainties for column densities were calculated as propagation of the EW uncertainties according to the formulas for the non-saturation and saturation cases (Eq. 1 and 7 in Somerville 1988, respectively). In some stars, most previously classified as shell stars, the Ca ii K line has a sharp, very pronounced triangular-like profile consisting in a very narrow core and broader wings, which cannot be fitted by either a Gaussian or a Voigt profile; in those cases, we have measured the EWs of the excess absorption with respect to the photospheric line and the velocity dispersion as the FWHM of the mentioned excess absorption, i.e., the velocity dispersion at one half of the absorption depth.

4.1.1. Origin of the non-photospheric stable absorptions

Stable non-photospheric absorption features might originate in the close-in CS environment of the star, or in the warm and cold clouds of the local interstellar medium, ISM (e.g. Redfield & Linsky 2008a). In order to try to decipher the origin, we have compared the radial velocity of those features with the radial velocities (v_{rad}) of the corresponding stars (Table B.2 and Table B.3) and with the velocity vectors of the local ISM (v_{ISM}) towards the line of sight of each star, as given for the ISM clouds in Redfield & Linsky's Colorado model[3]. Velocities and names of the clouds are also given in Table B.3. Nonetheless, a sound ascription to any of both CS or ISM origins is ambiguous in some cases; for instance, when the stellar v_{rad} and the ISM v_{ISM} along its line of sight are very close, or when there is no identified ISM Colorado cloud along the line of sight towards some stars with narrow Ca ii and Na i absorptions. Further, the properties of the non-photospheric absorptions do not clearly discriminate the plausible origin (Redfield et al. 2007) since the observed EWs in the ISM of the Ca ii H&K and of the Na i D lines and their ratios vary by several orders of magnitude (e.g Welty et al. 1996; Redfield & Linsky 2008a; Welsh et al. 2010). We note that Na i is found in cold ISM gas (~ 50 K) typically at distances larger than ~ 80 pc (Welsh et al. 2010), although is also occasionally found at shorter distances (e.g. Bertin et al. 1993; Welty et al. 1994); whereas Ca ii appears in much warmer medium (~ 5000 K) and is usually detected at much shorter distances (e.g. Redfield & Linsky 2008b).

In this context, and taking into account the mentioned caveats, we identify stars with CS gas those that satisfy any of the following criteria: i) stars with variable absorptions (see section 4.2); ii) stars where the non-photospheric absorption shares its velocity with the radial velocity of the star but not with any ISM Colorado cloud; iii) stars with Ti ii absorption lines and shell stars where the Ca ii K line has a sharp, triangular-like profile. We point out that some stars have more than one non-photospheric feature that can be independently identified with the velocity of the star or of the ISM. Also, for some stars the absorptions neither coincides with v_{rad} nor with v_{ISM}. When possible, an inspection for nearby stars was made in a field of 5^{o} in radius and distances ± 20 pc around each star. A column in Table B.3 shows our guess for the origin of the non-photospheric absorptions.

4.1.2. Comments on individual stars

In this section we discuss the plausible origin of the stable non-photospheric absorptions for some individual stars or group of stars. Stars with variable absorption features detected in this work are discussed in section 4.2. HD 9672 (49 Cet), HD 32297, HD 110058, HD 131488, HD 131835, HD 138813, HD 146897, HD 156623, HD 172555 and HD 181296 (η Tel) were analysed in Rebollido et al. (2018); therefore, we do not repeat the discussion here. We note, however, that Na i D features in the stars HD 9672, HD 156623, and HD 172555 were erroneously omitted by Rebollido et al. (2018). A corrigendum can be found in Rebollido et al. (2019). We point out that this mistake does not affect the main conclusions of Rebollido et al. (2018). The Na i D features are nonetheless included in Table B.3 and shown in Fig. 1 (Cont.). In HD 9672 the Na i D absorption appears at the velocity of the Ca ii feature, the radial velocity of the star and the velocity vector of the local interstellar cloud (LIC) cloud. In the case of HD 156623 the Na i D feature appears in emission at the stellar v_{rad}. For HD 172555 two Na i D2 components appear, one close to the G cloud in agreement with Kiefer et al. (2014a), and a second one very broad and variable (see section 4.2).

[3] http://sredfield.web.wesleyan.edu/

- HD 2884, HD 2885, and HD 3003 are members of the Tuc-Hor association. All three stars have similar proper motions, radial velocities and parallaxes. The projected angular separation between HD 2884 and HD 2885 is $\sim 27''$ while the one between HD 2884 and HD 3003 is $\sim 9'$. Thus, they likely form a physical multiple system (see also Eggleton & Tokovinin 2008; Tokovinin 2008; Howe & Clarke 2009). HD 2885 itself is a binary candidate (Lagrange et al. 2009). Our spectra show a weak narrow Ca II K absorption in HD 2884, a weak Na I D absorptions towards HD 2885, and weak Ca II K and Na I D absorptions towards HD 3003 (see also Iglesias et al. 2018). All these absorptions are close to the velocity vector of the Vel cloud and do not coincide with the v_{rad} of the stars (Table B.3 and Fig. 1 (Cont.)). HD 224392 is another Tuc-Hor star located at a similar distance from the Sun as the multiple system and at an angular separation of $\sim$ 4 deg. Its spectrum shows non-photospheric absorptions of both Ca II and Na I. The velocity of the Ca II feature is close to the Vel cloud and to the Ca II absorptions in HD 2884 and HD 3003; the velocity of the Na I is close to the Cet Colorado cloud that passes at $< 20^o$ the line of sight of HD 224392. All these facts suggest an ISM origin for the Ca II and Na I features; however, this ascription is controversial. First, we note that neither Ca II nor Na I non-photospheric features appear simultaneously in HD 2884 and HD 2885. At the same time, Na I is detected towards HD 3003 but not towards HD 2884. Thus, since all three stars are located very close, in particular HD 2884 and HD 2885, a CS origin for the observed features cannot be excluded. Given all these facts, we find ambiguous to ascribe the non-photospheric features in all 4 stars to either a CS or ISM origin and further observations are needed to elucidate their origin.
- HD 5267 has a strong non-photospheric feature at $\sim$ –5.0 km/s in both Ca II and Na I lines. The velocity of this feature does not coincide with v_{rad} (9.5 km/s) or with the v_{ISM} of any Colorado cloud. At the same time, there is a weak Ca II K feature at $\sim$10.0 km/s, also tentatively detected in the Na I D2 line, close to stellar radial velocity and the velocity vector, 11.44 km/s, of the LIC cloud (Table B.3). Unfortunately there are no spectra of field stars in the ESO archive that can be used to discriminate the origin of the component at –5 km/s. We note, however, that this feature is $\sim$15 km/s blue-shifted relative to the radial velocity of the star, and that HD 5267 has a similar effective temperature as HD 181296, T_{eff} $\sim$10500 K. HD 181296 has a stable component $\sim$20 km/s blue-shifted relative to the stellar velocity, most likely of CS origin as suggested in Rebollido et al. (2018) (see Chen & Jura 2003, for other examples). Thus, while the origin of the $\sim$10 km/s component is ambiguous, the origin of the –5 km/s is unknown.
- HD 16978 is another Tuc-Hor star reported by Welsh & Montgomery (2018) as having a variable non-photospheric Ca II K profile within 3 observations. Our spectra show such absorption with a similar EW but does not show the mentioned variability. The radial velocity of the feature coincides with the stellar v_{rad}, and it differs $\sim$4 km/s from the v_{ISM} of the Vel cloud. Given the variability of the feature profile noted by Welsh & Montgomery (2018), which might be indicative of a transient event, the more plausible origin is CS, although we cannot definitively exclude an ISM origin.
- The stars HD 71043, HD 71722, and HD 105850 have Ca II and Na I features close to the velocity vectors of Colorado clouds, and far away form the stellar v_{rad}, supporting an ISM origin, in agreement with Iglesias et al. (2018). This is also the case for the star HD 188228 where only a weak Na I absorption is seen close to the velocity of the G and Vel clouds.
- HD 118232 (24 CVn), HD 125162 (λ Bootis), and HD 221756 have non-photospheric absorption features not coinciding either with the stellar radial velocities or any known ISM Colorado clouds. Due to their high declinations (> +40°) we have not found any spectra of field stars in ESO archive which could help to elucidate the origin of the absorptions. Nonetheless, we find an ISM origin is the most plausible one given the remarkable shift in velocity between the features and the photospheric lines.
- HD 145689 (HIP 79797) is a member of the Argus association and shows a weak Ca II absorption at a velocity of –11.9 km/s, between the radial velocity of the star at –7.1 km/s and the velocity of the G Colorado cloud at –17.21 km/s. The F0 V field star HD 147787, located at a distance of 40 pc and a projected separation of $\sim 4°$ from HD 145689, does not show any non-photospheric feature in its spectrum. Thus, given this fact and since the difference between the Ca II feature and the stellar v_{rad} is $\sim 2\sigma$ we cautiously assign a CS origin to the Ca II absorption.
- HD 158352 (HR 6507) has two Ca II H&K and Na I D absorption components relatively close to the stellar v_{rad}. There are no Colorado clouds along the line of sight of the star, but it passes near (< 20°) several clouds with similar velocity vectors. Our spectra reveal a faint narrow Ca II 8542 Å absorption, and several faint Fe II and Ti II lines characteristics of shell stars. Iglesias et al. (2018) assign the Ca II H&K absorptions an ISM origin based on two field stars, HD 156208 and V 2373 Oph, that have absorptions similar to those of HD 158352. We find, however, that the ISM origin is ambiguous. HD 156208 and V 2373 Oph are at distances $\sim$ 217 pc and $\sim$ 476 pc, respectively, i.e. considerably larger than the distance to HD 158352 of $\sim$ 63 pc. Therefore, while an ISM cloud could be located closer than 63 pc, it cannot be excluded that some ISM clouds responsible for the Ca II H&K and Na I D are located between HD 158352 and the other two stars. On the other hand, Welsh & Montgomery (2015) observed two Ca II K absorption components and attributed one of them a CS origin as it coincides with the stellar v_{rad}. Thus, while CS gas is certainly present around the star, the origin of the Ca II H&K and Na I D absorptions is not completely obvious. We note that Lagrange et al. (2009) identify this star as a binary candidate.
- HD 168646 (HR 6864) has a pronounced triangular profile in the Ca II at the bottom of the stellar lines, as well as many strong shell lines of Ti II, Fe II, and strong cores in the Balmer lines. The Na I D lines present a strong feature close to the Ca II one, and a weaker one at a velocity of $\sim$ –22 km/s, away from the Aql cloud. A very weak third component might appear only in the D2 line at a velocity of $\sim$ 11 km/s. If real, this weak feature seems to have small variations in flux; we cannot make, however, any sound statement as we only have spectra taken in a single epoch. All features have velocities far away from any ISM Colorado cloud. In any case, the strong shell spectrum clearly traces the presence of CS gas.
- HD 177724 (ζ Aql) and HD 210418 have weak Ca II non-photospheric absorptions, each at their respective stellar radial velocities and close to some Colorado clouds. We have not found any useful field star in the ESO archive which could help to elucidate the origin of the features. Thus, the ascription to any of both CS or ISM origins is ambiguous .
- HD 196724 is a candidate shell star (Hauck & Jaschek 2000) with low rotational velocity, which shows a weak Ca II absorption at the stellar v_{rad} and also close to the v_{ISM} of the

Mic and Aql clouds. It might have weak Na I absorption but the spectra are too noisy to make a firm conclusion. The weak Ca II feature does not reveal a sharp, pronounced profile as it is seen in the Ca II K&H lines in other shell stars. Thus, we find ambiguous the origin of the Ca II (and Na I if real) absorptions.

– HD 198160 (HR 7959) is a λ Bootis type star with a very weak Ca II K absorption at the stellar v_{rad} and the Vel cloud v_{ISM}. It forms a binary system with another λ Bootis star, HD 198161 (Holweger & Rentzsch-Holm 1995; Faraggiana & Bonifacio 1999), both components at a projected angular separation of just 2.3″. Weak Ca II K and Na I absorptions are detected towards HD 198161. We also note that a very weak Na I absorption is present towards HD 198160. Thus, while a CS origin cannot be excluded, we find an ISM origin more realistic given the fact that we detect very similar absorptions towards both stars. However, we note that Holweger & Rentzsch-Holm (1995); Holweger et al. (1999) favour a CS origin around the binary.
– Stars belonging to the Upper Scorpius subgroup in the Scorpius-Centaurus association deserve particular attention. There are 13 stars in our sample belonging to this subgroup (Table B.1). All of them are located in a region of 5 sq. deg., and between 110 and 150 pc. The stars show non-photospheric Ca II and Na I absorption components which tend to be grouped around ∼–9 km/s, ∼–15/–23 km/s, and ∼–28 km/s (Table B.3), in agreement with Welty et al. (1994). Most of the stars, with few exceptions, have two features with similar velocities in both Ca II and Na I lines; depending on the star those two features are distributed among the three mentioned velocity ranges. The more blue-shifted components at ∼–28km/s are close to the G cloud velocity vector; the least blue-shifted components at ∼–9 km/s are often close to the radial velocities of the stars. The fact that similar features, including those in the range ∼–15/–23 km/s, are shared in one way or another by all stars strongly suggests their ISM origin, as already noticed by Rebollido et al. (2018) for HD 138813 and HD 146897. In general, the strongest feature is the less blue-shifted one, i.e., the one close to the stars' v_{rad}; this trend holds irrespectively of whether one or two absorption features are detected in any of the Ca II and/or Na I; exceptions to this general trend are HD 146606, and HD 145964 - we refer to this star again in section 4.2 as it has a non-photospheric event identified by Welsh & Montgomery (2013). The above results point evidently out that the ISM towards Upper Scorpius is not homogeneous, but with a notorious complexity likely structured in clumps or relatively small cloudlets, with different properties and located at different distances, discernibles along very nearby lines of sight. Finally, we note that a faint emission feature at ∼–1.2 km/s is detected in both lines of the Na I doublet towards HD 138813. As shown in Fig. 4, the emission is not related to the telluric subtraction. The emission feature is at the radial velocity of the star, and is similar to the emission feature detected towards HD 156623, a star with Ca II variable events (Rebollido et al. 2018, 2019). These emissions are most likely originated in the CS medium, as they are observed in every spectra, regardless of the observing campaign or atmospheric conditions.

4.2. Variable gas detection

Sixteen stars in our sample were selected because of variable, β Pic-like events of their Ca II H&K and/or Na I D lines. The stars

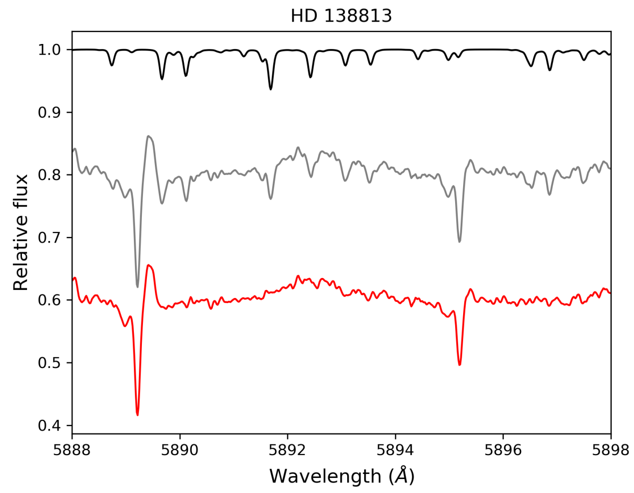

Fig. 4: Na I D lines of HD 138813, where the emission near the radial velocity of the star is easily recognisable and clearly present in the uncorrected spectra (grey line), and not originated as an over subtraction of the atmospheric model (black line). Red line shows the telluric corrected spectrum.

HD 56537 (λ Gem), HD 108767 (δ Crv), HD 109573 (HR 4796), and HD 148283 (HR 6123) also present optical (or UV) events (e.g. Grady et al. 1996b; Welsh & Montgomery 2015; Iglesias et al. 2018) although they were included on the basis of other criteria (Table B.1). These stars are listed in Table 2 together with five new stars showing variability in non-photospheric features found in the frame of this work - HD 36546, HD 37306, HD 39182 (HR 2025), HD 98058 (ϕ Leo), and HD 156623 (HIP 84881). We also include in Table 2 the star HD 132200; although this star was not included in our sample and has not directly been observed by us, a variable Ca II K absorption feature was found by Rebollido et al. (2018). Our results on ϕ Leo, HD 156623 and HR 10 have already been discussed in Eiroa et al. (2016), Rebollido et al. (2018, 2019),and Montesinos et al. (2019), respectively.

Comments on individual stars

– HD 9672 (49 Cet), HD 32297, HD 50241, HD 56537 (λ Gem), HD 64145 (ϕ Gem), HD 108767 (δ Crv), and HD 148283 (HR 6123) do not present any apparent transient event in our time series spectra (Table 2). Also, while we do not see any variability in HD 138629 (HR 5774) our spectra differ from previous ones (see below). Further, we note that the stars HD 56537, HD 64145, HD 110411, and HD 183324 do not present any stable, narrow absorption at the core of the photospheric line, although HD 110411 and HD 183324 seem to present variability at the bottom of the Ca II K line (Fig. 5, (see also Iglesias et al. 2018)).
– HD 21620 presents one stable non-photospheric absorption in both Ca II and Na I at ∼ 4 km/s (Fig. 1 (Cont.) and Table B.3). This feature does not coincide either with the radial velocity of the star or any of the Colorado ISM clouds; it has, however, a plausible ISM origin as several neighbouring stars have similar Na I absorptions (Génova & Beckman 2003; Welsh & Montgomery 2013). A weak absorption detected in Ca II K at ∼ 16 km/s is close to the ISM velocity of the LIC cloud. Nonetheless the variability of this feature,

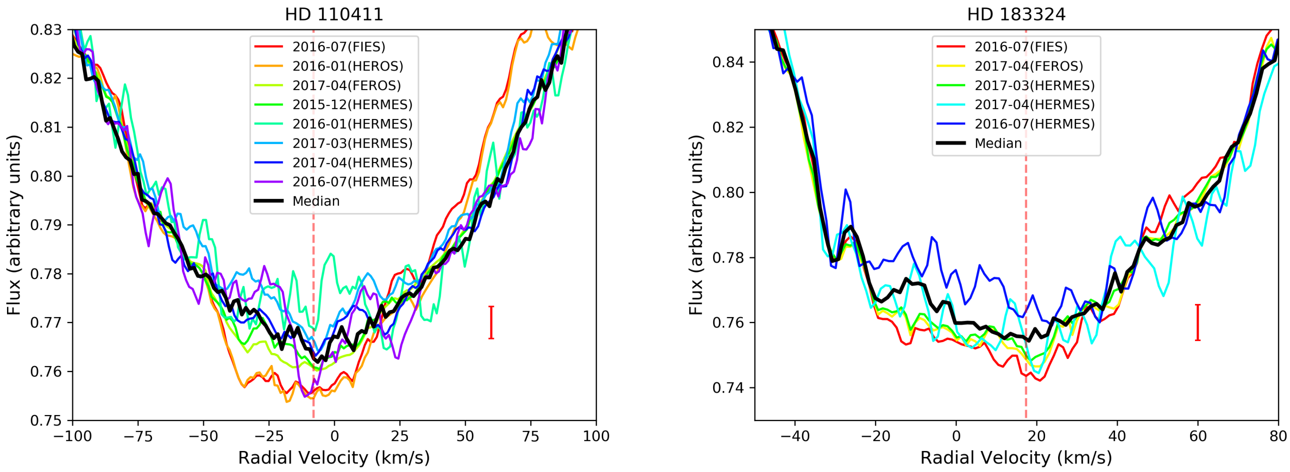

Fig. 5: Photospheric profile of Ca ii K spectra of HD 110411 and HD 183324. Dates and instruments are colour-coded as indicated in the legend. The core of the line varies although neither a narrow feature nor transient events are clearly distinguished. The red dashed vertical line marks the radial velocity of the star. The red error bar shows the 3-σ standard deviation in the region close to the bottom of the line. This applies to all upcoming figures.

also noted by Welsh & Montgomery (2013) (see their Fig. 1 and 2), is remarkable and we attribute it a CS origin. Fig. 6 shows the Ca ii K line of HD 21620 during the campaigns of 2015 and 2016. We detect mostly red-shifted variations in the range of ~ 10-30 km/s, with a tentative, weak blue-shifted event on 04-05/09/2015 at ~ 0 km/s (top left panel of Fig. 6), and a potential red-shifted event at ~ 50 km/s in the NOT median spectra of 07/2016 (bottom left panel of Fig. 6). We note that Welsh & Montgomery (2013) also detected a feature at a velocity close to this last event together with several blue-shifted ones. Some dynamical evolution might be traced by the ~ 16 km/s events observed in January 2016 as suggested by their changes in velocity and depth along three consecutive nights. All Ca ii K events we detect are very weak with no detectable counterpart in the Ca ii H line, which suggests that the gas is optically thin. As an example, Fig. 7 shows both Ca ii lines as observed on Dec 23rd, 2015. The K line can be fitted with two Gaussians at velocities 4.3 and and 16.8 km/s, and equivalent widths of 14.2 and 3.3 mÅ, respectively; at the same time, the 4.3 km/s H absorption, which is the stable one, has an EW = 7.2 mÅ, i.e., this feature is optically thin, while the 16.8 km/s variable one is embedded in the noise, also suggesting optically thin gas.

– HD 36546 presents a narrow feature at a velocity of ~ 15 km/s visible in both Ca ii and Na i lines (Fig. 1 (Cont.)). The origin of the feature is most likely CS as it coincides with the radial velocity of the star and is far from the ISM cloud along the line of sight (Table B.3 and Fig. 1 (Cont.)). A red-shifted event at a velocity of ~ 20 km/s is detected in the Ca ii K spectrum of 6/3/2017, apparently evolving in the following dates and practically disappearing in the spectrum of 8/3/2017 (Fig. 8, left panel). A Gaussian deconvolution of the 6/3/2017 Ca ii K absorption (Fig.9) gives an EW of 8.4±0.9 mÅ for the 20 km/s event, and 24.8±2.5 mÅ for the narrow stronger feature centered at 15 km/s, which is similar to the EW of 27.1±2.7 mÅ of this narrow feature in the spectrum of 8/3/2017. We note that the weak feature at 20 km/s is not discernible from the noise in the Ca ii H line (not shown) suggesting that the gas is optically thin, somehow similar to the case of HD 21620. We also point out that the Na i D2 line

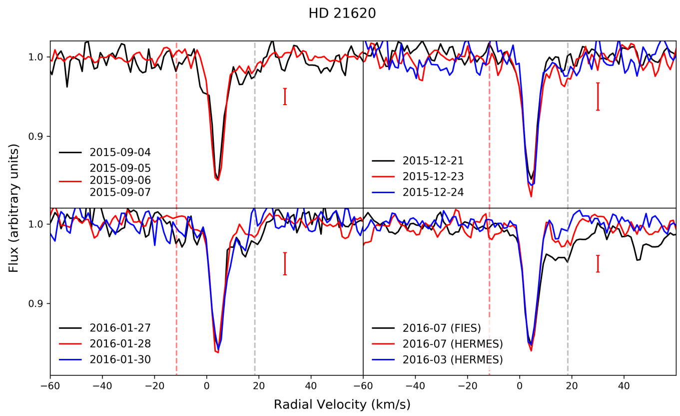

Fig. 6: Ca ii K line of different epochs of HD 21620. Spectra plotted in the panels at the top and lower left were obtained with HERMES. Lower right panel shows median spectra of indicated period and telescope. FEB-like events appear at ~ 16 km/s and tentatively at 0 (blue-shifted, top left panel), and 50 km/s (red-shifted, bottom right). The events of January 2016 appears to present some dynamical evolution. Vertical red and grey dashed lines show the stellar and ISM radial velocities respectively.

presents as well an asymmetry in the red wing, with a small change of slope when comparing the different dates (Fig. 8, right panel).

HD 36546 hosts a bright debris disc (Table B.1) seen near edge-on with an inclination angle $i \sim 70-75°$ (Currie et al. 2017), following the trend suggested by Rebollido et al. (2018) between the disc inclination and the presence of narrow non-photospheric absorptions at the radial velocity of the star. Lisse et al. (2017) found evidence of a C-rich CS environment which makes HD 36546 similar to β Pic and 49 Cet (Roberge et al. 2006, 2014). Thus, it can be another example of an enhanced carbon abundance acting as a braking mechanism of the hot inner (<1 AU) CS gas released by evaporation of exocomets, dust grains or grain-grain collisions (Fernández et al. 2006; Brandeker 2011).

Table 2: Stars with variable non-photospheric absorption features. References are within brackets.

Name	Prev. Detected	Det. in this work
HD 256 (HR 10)*	Yes (1,12,15)	**Yes**
HD 9672 (49 Cet)	Yes (2)	No
HD 21620	Yes (3)	**Yes**
HD 32297	Yes (4)	No
HD 36546	No	**Yes**
HD 37306	No	**Yes**
HD 39182 (HR 2025)	No	**Yes**
HD 42111	Yes (5,12)	**Yes**
HD 50241	Yes (5,11)	No
HD 56537 (λ Gem)	Yes (6)	No
HD 64145 (ϕ Gem)	Yes (6)	No
HD 80007 (HR 3685)	Yes (11,15)	**Yes**
HD 85905	Yes (7,15)	**Yes**
HD 98058 (ϕ Leo)*	No	**Yes**
HD 108767 (δ Crv)	Yes (6)	No
HD 109573 (HR 4796)	Yes (6,16)	**Yes**
HD 110411	Yes (3)	**Yes**
HD 138629 (HR 5774)	Yes (8)	No
HD 132200*	No	**Yes**
HD 145964	Yes (3)	**Yes**
HD 148283 (HR 6123)	Yes (5,13)	No
HD 156623 (HIP 84881)*	No	**Yes**
HD 172555	Yes (9)	**Yes**
HD 182919 (5 Vul)	Yes (2)	**Yes**
HD 183324	Yes (10,16)	**Yes**
HD 217782	Yes (2,5,14)	**Yes**

(*) Results have been presented by Eiroa et al. (2016), Rebollido et al. (2018), and Montesinos et al. (2019, A&A in press).
References: (1) Lagrange-Henri et al. (1990a); (2) Montgomery & Welsh (2012); (3) Welsh & Montgomery (2013); (4) Redfield (2007); (5) Roberge & Weinberger (2008); (6) Welsh & Montgomery (2015); (7) Welsh et al. (1998); (8) Lagrange-Henri et al. (1990b); (9) Kiefer et al. (2014a); (10) Montgomery & Welsh (2017); (11) Hempel & Schmitt (2003); (12) Lecavelier Des Etangs et al. (1997); (13) Grady et al. (1996b); (14) Cheng & Neff (2003); (15) Redfield et al. (2007); (16) Iglesias et al. (2018)

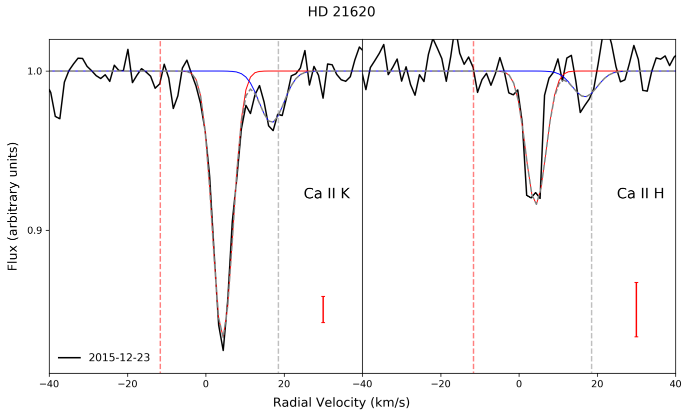

Fig. 7: The Ca ii K and H lines as observed on 23/12/2015 using HERMES. Two Gaussians are fitted to the K non-photospheric feature with velocities 4.3 km/s(red continuous line) and 16.8 km/s (blue continuous line). The strongest, stable 4.3 km/s absorption is clearly detected in the H line, but the weakest, variable absorption at 16.8 km/s is embedded in the noise of the H spectrum. Vertical red and grey dashed lines show the stellar and ISM radial velocities respectively.

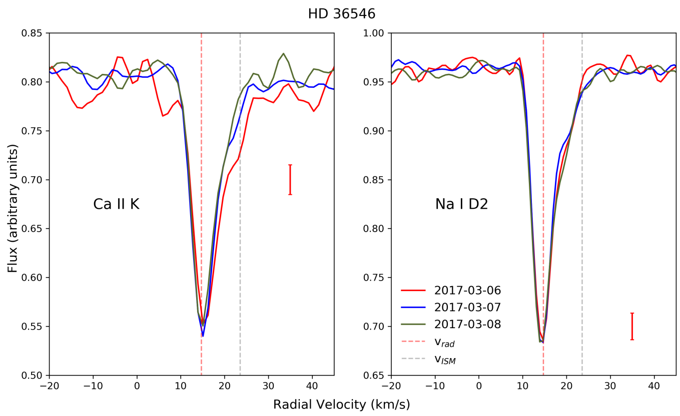

Fig. 8: Left panel: Ca ii K line. A transient event is seen at ∼ 20 km/s superimposed on the red wing of the narrow non-photospheric absorption at ∼ 15km/s. No obvious event is seen in 08/03/2017. Right panel: Na i D2 line. Dates are as indicated, and all spectra were obtained using HERMES. Red and grey vertical lines mark the radial velocity of the star and of the ISM respectively.

– HD 37306 presents two stable narrow Ca ii and Na i absorptions (Fig. 1 (Cont.)) at velocities ∼11 km/s and ∼32 km/s, while the stellar v_{rad} is 25.1 km/s. Nonetheless, the most remarkable and striking behaviour is the strong shell-like spectrum that appeared on the spectra of September 2017. The Ca ii H&K lines developed a strong, symmetric, triangular profile superimposed on the photospheric lines and the two narrow interstellar features, together with narrow shell-like absorptions in the Ca ii triplet or in several Fe ii and Ti ii lines (see Fig. 10). At the same time, photospheric lines as e.g. the Mg ii 4481 Å or the O i triplet at 7750 Å remained constant, as well as the Na i D lines. Further, the strong shell spectrum fully vanished in additional spectra taken in November 28, 2018 with the CARMENES spectrograph in Calar Alto Observatory (Quirrenbach et al. 2016), and from December 14 to 18, 2018 with HERMES. This behaviour has also been observed by Iglesias et al. (2019) partly using the same spectra. Due to the in principle unusual nature of this phenomenon, we have checked possible sources of contamination, such as instrumentation issues or additional sources in the fiber, but we have discarded these scenarios.
Thus, the appearance/disappearance of the shell-like profiles does point out to the presence of CS gas, but no blue-/red-shifted FEB-like events are detected in any of our spectra. We note that variability of shell spectra and even its appearance/disappearance in some stars is well known (e.g. Jaschek et al. 1988). At the same time, and despite the lack of any identified ISM clouds in the line of sight, the fact that no remarkable changes are seen in the mentioned ∼11 km/s and ∼32 km/s narrow features during the 8 days of observations in September 2017, while drastic changes are seen in the CS (shell-type) environment, suggests an ISM origin as the more plausible alternative for those two absorptions, in agreement with Iglesias et al. (2018).
– HD 39182 (HR 2025), one of the selected Ti ii stars, has a sharp triangular-like absorption (Fig. 1 (Cont.)) with two narrow Ca ii components; one is found at ∼ –22 km/s, centred

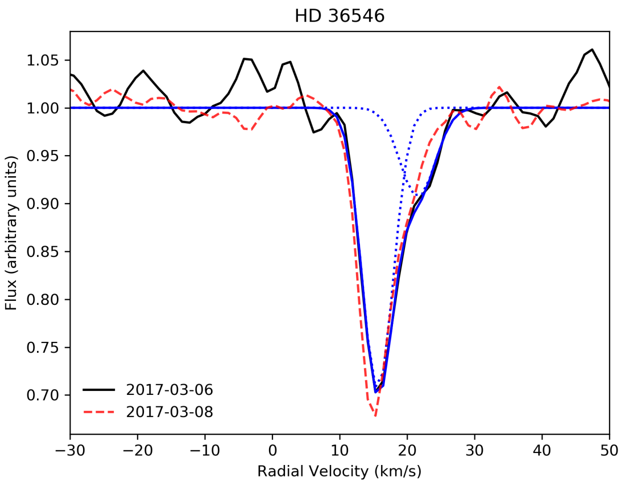

Fig. 9: The Ca ɪɪ K spectra of the HD 36546 non-photospheric absorption for the day where the event in the red wing is most conspicuous (06/03/2016, black line) and when it is practically undetectable (08/03/2016, red dashed line). As in the previous figure, both spectra were obtained with HERMES. Blue solid line shows a fit of the 06/03/2016 spectrum with two Gaussians, each one plotted as dotted blue lines.

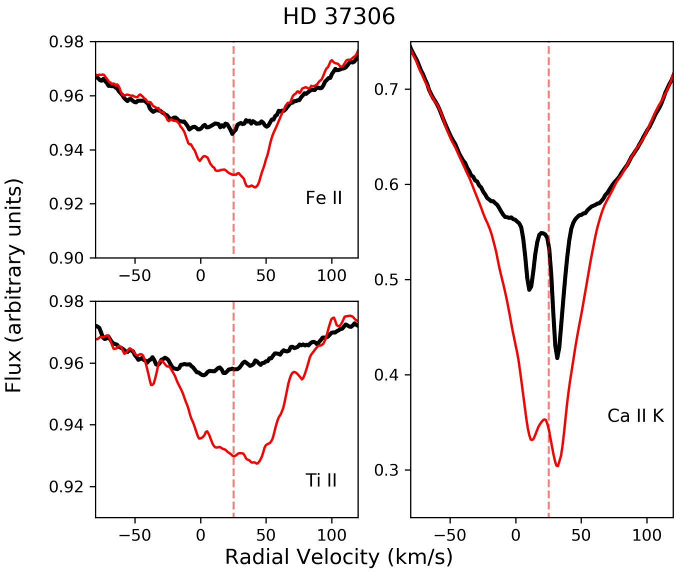

Fig. 10: Fe ɪɪ (4583.83 Å), Ti ɪɪ (4443.80 Å) and Ca ɪɪ K lines of HD 37306. While most of the spectra, represented by the median spectrum in the plot (black line), do no vary and show two Ca ɪɪ non-photospheric absorptions, a strong shell-like profile appeared in September 2017 (red line, FEROS). It was not observed again in later spectra of November and December 2018, not shown in the figure. Red vertical line marks the radial velocity of the star.

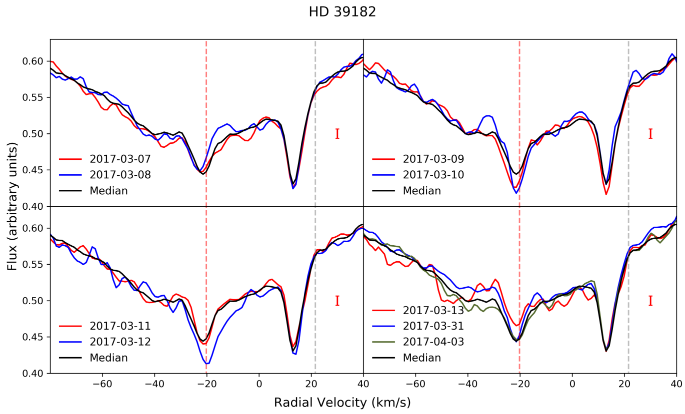

Fig. 11: Ca ɪɪ K spectra of HD 39182 grouped by observing dates obtained with HERMES. In all panels, the median spectra is also plotted. The red and grey vertical lines correspond to the radial velocity of the star and the velocity vector of the LIC Colorado cloud, respectively.

in the photospheric line coinciding with the stellar v_{rad}, and varies significantly; the second, strongest one at ∼ 13 km/s is clearly displaced from the line center (Fig. 11). A weak extra absorption at ∼ –41 km/s is present in some spectra, i.e., in the blue wing of the –22 km/s component (Figs. 1 (Cont.) and 11). The Na ɪ D lines only show a strong narrow absorption at ∼ 14 km/s, coinciding with the strongest Ca ɪɪ component. None of the velocity components coincides with the velocity vector (v_{ISM} = 21.62 km/s) of the LIC cloud, which is seen along the line of sight to the star. As an example of the observed Ca ɪɪ variability Fig. 12 shows both H and K lines taken in two consecutive nights, where remarkable variations of the depth and profile of both non-photospheric features are observed. We also note that our spectra differ from the one reported by Lagrange-Henri et al. (1990c). Their spectrum shows a strong Ca ɪɪ feature at the bottom of the stellar line, i.e., like our –22 km/s feature, but the strong 13 km/s absorption in our spectra, if present, is much weaker. Further, Lagrange-Henri et al. (1990c) do not report any Na ɪ component. Thus, all these results suggest that the origin of all absorptions are CS.

– HD 42111 (HR 2174) is a shell star with strong Ca ɪɪ and Na ɪ absorptions in the median spectrum close to the radial velocity of the star and of the Aur cloud velocity (Fig. 1 (Cont.) and Table B.3), which have previously been reported by Lagrange-Henri et al. (1990c). Those authors attributed a CS origin (at least partially) to the Ca ɪɪ absorption based on a comparison of the dispersion velocities (FWHMs) of Ca ɪɪ K and Na ɪ lines; this result was later confirmed by Lagrange-Henri et al. (1991) by comparing the non-photospheric features of HD 42111 and of the nearby star HD 42092. Further, the (at least partly) Ca ɪɪ CS origin is corroborated by the fact that the EW and FWHM of the Ca ɪɪ K absorption, as estimated with our spectra, are much larger that the ones reported in those works, while at the same time the EWs and FWHM of the strong Na I absorptions are similar - a small change of the Ca ɪɪ K absorption was also pointed out by Welsh & Montgomery (2013). Individual spectra of HD 42111 show that the Ca ɪɪ K feature is formed by two components at velocities ∼25 km/s and 27.5 km/s, supporting the suggestion made by Lagrange-Henri et al. (1990c) concerning the plausible blend of two distinct features. Both Ca ɪɪ K components have very similar strength (Fig. 13), although the feature at ∼25 km/s varies in depth while the one at ∼27.5 km/s appears distinctly only in some selected dates as a kind of β Pic-like events, e.g. 03/03/2016 or 08/03/2017 (Fig. 13), likely with a small dynamical evolution, at least in the March 2016 spectra, (see top-right panel of Fig. 13). In this respect,

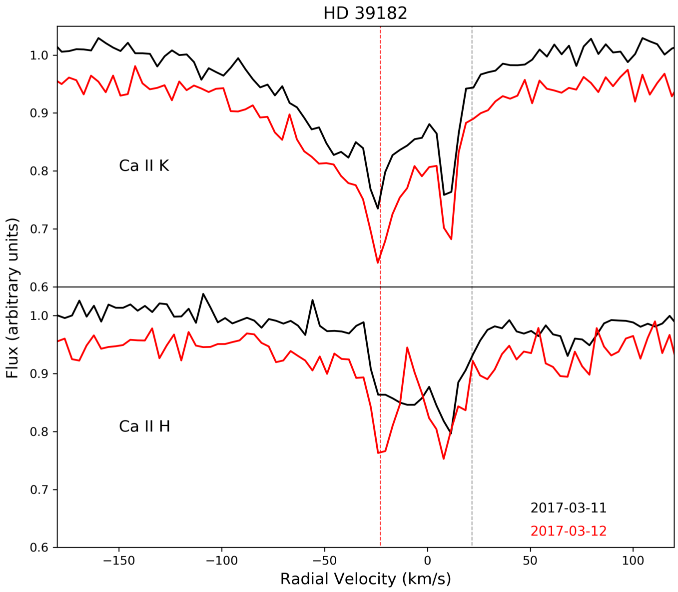

Fig. 12: Ca ɪɪ K and H lines of HD 39182 colour-coded for two different observing dates obtained with HERMES. Spectra have been shifted 0.05 units in the Y-axis aiming to facilitate the visualisation of the variability. The red and grey vertical lines correspond to the radial velocity of the star and the velocity vector of the LIC Colorado cloud, respectively.

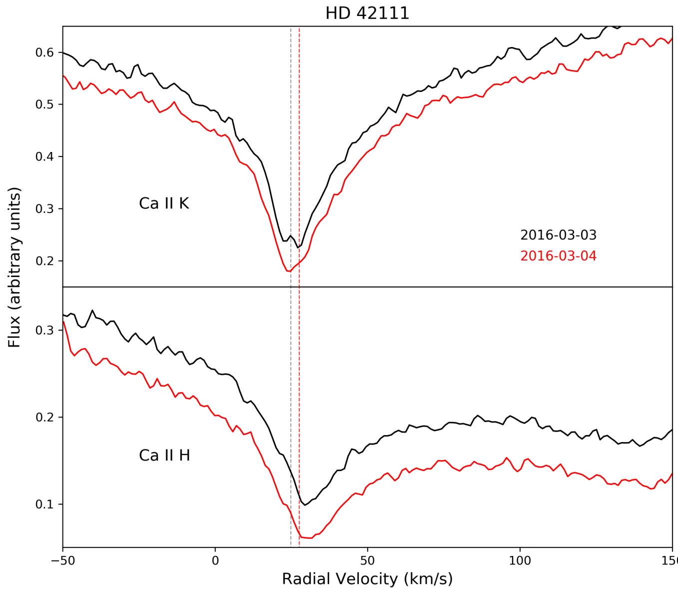

Fig. 14: Ca ɪɪ H&K spectra of HD 42111 obtained with HERMES and grouped as observed in the indicated consecutive dates. The photospheric contribution has not been removed in this plot.The vertical lines correspond to the radial velocity of the star and the velocity vector of the ISM in the line of sight.

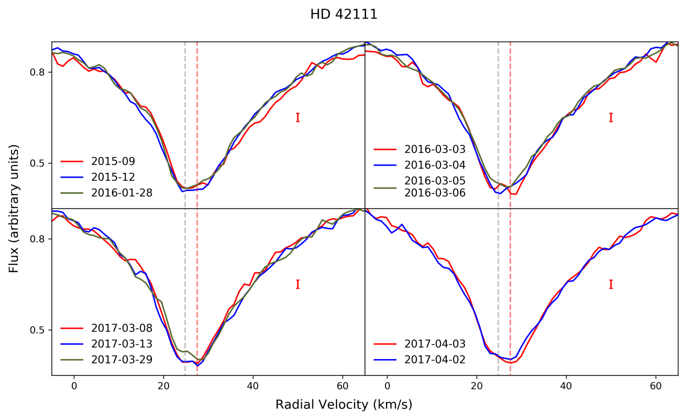

Fig. 13: Ca ɪɪ K spectra of HD 42111 obtained with HERMES and grouped by observing dates. Spectra have been shifted 0.05 units in the Y-axis. The red and grey vertical lines correspond to the radial velocity of the star and the velocity vector of the ISM in the line of sight.

we note that Welsh & Montgomery (2013) reported a FEB-like Ca ɪɪ K event at 75 km/s, and that Grady et al. (1996b) and Lecavelier Des Etangs et al. (1997) detected gas in UV lines of Fe ɪɪ, Mn ɪɪ, and Mg ɪɪ, interpreted as CS clumps falling onto the star. With respect to the Ca ɪɪ H feature, our individual spectra do not resolve both K components, and are all well represented by their median profile; also, the peak of the H line feature is slightly red-shifted with respect to the K absorption. As an example, Fig. 14 plots the Ca ɪɪ H and K lines of the two consecutive nights where that behaviour can be seen. This could be due to the fact that the broad Ca ɪɪ H feature is severely blended with the strong triangular-like profile at the core of the Balmer Hϵ line - such strong triangular-like profiles are clearly present in all Balmer lines. Obviously, additional higher resolution spectra are needed in order to attempt to resolve the Ca ɪɪ H absorption without the interference of the Hϵ line, and to study its plausible variability. We further note that a weak, but very broad, absorption is observed in both Na ɪ D lines producing the observed secondary peak (Fig. 1 (Cont.). That absorption, present in all individual and the median spectrum of HD 42111, is not evident in the spectra by Lagrange-Henri et al. (1990c), Lagrange-Henri et al. (1991), or the high-resolution, unpublished spectrum obtained by EXPORT (Mora et al. 2001).

– HD 80007 has very weak Ca ɪɪ K and Na ɪ D2 absorptions at the stellar v_{rad} (Table B.3 and Fig. 1 (Cont.)). The corresponding Ca ɪɪ H and Na ɪ D1 might be present in our median spectrum but at the noise level (Fig. 1 (Cont.)); and new spectra are required before a sound confirmation can be made. Hempel & Schmitt (2003) noticed a change in the equivalent width, shape, and velocity of the Ca ɪɪ absorption. Redfield et al. (2007) also found variability in the velocity while the column density of the Ca ɪɪ absorption remains relatively constant; in contrast, those authors found more remarkable variability in the velocity (two absorptions at ∼ –7 km/s and ∼ 7 km/s) and column densities of the Na ɪ feature. Further, Welsh & Montgomery (2015) found a quasi two-component Ca ɪɪ K feature in two consecutive nights and one single-component absorption in two other nights, with changes in the equivalent width. In addition, Wood & Hollis (1971) found a quasi-periodic oscillation in the strength of the Hβ Balmer line, and suggested it could be due to flares generated by acoustic oscillations of the stellar atmosphere.
Our spectra show new aspects of both Ca ɪɪ and Na ɪ absorptions as well as in the stellar radial velocity. Firstly, the radial velocity of the star shows a regular variation of the order of ∼ 1.5 km/s per day in both 2016 and 2017 observing periods, Fig. 15. A possibility is that HD 80007 is a binary system and that the radial velocity variability is induced by an un-

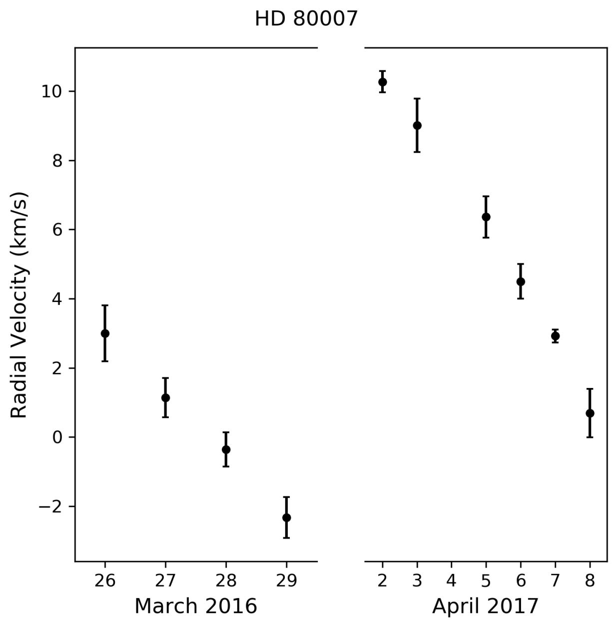

Fig. 15: Radial velocity variation of HD 80007 in both observing periods. The observations suggest the presence of an unseen companion.

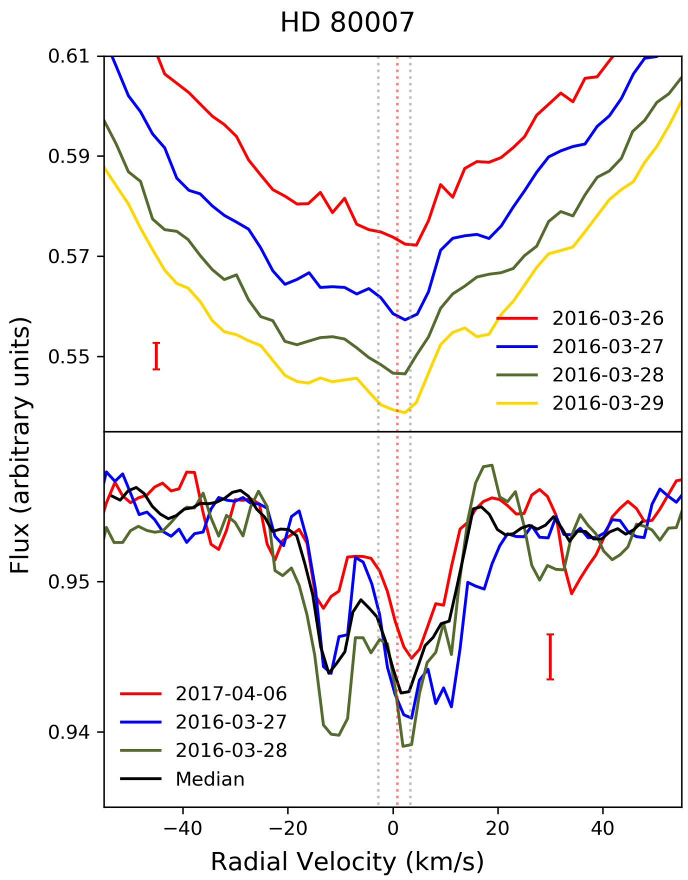

Fig. 16: Top panel: Ca ii K line of HD 80007 for the selected days, observed with FEROS. Spectra have been shifted 0.01 units in the Y-axis aiming to facilitate the visualisation of the variability. The central absorption is seen at ∼ 2 km/s, as well as blue- and red-shifted variable absorptions. Bottom panel: Na i D2 line of HD 80007 for the selected days. Variability is seen at ∼ -10 and ∼ 2 km/s. In both panels it is noticeable the slight shift at the bottom of the narrow absorptions presumably produced by a companion.

seen companion. Secondly, the Ca ii K absorption shows a "central" feature with small changes in its strength accompanied in some spectra with blue- and red-shifted components (Fig. 16, top panel). At the same time the Na i D2 feature presents two components. One is a broad, variable feature centred at ∼ 2 km/s, i.e., the velocity of the star and the Ca ii feature, with a red-shifted wing up to ∼ 18.5 km/s even discernible in the median spectrum (Fig. 16, bottom panel). Further, one red-shifted event at ∼10 km/s and extending up to ∼22 km/s might tentatively be present in the spectrum of 2016 March 27. The second Na i D2 component at a velocity ∼ –11.5 km/s appears in all spectra but it varies its depth. We note that the velocity difference between both features is approximately the same as the ones sporadically observed by Redfield et al. (2007).

- HD 85905 is a shell star whose median spectrum shows a sharp triangular-like Ca ii absorption with two components at velocities at ∼8.4 km/s and ∼25.0 km/s, and one Na i feature at ∼8.1 km/s. The feature at ∼8 km/s coincides with the radial velocity of the star and is also close to the velocity vector of the G cloud (Fig. 1 (Cont.) and Table B.3). Nonetheless, individual spectra from the different epochs show remarkable variability; Fig. 17 shows some examples. During December 2015 both Ca ii K components experienced noticeable variations, while the corresponding Na i 8.0 km/s feature remained constant. However, there is a relatively strong feature at a velocity of ∼23.7 km/s in both Na i D lines, (i.e. close to the Ca ii 25.0 km/s component) visible in all dates of that period (December 2015) but not in any other of our observing epochs. The lower panel of Fig. 17 shows the median of December 2015 spectra of both Na i D lines where this result can be appreciated. Further, while during the periods of December 2015, January and March 2016 both Ca ii components were present, only the component at ∼8 km/s was visible during the two different campaigns of 2017 (March 8 to 11, and March 29 to April 8). During these campaigns, a strong absorption appeared as well in the blue wing of the Ca ii K, while the red-shifted 25.0 km/s feature practically disappears. Fig. 18 shows the profiles of both the Ca ii H and K lines of the median spectra of the three previously mentioned periods where changes of the H line profile can also be appreciated. The above results clearly suggest a CS origin of the non-photospheric absorptions observed in HD 85905, maybe related to a variability of the CS shell as suggested by the variations observed in other shell lines of e.g. Fe ii, but not in photospheric lines as Mg ii 4481 Å or the O i triplet at 7775 Å (not shown). A detailed analysis will be published elsewhere. Welsh et al. (1998) and Redfield et al. (2007) also attributed a CS origin to the Ca ii and Na i absorptions they detected.
- HD 109573 (HR 4796) has two very weak Ca ii K absorptions at ∼ –14.2 and –4.7 km/s in the median spectrum (Fig. 1 (Cont.)). The one at –14.2 km/s is not detected in the Ca ii H line, suggesting the gas is optically thin, as it is the –4.7 km/s feature. This latter absorption is also present in the Na i D lines. None of these features coincides with the radial velocity of the star. Fig. 19 shows details of the Ca ii K line on different dates (the Ca ii H line is only revealed with the me-

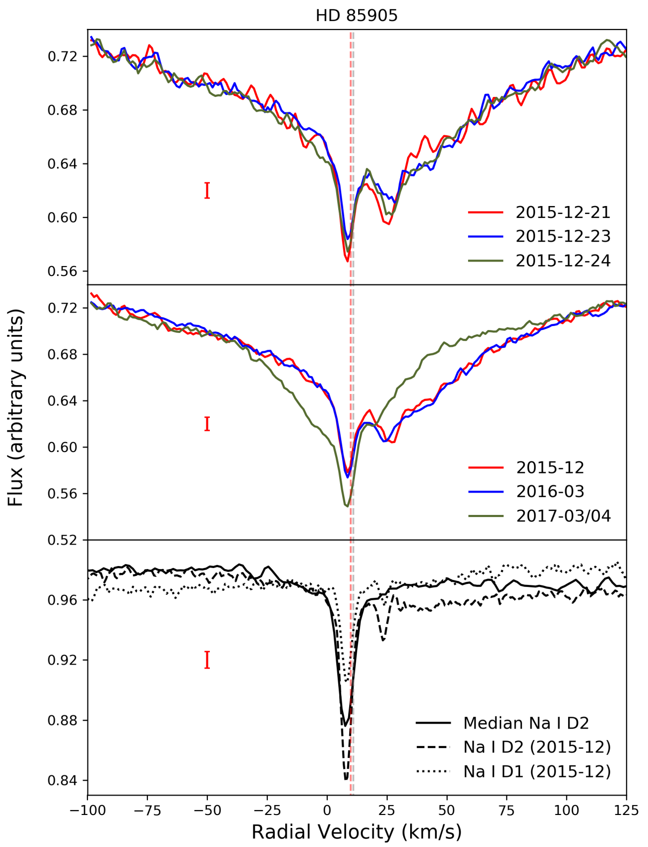

Fig. 17: Top panel: Days 21, 23 and 24 of December 2015 where variability of the ∼ 25 km/s Ca ii K feature can be seen. Middle panel: Ca ii K median spectra of three different campaigns using HERMES where the variability in the triangular profile is seen. The absorption at ∼ 25 km/s disappears in March 2017. Lower panel: Na i D lines of December 2015 where the absorption at ∼ 23 km/s is visible. The median of all spectra in the Na i D2 line where the absorption is no longer present is also shown. The vertical lines correspond to the radial velocities of the star and of the ISM.

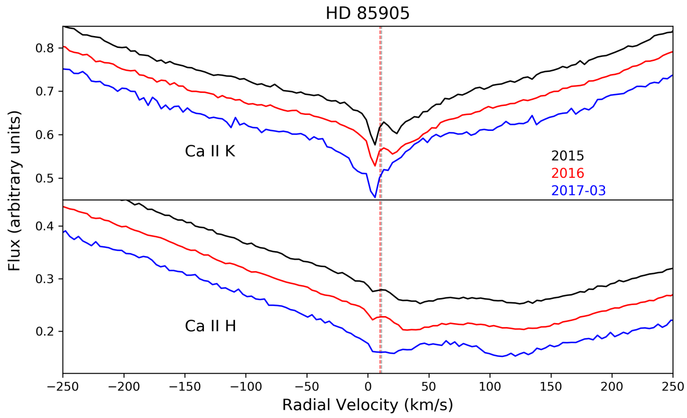

Fig. 18: Ca ii H and K median spectra of the campaigns indicated in the labels obtained using HERMES, where the variability of both lines can be appreciated. Spectra have been shifted 0.05 units in the Y-axis The photospheric contribution has not been removed in this plot. The vertical lines correspond to the radial velocities of the star and of the ISM.

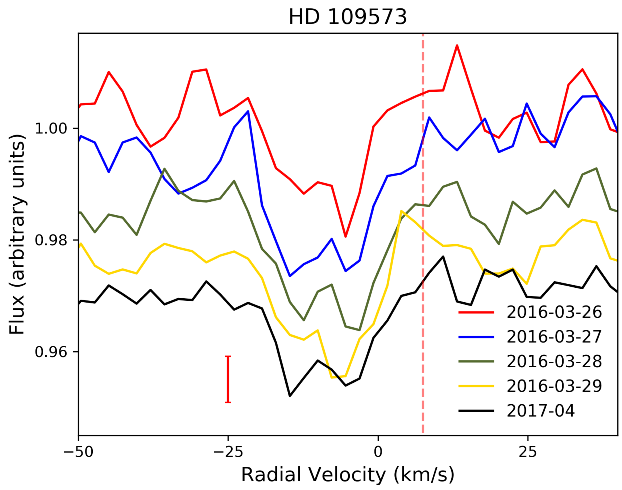

Fig. 19: Ca ii K line of HD 109573. A shift of 0.005 has been added to the Y-axis in order to help differentiate the variations. All spectra were obtained using FEROS. The red vertical line corresponds to the radial velocity of the star. Ca ii K line shows two absorptions not coincident with the radial velocity of the star but with variations in their strength.

dian spectra of all 23 individual spectra of HR 4796). Both Ca ii K components vary in depth and shape, in some cases close to the noise level. Nonetheless, a discernible variability is seen, e.g. the -14.2 km/s component of March 2016 26th and 29th is distinctively weaker than of March 2016 27th, 28th. or the median of April 2017. Our spectra and the variability of the Ca ii K features are quite similar to those in Welsh & Montgomery (2015), strongly suggesting a CS origin. Nonetheless, Iglesias et al. (2018) attribute the –5 km/s feature an ISM origin, as the field star 1 Cen (HD 110073; 30 pc behind HR 4796) also has a similar absorption feature. Welsh & Montgomery (2015) detected a faint FEB-like event at ∼ 60 km/s in two spectra of a single night; and Iglesias et al. (2018) report a faint variable feature at the velocity of the star. None of these are apparent in our spectra.

– HD 138629 (HR 5774) has three non stellar Ca ii features at velocities –31.8, –22.9, and –13.8 km/s with no sign of variability, none of them clearly coincident with v_{rad} or with v_{ISM}. The Na i D lines also present three absorptions, two of them coinciding with two Ca ii ones (Fig. 20). Our spectra differ from the two and four Ca ii components, and from one Na i feature, reported by Lagrange-Henri et al. (1990b). We attribute at least partially a CS origin due to the apparent changes with previous works, but an ISM origin can not be excluded at least for the features at ∼ –22 km/s and ∼ –12 km/s.
– HD 145964 is one of the Upper Scorpius stars. Two absorption components at velocities ∼ –9.5 km/s and ∼–25 km/s are detected in Ca ii and Na i lines (Fig. 1 (Cont.) and Table B.3). Those components can in principle be attributed to the ISM medium as they are also detected in many other UpSco stars (see Sect. 4.1.2). However, while the profile of Ca ii

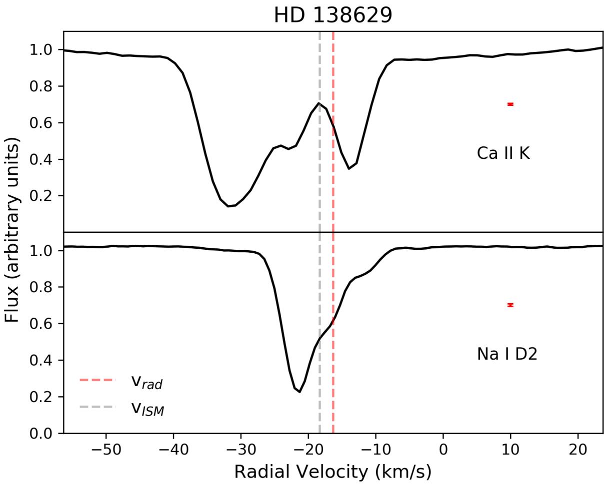

Fig. 20: Median HERMES spectra of Ca ii K and Na i D2 non-photospheric absorption features observed towards HR 5774. Dashed lines correspond to the radial velocity of the star (red) and the velocity vector of the interstellar NGP cloud (blue).

K feature at –9.0 km/s, which is the velocity of the star, remains practically constant, the asymmetric blue wing of the –25 km/s absorption shows a weak ∼ –30 km/s component in most spectra of all observing runs, but not e.g. in both the Hermes and FEROS spectra taken during the same dates in April 2017 (Fig. 21). We also note that a marginal variation in the relative depth of the –9.0 km/s and –25 km/s features might be present. The same behaviour is observed in the Ca ii H line (Fig. 22).
Thus, a CS contribution is suggested, in particular for the –25 km/s and –30 km/s absorptions. Similar Ca ii K absorptions were detected by Welsh & Montgomery (2013), who also reported a weak FEB-like event at a velocity of ∼ 50 km/s that is not detectable in our data.

– HD 172555 was already discussed by Rebollido et al. (2018) as one of the debris disc stars with both cold and hot gas in its circumstellar environment (see also the first paragraph of Sect. 4.1.2). Here we want to stress that a weak ISM feature is detected in both Ca ii lines at a velocity of ∼–20 km/s, in good agreement with Kiefer et al. (2014a). In addition, our spectra reveal a weak, broad Na i D2 feature centred at ∼15.3km/s and extending from ∼–5 km/s up to ∼35 km/s. Although the individual spectra are relatively noisy we are confident on this detection as it appears in all spectra. The top panel of Fig. 23 shows the Na i D2 median spectrum, and spectra of 08/03/2016, 08/04/2017. The broad Na i D2 feature presents a clear variability, denoting its CS nature. The bottom panel of Fig. 23 shows the telluric subtraction for the indicated dates, where it is clear the variability is not related to telluric lines. Fig. 23 (top panel) also shows the median of all Na i D1 line spectra, where the ISM feature is clearly visible but not the broad CS one. We note that Grady et al. (2018) detected some UV broad, variable absorptions of ions like e.g. Cii.
– HD 182919 (5 Vul) has a weak, narrow absorption feature at ∼–18.5 km/s, close the velocity of the star and to the G, Mic, and Aql clouds (Table B.3 and Fig. 1 (Cont.)). The feature varies its depth (∼ 6.0σ) when analysing the median spectra of different epochs (Fig. 24); thus, it most likely has a CS origin, at least partly. During the 2016 July observing run at Mercator a very weak Ca ii K blue-shifted absorption with an EW of 1.3 mÅ is apparent at a velocity of ∼ -35 km/s; in addition, the spectrum of 2016-07-14 shows a Ca ii K red-shifted event at ∼ 25 km/s and EW 1.6 mÅ. This absorption is not detected in the Ca ii H line. Since its value is consistent with a 3.1 σ detection, we consider the detection *tentative*. We note that Montgomery & Welsh (2012) also noticed the variability of the narrow absorption as well as the presence of a FEB-like event with a velocity range 15–60 km/s in one of their spectra.
– HD 217782 (2 And) has three Ca ii absorptions at velocities ∼ –17.1 km/s, –9.2 km/s, and 5.2 km/s (see Fig. 1 (Cont.)).

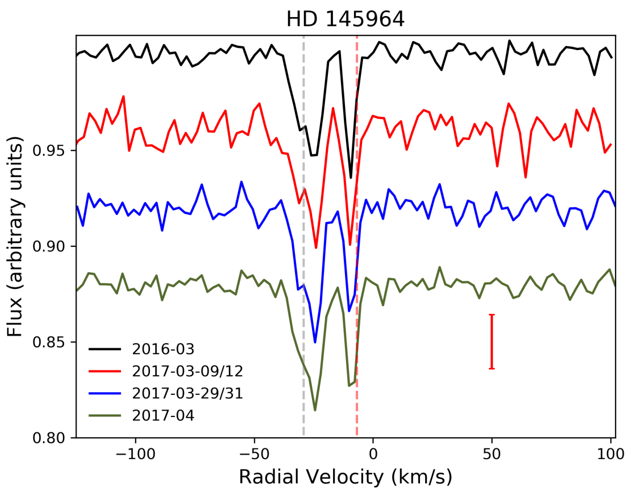

Fig. 21: Ca ii K spectra of HD 145964 as indicated in the labels, obtained using HERMES. An offset of 0.04 was introduced in the Y-axis to better perceive the variations. The red and grey vertical lines correspond to the radial velocity of the star and the velocity vector of the G Colorado cloud, respectively

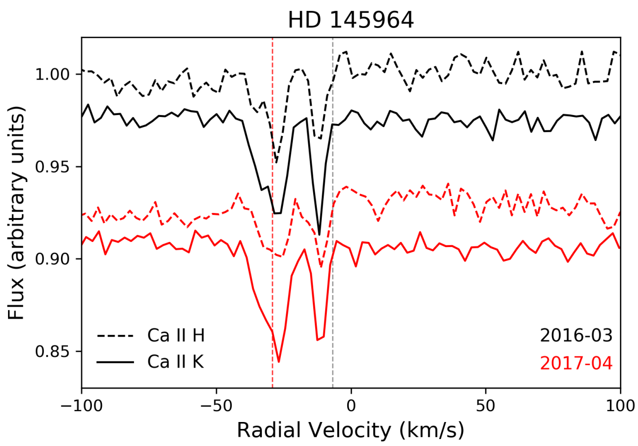

Fig. 22: Spectra of HD 145964 colour coded as indicated in the labels for Ca ii K & H lines (continuous and dashed lines, respectively), and obtained with HERMES. An offset of 0.05 was introduced in the Y-axis to better perceive the variations between both dates, and 0.02 between the K and H lines. The red and grey vertical lines correspond to the radial velocity of the star and the velocity vector of the G Colorado cloud.

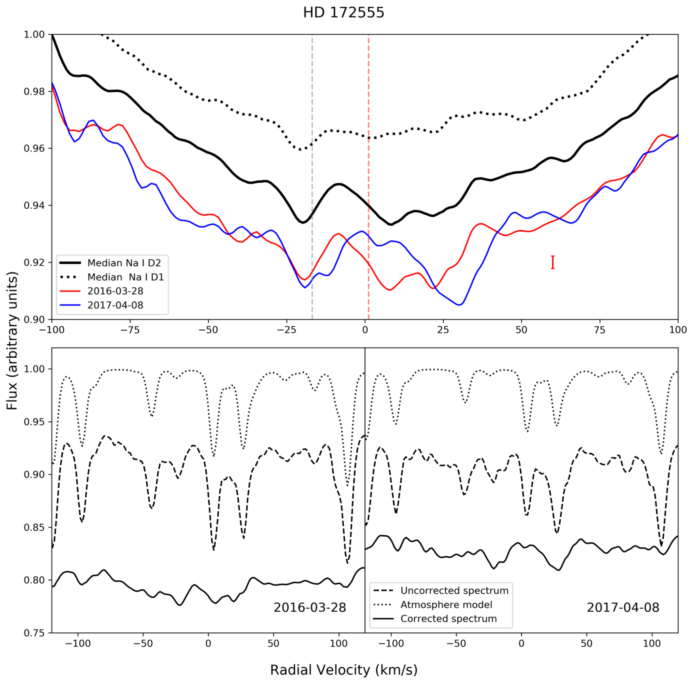

Fig. 23: Top panel: Absorptions detected in the Na i D2 line of HD 172555. Black lines corresponds to the median of all spectra for Na i D2 (solid line) and D1 (dotted line). Blue and red lines correspond to two different dates, where the variations in the ~15 km/s Na i D2 component can be perceived. Bottom panel: Examples of the telluric subtraction are plotted, in order to show that this process it is not the source of the variability. In both cases, spectra were obtained using FEROS. Red and grey vertical lines mark the stellar and ISM radial velocities respectively.

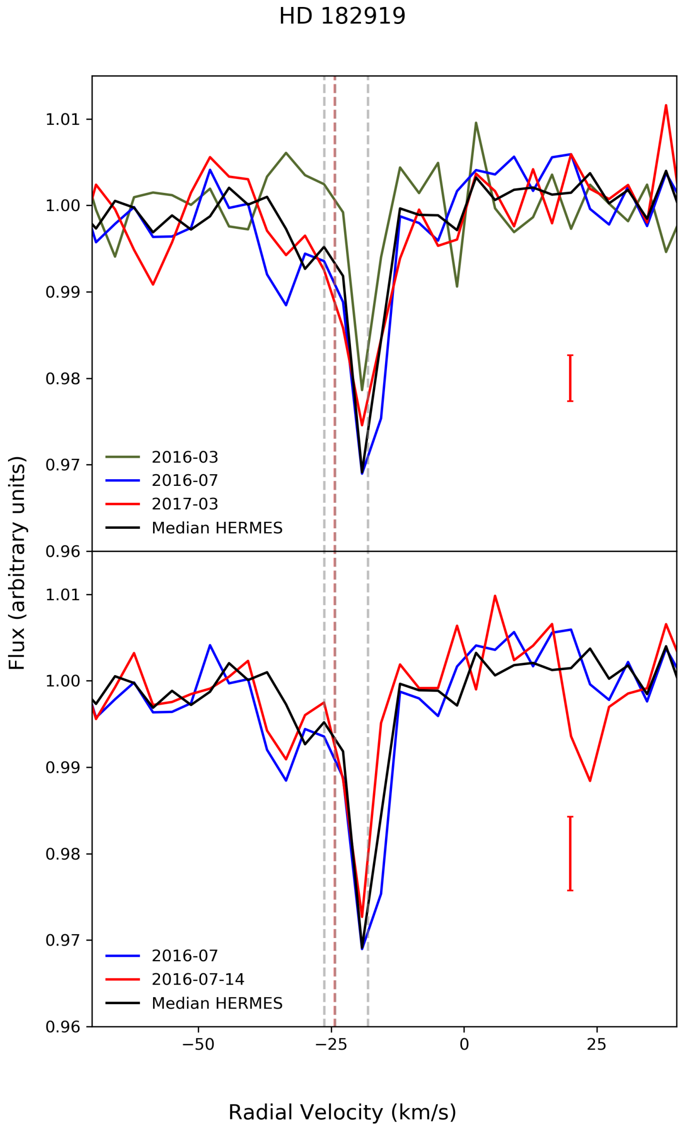

Fig. 24: Ca ii K spectra of HD 182919 (5 Vul) taken with HERMES in the dates indicated in the labels. Top panel shows the variation of the features at ~ –18 and ~ –35 km/s. In the bottom panel it is visible a possible FEB-like event at ~ 25 km/s. The red and grey lines correspond to the radial velocity of the star and the velocity vector of Colorado clouds, respectively.

Two of them, blue-shifted with respect to the radial velocity of the star, are also detected in Na i. The weakest feature at 5.1 km/s is at the stellar v_{rad} and the velocity vector of the Hyades ISM cloud (Table B.3). While the stronger and narrower -9.3 km/s Ca ii K feature remains unchanged (variations below 1σ), the -16.5 and likely the 5.1 km/s components present some variability (Fig. 25). Particularly, the -16.5 km/s feature seems to experience some dynamical evolution changing its depth and velocity within hours, e.g. up to 3 σ EW variation along the night $6^{th}/7^{th}$ September 2015, as well as a shape and depth change (Fig. 25, bottom left panel). Similar changes are also seen on other nights. Those changes, although much less remarkable, can tentatively be present in the weaker Ca ii H feature, as seen in Fig. 26 where both Ca ii non-photospheric lines of the mentioned night are shown. These results suggest the presence of CS gas around 2 And. Cheng & Neff (2003); Montgomery & Welsh (2012); Welty et al. (1996) found similar UV/optical results.

4.3. Summary of CS gas detections

Fig. 1 (Cont.) shows the observed median Ca ii K&H and Na i D lines and the non-photospheric residuals, once the stellar contribution has been subtracted, of the 60 stars that have narrow stable absorptions; radial velocities of the stars and the velocity vector of the ISM Colorado clouds velocities are also plotted. Table B.3 gives radial velocities, FWHM, equivalent widths, and column densities of the narrow features. Table 2 lists the stars showing variable absorptions detected in this work, and also the stars reported in the literature as hosting sporadic events but not detected by us.

We find evidence of hot CS gas in 32 objects out of the initial sample of 117 stars, being 30 in the form of stable non-photospheric components, and variable absorptions in the other two cases. Variable red- and/or blue-shifted events with respect to the radial velocity of the stars have been detected in 18 objects, including the serendipitous detection of HD 132200, which was not in the initial sample (Rebollido et al. 2018). Among those 18 objects, all but HD 110411 and HD 183324, also have stable narrow features. These figures mean we have found evidence of a close-in gaseous CS environment in ~27% of the sample. We note, however, that it is not statistically significant as the selection criteria were highly biased, for instance includ-

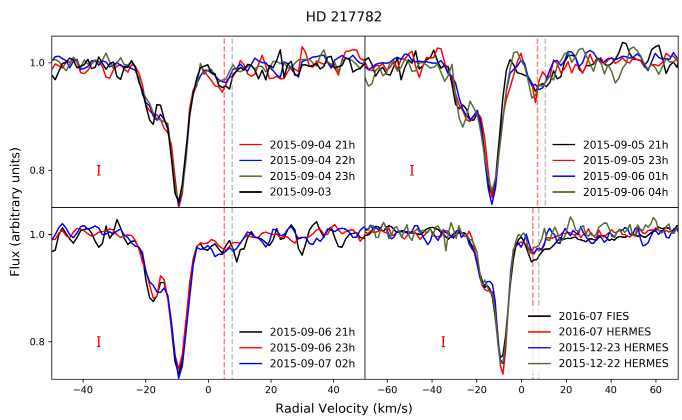

Fig. 25: Ca II K spectra of HD 217782 as indicated in the labels. In the bottom right panel the labels indicate the instrument used in each case. The rest of the spectra were obtained with HERMES. The dashed red and grey lines correspond to the radial velocity of the star and the velocity vector of Colorado clouds, respectively.

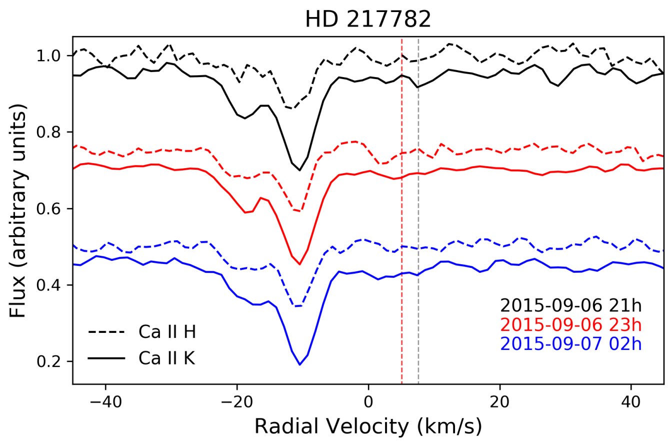

Fig. 26: Ca II H and K non-photospheric features of HD 217782 taken during the night indicated in the labels. All spectra were taken using HERMES. A shift of 0.2 was introduced in the Y-axis to help differentiate the variations. The dashed red and grey lines correspond to the radial velocity of the star and the velocity vector of Colorado clouds, respectively.

ing stars for which the presence of hot or cold CS gas was already known. Nonetheless, the figure does indicate that a non-negligible amount of stars, particularly A-type (see below), are surrounded by CS gas which can be detected by means of high resolution optical spectroscopy. We note that we are not considering the 8 stars where the detected narrow feature has a dubious origin as we are unable to soundly attribute it either to a CS or/and ISM environment.

The detected CS gas clearly has distinct origins. Red- and blue-shifted events are plausibly linked to the presence of FEBs, as in the well known case of β Pic; even in some cases our spectra likely trace the dynamical evolution of those exocomets, i.e., a change in depth and velocity. In none of the cases the exocomet activity is as rich as in β Pic, which remains unique in this context. Stable absorption features in some stars are also likely related to exocomets and/or evaporation of grains in the immediate CS environment. In the case of shell stars, the non-photospheric stable features, including many metallic shell lines of species like Fe II or Ti II, are related to the shell itself, and likely arising from mass loss phenomena experienced by the central star. Nonetheless, some shell stars also present sporadic red- or blue-shifted absorption events in Ca II reminiscent of exocomets. HD 37306 represents an extreme case, where we detected the appearance and disappearance of a strong shell spectrum but no trace of any exocomet-like event.

5. Discussion

While our stellar sample is heterogeneous and highly biased we can still try to find some trends among the incidence of CS gas and some general properties of the stars, and the different groups of stars according to the selection criteria.

Fig. 27 shows the HR diagram of the sample where the absolute magnitude M_V and colour index B-V are estimated from the magnitudes and parallaxes given in SIMBAD; the MS track is taken from Pecaut & Mamajek (2013). To estimate M_V we have not taken into account the potential extinction towards the stars; nonetheless, the true loci of the individual stars in the HR diagram would not significantly alter the conclusions. Objects with evidence of hot CS gas (variable or stable) are A-type stars, and are therefore located in the upper-left region of the diagram. This is in line with previous works, although as far as we know they have only been concentrated in the study of A-type stars (e.g. Holweger et al. 1999; Welsh & Montgomery 2018, and references therein). We only know of one later spectral type star, HD 109085 (η Crv, F2 V) for which one exocometary-like event has recently been reported although it requires confirmation (Welsh & Montgomery 2019); while cold CO is most likely present in this system (Marino et al. 2017), we do not find any trace of CS gas associated with this star (Rebollido et al. 2018, this work). In this respect, photometric transits are more efficient than spectroscopy to detect exocomets around later type stars (e.g. Rappaport et al. 2018; Ansdell et al. 2019). The inability, at least up to now, of spectroscopy to detect exocomet signatures in late-type stars might be due to the concurrence of several causes, e.g. stellar activity that makes it extremely difficult to detect faint variable events superimposed on the profiles of the chromospheric active Ca II and Na I lines; also, late type stars usually have small rotational velocities so that narrow stable absorptions are practically indiscernible from the core of the narrow stellar lines.

It is obvious from Fig. 27 that stars with both stable and/or sporadic CS features tend to be in many cases located above the main sequence, in the δ Scuti instability strip of the HR diagram (Breger 1979; Rodriguez et al. 1994). A few of the hot-gas-bearing stars in our sample are identified as δ Scuti stars in SIMBAD - HD 110411, HD 183324, and HD 192518; recently, Mellon et al. (2019) have found that HD 156623 is also a δ Scuti star; we also point out that β Pic itself has δ Scuti pulsations (Koen 2003; Mékarnia et al. 2017). In addition, the CS gas stars have distinctly larger $v \sin i$. As expected, (e.g. Nielsen et al. 2013), the highest $v \sin i$ values are found for the earlier spectral types (symbol sizes in Fig. 27 are proportional to v sin i). Excluding stars later than F2, Fig. 28 shows the cumulative distribution functions (CDF) of the projected rotational velocity of the early type stars without non-photospheric features, stars with features identified as ISM absorptions, and stars with variable events. It is evident from Fig. 28 that stars with non-photospheric ISM features or with variable CS events, have larger $v \sin i$ values than stars without non-photosperic features. Table 3 shows the results of a Kolmogorov-Smirnov test separating those three subsamples. We refer to Maldonado et al. (2012)

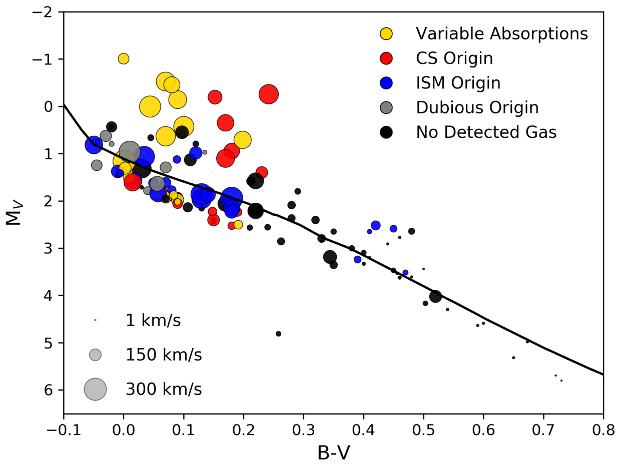

Fig. 27: Colour-Magnitude diagram of the whole sample. Colours represent stars with different non-photospheric features while the size of the symbols is proportional to $v \sin i$.

for the meaning of the parameters D, p-value, and n_{eff} in that table. In particular, the p-value indicates that the subsample of stars with ISM absorptions differ with a probability of ∼97%, of the stars without non-photospheric absorptions; for the case of stars with variable events the probability is practically 100%. At the same time, the results of the Kolmogorov-Smirnov test indicates that the ISM and variable events subsamples do not differ significantly. Nonetheless, a visual inspection of Fig. 28 suggests that there might be a paucity of the variable hot-gas-bearing stars with $v \sin i$ up to ∼150 km/s with respect to the sample of stars with ISM absorptions, which is lost in the statistical test when comparing the whole range of $v \sin i$.

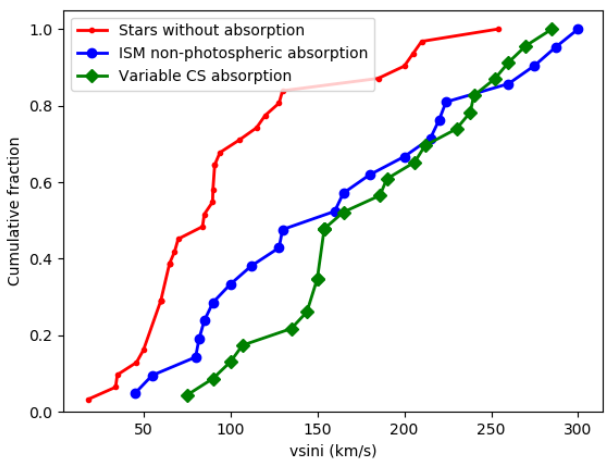

Fig. 28: Cumulative distribution functions of the subsamples labelled in the plot.

When considering the age of all stars with non-photospheric CS and ISM absorptions, ∼58% have ages below 100 Myr (Table B.1). If we just consider stars plausibly hosting CS features that figure is ∼51%, and reduces ∼42% (11 out of the 26 stars) when the stars with variable features are considered. Thus, although ages of field stars might be highly uncertain and the nature of the variability of the features is not always due to exocomet-like events, e.g. the case of HD 37306, stars with FEB-like events do not tend to be young objects but they are distributed in a wide range of ages, from ∼10 Myr to ∼1 Gyr. All this is clearly recognized in Figure 29 where a plot of the rotational velocity of the stars (up to F2) versus age is shown. Stars with non-photospheric features are all younger than 1000 Myr, and its distribution is clearly modulated by stars in young clusters - mainly UpSco, UCL, BPMG and Tuc-Hor. Stars with CS features are found among the whole range of ages, and have higher rotational velocities than stars without non-photospheric features. They also appear to have higher rotational rotational velocities than stars with ISM features, in fact reflecting the results of the Kolgomorov-Smirnov test above, and the mentioned paucity of CS-feature stars with low $v \sin i$.

Table 3: Kolmogorov-Smirnov test comparing the projected rotational velocity distribution of the subsample of stars earlier than F2 without non-photospheric features, stars with absorptions with an ISM origin, and stars with variable events.

Sample 1	Sample 2	D	p-value	n_{eff}
ISM absorp.	No absorp.	0.39	0.030	12.52
CS Var. absorp.	No absorp.	0.66	6.376e-06	12.20
ISM absorp.	CS Var. absorp.	0.30	0.222	10.98

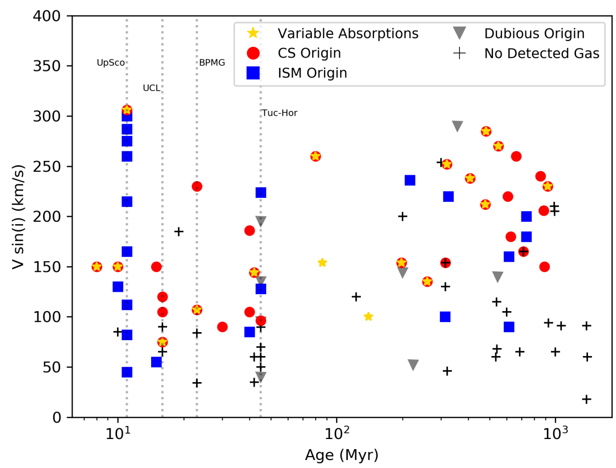

Fig. 29: Age versus $v \sin i$ of the stars in the sample. Symbols mark the type of absorptions detected for each object. Vertical dotted lines mark the location of some of the young associations: Upper Scorpious, Upper Centaurus Lupus, Beta Pic Moving Group and Tucana-Horologium.

Out of the 32 stars in our sample with non-photospheric absorptions, we find in many cases coincident radial velocities (within the errors reported in Sect. 4.1) between the features observed in Ca and in Na. Fig. 30 shows the ratio of Ca II K and Na I D2 column densities against the Ca II K column density, colour coded for the attributed origin. In those cases where only one of the lines was detected, an upper limit was calculated using the EW uncertainty to compute the column density. The distribution of the stars in this diagram is consistent with other works (e.g. Welsh et al. 2010; Gudennavar et al. 2012). There is no clear separation between CS or ISM absorptions, i.e., the ratios of their column densities do not show any significant trend when comparing them regarding their origin, in agreement with previous results (see section 4.1.1, first paragraph). It is worth noticing though, that it seems that the presence of both Ca and Na components is more common in ISM absorptions. HD 42111 seems to behave as an extreme outlier in our sample as it has a large $N_{\text{Caii K}}$. However, this shell star has two practically blended narrow, absorptions (not discernible in the median spectrum), which might explain the large $N_{\text{Caii K}}$.

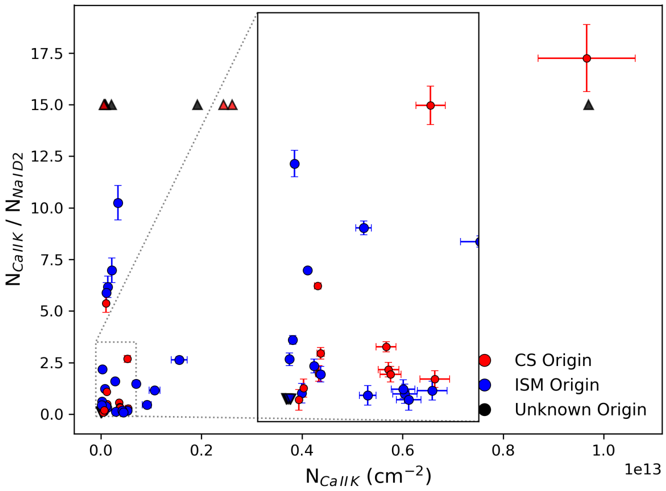

Fig. 30: Column densities of Ca ii K and ratio of column density of Ca ii K and Na i D2 of those absorptions of similar radial velocities. For the case where an absorption was detected in only one of the lines, triangles pointing up are upper limits and triangles pointing down are lower limits. The outlier in the upper-left corner of the plot is HD 42111. Colour denotes the suggested origin as in the legend.

While objects in the sample are distributed in the sky without preferential locations (Fig. 1), we find a possible trend when examining distances. Stars without narrow absorptions (either CS or ISM) are located at < 50 pc, but there is no clear differentiation between stars with CS and ISM narrow absorptions. This could be due to the lower frequency of interstellar clouds at shorter distances, and the exponential growth of the number of stars with distance.

5.1. Stars with debris discs

To our knowledge, 76 out of the 117 stars in the sample are associated with a known debris disc (Table B.1). We find that 35 out of those 76 debris discs have at least a non-photospheric narrow feature (Table B.3 and Table 4), and 15 among these 35 debris disc stars plausibly have at least one CS component - this figure does not include stars with an ambiguous origin of the detected non-photospheric absorptions. Stable CS features at the velocity of the star have been interpreted as proof of a CS gas disc, and its persistence requires the presence of a braking mechanism that prevents the hot gas from being blown away by the strong radiation pressure from the star (e.g. Lagrange et al. 1998). Fernández et al. (2006) suggested that in β Pic such mechanism could be exerted by the observed enhanced carbon abundance (see also Roberge et al. 2006; Brandeker 2011), a fact also suggested for HD 9672 (Roberge et al. 2014). Among the stars in our sample with stable features, in addition to HD 9672 and HD 36546 (see section 4.2), that scenario might be at work for HD 32297, where

Table 4: Debris disc stars in the sample with narrow non-photospheric features. Bold-faced stars have features of CS origin, and those in italics also have variable absorptions. HD 110411 and HD 183324 do not have narrow absorptions but have CS gas.

HD 3003	HD 118232	HD 146897
HD 5267	HD 125162	HD 147137
HD 9672	**HD 131488**	***HD 156623***
HD 21620	HD 131835	**HD 158352**
HD 32297	HD 138813	***HD 172555***
HD 36546	HD 142315	**HD 181296**
HD 37306	HD 144587	***HD 182919***
HD 71043	HD 144981	***HD 183324***
HD 71722	HD 145554	HD 188228
HD 105850	HD 145631	HD 198160
HD 109573	**HD 145689**	HD 221756
HD 110058	***HD 145964***	
HD 110411	HD 146606	

a carbon overabundance is suggested by the the 3.7σ Herschel detection of [C ii] emission at 158 μm (Donaldson et al. 2013).

Concerning variable absorptions, 12 out of the total 18 stars showing variability either in one or both of the Ca ii H&K lines or in one or both of the Na i D lines, have as well excesses associated with the presence of a debris discs (Table 4 and Table 2). All these stars are younger than 200 Myr.

In all cases, but HD 37306, transient red- or blue-shifted events attributed to exocomets have been observed. The observed variability in HD 37306 is due to the appearance, and later disappearance, of a strong shell spectrum (see above). Complementary to these results, the rest of the stars with variable features listed in Table 2, i.e. 14 stars, do not host a debris disc, and are older than 200 Myr. We point out, however, that in four cases - HD 39182, HD 64145, HD 132200, and HD 138629 - there is no observational information concerning the potential presence of a debris disc, and in two cases - HD 132200 and HD 138629 - we do not have information about their age.

In parallel, to our knowledge 36 out of the 76 debris discs have been spatially resolved after the compilations by N. Pawellek and A. Krivov[4], and C. McCabe, I.H. Jansen, and K. Stapelfeldt[5]. Further, 28 out of those 36 resolved debris disc stars have spectral types earlier than F2 and, therefore, sensitive to show the presence of exocometary signals. Also, Moór et al. (2017) reported inclinations for the A1 stars HD 121617 and HD 131488. Table 5 lists the early-type 30 resolved debris discs together with their corresponding inclination angles, taken from the mentioned catalogues. Among the resolved discs, 17 have non-photospheric features (Table 5). In 6 cases the absorption features are more plausibly interstellar or ambiguous - HD 71722, HD 125162, HD 131835, HD 138813, HD 146897, and HD 188228. In 11 stars, a CS origin seems to be the most reasonable one, for at least one of the observed non-photospheric absorption features; 8 out of these 11 stars have variable absorptions. Although based on a relatively low number of objects, an inspection of the inclination angles in Table 5 reveals: i) there is no a preferential distinction between discs seen edge- or polar-on for those debris discs without non-photospheric absorptions;

[4] https://www.astro.uni-jena.de/index.php/theory/catalog-of-resolved-debris-disks.html
[5] https://www.circumstellardisks.org/

Table 5: Resolved debris discs and inclination angles. Bold-faced are those with narrow non-photospheric absorption features while those in italics have at least one component attributed to a CS origin. HD 110411 and HD 183324 do not have narrow absorptions but have CS gas.

Star	i^o	star	i^o	star	i^o
HD 9672	79	**HD 71722**	78	***HD 131488***[2]	82
HD 14055	83	HD 74873	27	**HD 131835**	75
HD 15115	80	HD 95418	84	HD 139006	80
HD 21997	26	HD 102647	30	***HD 138813***	28
HD 27290	69	HD 109085	35	**HD 146897**	84
HD 28355	76	***HD 109573***	76	***HD 156623***	30
HD 31295[*,1]		***HD 110058***†	50	***HD 172555***	75
HD 32297	90	*HD 110411*	70	***HD 181296***	90
HD 36546	75	HD 121617[2]	37	*HD 183324*	2
HD 38206	60	**HD 125162**	48	**HD 188228**	49

(*) resolved debris disc with unreported inclination angle; (†) Kasper et al. (2015) report an edge-on inclination
(1) Draper et al. (2016); (2) Moór et al. (2017)

Table 6: Stars showing near-IR excesses.

Name	Non-photospheric absorption	H/K excess
HD 2262	Yes*(1)	(2)
HD 28355	No	(2)
HD 40136	No	(1)
HD 56537	Yes(2)	(1)
HD 102647	No	(1)
HD 108767	Yes(2,3)	(2)
HD 172555	Yes(3,4)	(2)
HD 177724	Yes(3)	(1,3)
HD 187642	No	(1,3)
HD 203280	No	(1)
HD 210418	Yes(3)	(3)

*Not clear if exocomet-like or stellar mass loss events.
References for non-photospheric absorptions: (1): Welsh & Montgomery (2018); (2): Welsh & Montgomery (2015); (3) This work ; (4) Kiefer et al. (2014a)
References for H/K excess: (1): Absil et al. (2013), (2): Ertel et al. (2014), (3) Nuñez et al. (2017)

ii) similar result is seen for those stars with ISM features; and iii) the trend is clearly different when we inspect debris discs with CS absorptions, i.e., most of them are clearly seen at $i > 70°$ ($\sim$ 72%), and this trend is reinforced when only those discs with variable features are considered. In other words, debris discs associated with stars hosting CS absorptions tend to be seen edge-on, while debris discs associated with stars without non-photospheric absorptions or stars with ISM features do not show a preferential inclination. This result is consistent with the fact that the detection of CS features, i.e. hot gas, is favoured when the systems are seen close to edge-on, as well as with the large projected rotational velocities shown by the stars with CS gas compared to those without such gas. We note that the observed trend, which is just a geometrical effect, does not exclude the existence of hot gas, i.e. the eventual existence of comet-like bodies around the debris discs systems seen away from edge-on. A similar trend was already pointed out by Rebollido et al. (2018) in their analysis of debris discs with measurable amounts of cold gas seen in emission in the far-IR and (sub-) mm wavelength regimes.

5.2. Near infra-red excesses

There are 22 stars (Table B.1) in our sample explicitly taken from the literature searching for hot excesses in the H (1.6 μm) and K(2.2 μm) bands (Table B.1). In addition, HD 172555 also presents such excess (Absil et al. 2013; Ertel et al. 2014, 2016; Nuñez et al. 2017).

Within the stars in our sample with near-IR excesses plausibly due to hot dust (i.e., excluding stars where binarity is the cause of the excess), 11 stars have spectral types earlier than F2, and 6 out of those 11 stars present non-photospheric features, either detected in this work or in previous ones (Table 6).

To assess the significance of the incidence of CS absorption around hot dust stars we consider all reported 31 near-IR excess stars (Absil et al. 2013; Ertel et al. 2014; Nuñez et al. 2017). Excluding the binaries, 14 stars - the 11 studied by us plus Vega, β Pic, and HD 210049 (μ PsA) - have spectral types earlier than F2. Among those 14 stars, 5 have variable absorptions features (HD 2262, HD 56573, HD 108767, HD 172555, and β Pic); 2 stars have an ambiguous CS/ISM narrow feature (HD 177724, and HD 210418); 2 stars are associated with pole-on debris discs (HD 102647 and Vega), i.e. an unfavourable orientation to detect CS features; 1 star (HD 28355) has a resolved debris disc with an inclination angle $i = 70°$, but our spectra do no reveal any non-photospheric absorption; for the last 4 stars (HD 40136, HD 187642, HD 203280, and HD 210049) the orientation of the system is unknown. If we assume random orientations, the probability to observe a system with an inclination larger than 65°–70°, i.e., edge-on or close to it, lies between $\sim$42% and 34%, respectively, which is similar to the percentage of stars with hot CS gas among the hot dust stars. We also note that it agrees with the percentage of edge-on discs, either debris or other type of disc, that can be found in the Catalogue of Resolved Discs compiled by C. McCabe, I.H. Jansen, and K. Stapelfeldt. Given those figures, a relationship between hot dust and hot CS gas is suggested, which should be confirmed by increasing the sample of stars with the appropriate near-IR interferometric and UV/optical spectroscopic data.

5.3. Ti II / Shell stars

In addition to the stars selected on the basis of their Ti II lines, there is a number of stars which have been classified as shell stars (Abt 2008; Lagrange-Henri et al. 1990c; Hauck & Jaschek 2000; Roberge & Weinberger 2008). Table 7 lists, according to our knowledge, the shell stars in our sample. No Ca II or Na I non-photospheric absorptions are observed towards HD 39283 and HD 77190; in the cases of HD 118232 and HD 196724 the origin of the Ca II absorption is likely ISM or ambiguous. As a matter of fact, the spectra of these four stars do not reveal any prominent shell-like characteristics. The rest of the stars show triangular-like CS absorptions (bold-faced in the table) - those stars with variable features are also emphasized. Not all absorptions can be attributed to FEB-like events; for example, the stable absorption seen towards HD 192518 is clearly formed in a gaseous shell, while as already mentioned the variability in HD 37306 is due to the appearance/disappearance of a shell around this star. Nonetheless, 11 stars do present variable events, most of them attributable to exocomets; even, our spectra might be tracing their dynamical evolution of some events by changing their depths and velocities.

Table 7: Shell stars. Stars with non-photospheric CS features are bold-faced while those with variability are emphasized.

Star	Star	Star
HD 256	***HD 50241***	***HD 148283***
HD 21688	HD 77190	**HD 158352**
HD 37306	***HD 85905***	**HD 168646**
HD 39182	***HD 98058***	**HD 192518**
HD 39283	HD 118232	HD 196724
HD 42111	***HD 138629***	***HD 217782***

5.4. λ Boo stars

The sample contains 12 objects previously classified as λ Boo type stars (Table 8) although three of them - HD 39283, HD 210418, and HD 217782 - have recently been considered as non-members of this stellar class (Murphy et al. 2015b, and references therein). Several criteria have been used to classify λ Boo stars (e.g. Murphy et al. 2015b; Gray et al. 2017); among them, optical line ratios between volatiles, like CNO, and heavier elements (e.g. Mg) are useful to ascribe stars to this stellar class (Cheng et al. 2017). This criterion is based on the basic definition of the λ Boo stars, i.e. stars with a remarkable low abundance of heavy (e.g. Fe, Al, Mg) elements while volatiles as CNO have near solar abundances (Baschek & Slettebak 1988, e.g.). In order to eventually find new λ Boo candidates, we have measured in all stars earlier than F2 in our sample the ratio of the Mg II 4481 Å and the O I 7774 Å triplet, which are strong and easy to measure in our spectra.

Fig. 31 is a plot of the EW of the O I line versus the ratio of Mg II to O I lines. All identified λ Boo stars in the sample are clearly located to the left in that plot, well separated from the bulk of the stars. The exception is HD 145964 classified as *weak* λ Boo by Welsh & Montgomery (2013) based on the measurements of Abt & Morrell (1995). The identified λ Boo stars have low metallicities ([Fe/H] < –0.25) excluding HD 145964 and HD 217782. A vertical dashed line at MgII /O I< 0.49 marks the limit for the identified λ Boo objects in our sample. This figure is the one for the λ Boo stars HD 198160 and HD 198161, and approximately the one for those removed from the class by Murphy et al. (2015b) stars. We note that 6 stars are additionally located at similar locations in Fig. 31 as the λ Boo stars, and they also have low metallicities (Table B.2). We consider that those stars are new candidates, Table 8. In addition, 3 shell stars -HD 39182, HD 42111, and HD 168646 - have low Mg II/O I ratio but a very high EW (O I), and metallicities >0.0.

With respect to the presence of non-photospheric narrow and/or variable features, 15 out of the 18 λ Boo stars (including the new candidates) listed in Table 8 present evidences of non-photospheric gas in their spectrum; in 5 cases the feature is interstellar, in 2 cases the origin is ambiguous; and the remaining 8 stars (44% of the λ Boo stars), have exocometary-like events. Comparing this figure to the 26% incidence of exocometary-like events of the whole sample, there seems to be an enhanced probability for λ Boo stars to have such events. A connection between metal-poor stars and the presence of debris discs or remainings of planet formation processes has been suggested before in the literature (Jura 2015; Murphy & Paunzen 2017), as heavier elements are blown away by radiation pressure, while volatile elements are accreted onto the star (see Draper et al. 2016, and references therein). Therefore, exocomets represent a rather likely scenario, that could replenish the atmosphere of λ Boo stars of C, N, O and S elements.

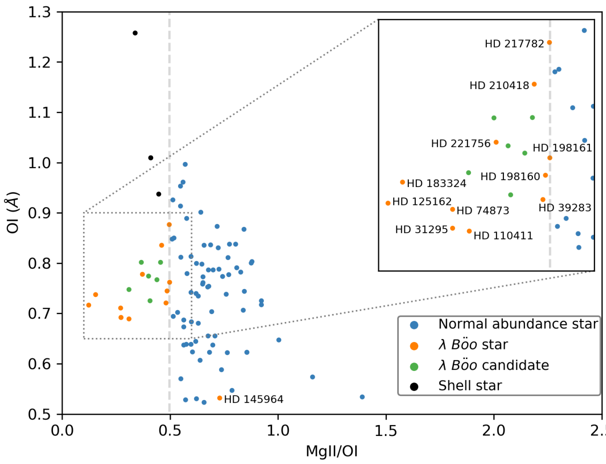

Fig. 31: Ratio O I (7744 Å) and Mg II (4481 Å) versus the EW of O I. Orange dots mark stars previously classified as λ Boo stars; green dots mark new λ Boo candidates; and blue dots mark the stars with normal abundances. The vertical dashed line delimits the locus of bona fide λ Boo stars (see text).

Table 8: EW of the Mg II 4481 Åand O I 7744 Ålines of previously known λ Boo stars, together with stars of the sample with similar characteristics. The new λ Boo candidates are indicated.

Star	EW Mg II (Å)	EW O I (Å)	λ Bö*o*
HD 31295	0.188	0.692	Yes
HD 32297	0.336	0.767	New
HD 36546	0.231	0.748	New
HD 39182	0.413	1.010	Shell
HD 39283	0.347	0.720	Yes
HD 42111	0.424	1.258	Shell
HD 71722	0.294	0.802	New
HD 74873	0.192	0.711	Yes
HD 110058	0.310	0.774	New
HD 110411	0.213	0.689	Yes
HD 125162	0.087	0.717	Yes
HD 145964	0.388	0.532	Yes
HD 156623	0.366	0.802	New
HD 168646	0.418	0.937	Shell
HD 177724	0.294	0.726	New
HD 183324	0.114	0.738	Yes
HD 198160	0.362	0.745	Yes
HD 198161	0.378	0.762	Yes
HD 210418	0.385	0.836	Yes
HD 217782	0.435	0.877	Yes
HD 221756	0.289	0.778	Yes

6. Conclusions

We have presented the observational results of a systematic study aiming at detecting and monitoring hot gas attributed to the presence of exocomets in the CS environment. The study has been based on the analysis of the Ca II K&H and Na I D lines in a heterogeneous and biased sample of 117 main-sequence late B to G type stars. This is the largest systematic study searching for exocomets carried out so far. The main results are the following.

Narrow non-photospheric ISM or CS absorptions have been detected towards ~50% of the sample (60 stars). Among the stars with those absorptions, at least one of the detected narrow features can be attributed to CS gas in 30 objects, i.e., 26% of the whole sample. This figure is not statistically significant as the studied sample included stars with previously detected CS gas, but it does show that gas in the CS environment of A-type stars is relatively common. In some stars, the gas is originated in a CS shell surrounding the stars; in some other cases, the narrow absorptions can be attributed to the evaporation of exocomets or to gas released by dust grain collisions or evaporation.

Sporadic red-shifted and blue-shifted events that in some cases (but not all) might be due to β Pic-like exocomets have been found in the CS environment of 16 stars, out of which 6 are new to the literature (including HD 132200, not contained in the original sample). In a few cases, our spectra seem to trace the dynamical evolution of such events as suggested by changes in their velocity and depth. Nonetheless, the exocometary-like activity in our stars, maybe with the exception of ϕ Leo (see Eiroa et al. 2016), is very poor compared with β Pic, which remains a unique object.

The variations observed towards the two other stars, namely HD 256 (HR 10) and HD 37306 (HR 1919) do not require the presence of exocomets for their interpretation. The variability of the CS features in HR 10 is mainly due to the binary character of this star. A detailed analysis has being carried out in a separated paper (Montesinos et al. 2019). In the particular case of HD 37306, our spectra have witnessed the appearance and disappearance of a strong shell around this star. There are no hints in our data of exocometary events in this star, although we point out that some shell stars in our sample do show such events.

Hot CS gas is only detected towards stars earlier than A9, in line with previous works. The F2 V star η Crv is the only star for which β Pic-like events with a 2.9σ detection have been claimed (Welsh & Montgomery 2019). This paucity in detecting exocometary events around late type stars might be due to the inability of spectroscopy to detect faint non-photospheric absorptions on top of cool photospheres. In this respect, photometric transits have demonstrated to be competitive and successful in detecting exocomets around late type stars.

Hot gas-bearing main sequence stars have distinctly higher projected rotational velocities, and spread over a large range of ages, from ~10 Myr up to at least ~1 Gyr. Some of them are also known to present δ Scuti pulsations, as β Pic itself.

Exocometary-like events are often associated with edge-on debris disc stars, in particular towards those with cold gas (see also Rebollido et al. 2018). This result is interpreted as a geometrical effect, but it does suggest that debris disc stars with non-photospheric absorptions (i.e. hot gas) are excellent targets to search in the far-IR and (sub-)mm spectral range for the presence of cold gas released by the evaporation of solid bodies at distances relatively far from the central star. We note that not all stars with FEB-events are associated with a debris disc. It cannot be excluded that this is due to the current, limited sensitivity to detect debris discs, $L_{dust}/L_* \sim 10^{-6}$.

We find that FEB-like events are detected towards 17% of stars with near-IR excesses denoting the presence of hot exozodies. Both hot dust and gas might be related phenomena, although more observations are needed to confirm or deny the trend pointed out in our study.

Our sample includes 18 λ Bootis stars, with 6 new candidates found in this work. A relevant fraction of them, 8 out the 18 stars, have FEB-like events, suggesting again that both phenomena could be related.

Acknowledgements. The authors wish to thank the careful reading of the manuscript and comments by the referee which have helped to improve the content of this work. Based on observations made with the Mercator Telescope, operated on the island of La Palma by the Flemmish Community, and the Nordic Optical Telescope, operated by the Nordic Optical Telescope Scientific Association, at the Spanish Observatorio del Roque de los Muchachos of the Instituto de Astrofísica de Canarias. Based on observations made with ESO Telescopes at the La Silla Observatory under programmes 099.A-9029(A),099.A-9004(A) and 094.A-9012. Also based on observations made with the TIGRE telescope funded and operated by the Universities of Hamburg, Guanajuato and Liège. We thank David Montes for providing the December 2018 Mercator spectra and to Santos Pedraz and Ana Guijarro for the CARMENES spectra of HD 37306. We thank Sam Kim and Markus Rabus for the FEROS spectra obtained in September 2017. I.R. thanks Angela Hempel for her support with FEROS observations in March 2016 and April 2017, and the Calar Alto Observatory staff, where a large part of this paper was written. Partially based on data obtained from the ESO Science Archive Facility, programs 096.C-0876, 076.B-0055, 185.D-0056, 082.B-0610, 072.C-0488, 0100.C-0090, 093.C-0409, 081.D-0610, 080.A-9006, 184.C-0815, 077.C-0295. C.E., G.M., B.M., I.R., and E.V. are supported by Spanish grant AYA 2014-55840-P. H.C. acknowledges funding from the ESA Research Fellowship Programme. J. O., A. B., and D. I. acknowledge support from the ICM (Iniciativa Científica Milenio) via the Nucleo Milenio de Formación planetaria grant. J. O. acknowledges support from the Universidad de Valparaíso and from Fondecyt (grant 1180395). A. B. acknowledges support from Fondecyt (grant 1190748). A. M. acknowledges the support of the Hungarian National Research, Development and Innovation Office NKFIH Grant KH-130526. This research has made use of the SIMBAD database, operated at CDS, Strasbourg, France. This work has used Seth Redfield's Colorado model of interstellar clouds and his online tool "LISM Kinematic Calculator". This work has also used the debris disc catalogues "Resolved debris discs" from Jena University compiled by N. Pawellek and A. Krivov; and the one in circumstellardisks.org compiled and mantained by C. McCabe, I. H. Jansen and K. Stapelfeldt.

References

Absil, O., Defrère, D., Coudé du Foresto, V., et al. 2013, A&A, 555, A104
Absil, O., di Folco, E., Mérand, A., et al. 2006, A&A, 452, 237
Abt, H. A. 2008, ApJS, 174, 499
Abt, H. A. & Morrell, N. I. 1995, The Astrophysical Journal Supplement Series, 99, 135
Abt, H. A. & Moyd, K. I. 1973, ApJ, 182, 809
Abt, H. A., Tan, H., & Zhou, H. 1997, ApJ, 487, 365
Ansdell, M., Gaidos, E., Jacobs, T. L., et al. 2019, MNRAS, 483, 3579
Armitage, P. J. 2010, Astrophysics of Planet Formation
Ballering, N. P., Rieke, G. H., Su, K. Y. L., & Montiel, E. 2013, ApJ, 775, 55
Baschek, B. & Slettebak, A. 1988, A&A, 207, 112
Bell, C. P. M., Mamajek, E. E., & Naylor, T. 2015, MNRAS, 454, 593
Bertin, P., Lallement, R., Ferlet, R., & Vidal-Madjar, A. 1993, A&A, 278, 549
Beust, H., Lagrange, A.-M., Crawford, I. A., et al. 1998, A&A, 338, 1015
Beust, H. & Morbidelli, A. 2000, Icarus, 143, 170
Beust, H., Vidal-Madjar, A., & Ferlet, R. 1991, A&A, 247, 505
Beust, H., Vidal-Madjar, A., Ferlet, R., & Lagrange-Henri, A. M. 1990, A&A, 236, 202
Bochanski, J. J., Faherty, J. K., Gagné, J., et al. 2018, AJ, 155, 149
Bonsor, A., Raymond, S. N., Augereau, J.-C., & Ormel, C. W. 2014, MNRAS, 441, 2380
Boyajian, T. S., LaCourse, D. M., Rappaport, S. A., et al. 2016, MNRAS, 457, 3988
Brandeker, A. 2011, ApJ, 729, 122
Brandeker, A., Liseau, R., Olofsson, G., & Fridlund, M. 2004, A&A, 413, 681
Breger, M. 1979, PASP, 91, 5
Cataldi, G., Moór, A., Ohashi, N., et al. 2019, Research Notes of the American Astronomical Society, 3, 39
Chen, C. H. & Jura, M. 2003, ApJ, 582, 443
Chen, C. H., Mittal, T., Kuchner, M., et al. 2014, ApJS, 211, 25
Chen, C. H., Patten, B. M., Werner, M. W., et al. 2005, ApJ, 634, 1372
Cheng, K.-P. & Neff, J. E. 2003, AJ, 125, 868
Cheng, K.-P., Neff, J. E., Johnson, D. M., et al. 2017, AJ, 153, 39
Cotten, T. H. & Song, I. 2016, ApJS, 225, 15
Currie, T., Guyon, O., Tamura, M., et al. 2017, ApJ, 836, L15
Currie, T., Lisse, C. M., Sicilia-Aguilar, A., Rieke, G. H., & Su, K. Y. L. 2011, ApJ, 734, 115
David, T. J. & Hillenbrand, L. A. 2015, ApJ, 804, 146
de Zeeuw, P. T., Hoogerwerf, R., de Bruijne, J. H. J., Brown, A. G. A., & Blaauw, A. 1999, AJ, 117, 354
Desidera, S., Covino, E., Messina, S., et al. 2015, A&A, 573, A126

Donaldson, J. K., Lebreton, J., Roberge, A., Augereau, J.-C., & Krivov, A. V. 2013, ApJ, 772, 17
Donaldson, J. K., Roberge, A., Chen, C. H., et al. 2012, ApJ, 753, 147
Draper, Z. H., Matthews, B. C., Kennedy, G. M., et al. 2016, MNRAS, 456, 459
Duchêne, G., Arriaga, P., Wyatt, M., et al. 2014, ApJ, 784, 148
Eggleton, P. P. & Tokovinin, A. A. 2008, MNRAS, 389, 869
Eiroa, C., Marshall, J. P., Mora, A., et al. 2013, A&A, 555, A11
Eiroa, C., Rebollido, I., Montesinos, B., et al. 2016, A&A, 594, L1
Ertel, S., Absil, O., Defrère, D., et al. 2014, A&A, 570, A128
Ertel, S., Defrère, D., Absil, O., et al. 2016, A&A, 595, A44
Faraggiana, R. & Bonifacio, P. 1999, A&A, 349, 521
Faramaz, V., Ertel, S., Booth, M., Cuadra, J., & Simmonds, C. 2017, MNRAS, 465, 2352
Ferlet, R., Vidal-Madjar, A., & Hobbs, L. M. 1987, A&A, 185, 267
Fernández, R., Brandeker, A., & Wu, Y. 2006, ApJ, 643, 509
Frandsen, S. & Lindberg, B. 2000, in The Third MONS Workshop: Science Preparation and Target Selection, ed. T. Teixeira & T. Bedding, 163
Gáspár, A., Rieke, G. H., & Balog, Z. 2013, ApJ, 768, 25
Geiler, F. & Krivov, A. V. 2017, MNRAS, 468, 959
Génova, R. & Beckman, J. E. 2003, ApJS, 145, 355
Gontcharov, G. A. 2012, Astronomy Letters, 38, 771
Grady, C. A., Brown, A., Welsh, B., et al. 2018, AJ, 155, 242
Grady, C. A., McCollum, B., Rawley, L. A., et al. 1996a, ApJ, 464, L183
Grady, C. A., Perez, M. R., Talavera, A., et al. 1996b, ApJ, 471, L49
Gray, R. O. & Corbally, J., C. 2009, Stellar Spectral Classification
Gray, R. O., Riggs, Q. S., Koen, C., et al. 2017, AJ, 154, 31
Greaves, J. S., Holland, W. S., Matthews, B. C., et al. 2016, MNRAS, 461, 3910
Gudennavar, S. B., Bubbly, S. G., Preethi, K., & Murthy, J. 2012, ApJS, 199, 8
Hauck, B. & Jaschek, C. 2000, A&A, 354, 157
Hempel, M. & Schmitt, J. H. M. M. 2003, A&A, 408, 971
Hobbs, L. M., Welty, D. E., Lagrange-Henri, A. M., Ferlet, R., & Vidal-Madjar, A. 1988, ApJ, 334, L41
Holweger, H., Hempel, M., & Kamp, I. 1999, A&A, 350, 603
Holweger, H. & Rentzsch-Holm, I. 1995, A&A, 303, 819
Howe, K. S. & Clarke, C. J. 2009, MNRAS, 392, 448
Iglesias, D., Bayo, A., Olofsson, J., et al. 2018, MNRAS, 480, 488
Iglesias, D. P., Olofsson, J., Bayo, A., et al. 2019, MNRAS, 490, 5218
Jaschek, M., Jaschek, C., & Andrillat, Y. 1988, A&AS, 72, 505
Jura, M. 2015, AJ, 150, 166
Kalas, P. 2005, ApJ, 635, L169
Kasper, M., Apai, D., Wagner, K., & Robberto, M. 2015, ApJ, 812, L33
Kaufer, A., Stahl, O., Tubbesing, S., et al. 1999, The Messenger, 95, 8
Kausch, W., Noll, S., Smette, A., et al. 2015, A&A, 576, A78
Kennedy, G. M. & Wyatt, M. C. 2014, MNRAS, 444, 3164
Kiefer, F., Lecavelier des Etangs, A., Augereau, J.-C., et al. 2014a, A&A, 561, L10
Kiefer, F., Lecavelier des Etangs, A., Boissier, J., et al. 2014b, Nature, 514, 462
Kirchschlager, F., Wolf, S., Krivov, A. V., Mutschke, H., & Brunngräber, R. 2017, MNRAS, 467, 1614
Koen, C. 2003, MNRAS, 341, 1385
Kóspál, Á., Moór, A., Juhász, A., et al. 2013, ApJ, 776, 77
Kral, Q., Marino, S., Wyatt, M. C., Kama, M., & Matrà, L. 2019, MNRAS, 489, 3670
Kral, Q., Matrà, L., Wyatt, M. C., & Kennedy, G. M. 2017, MNRAS, 469, 521
Lagrange, A.-M., Beust, H., Mouillet, D., et al. 1998, A&A, 330, 1091
Lagrange, A.-M., Bonnefoy, M., Chauvin, G., et al. 2010, Science, 329, 57
Lagrange, A. M., Desort, M., Galland, F., Udry, S., & Mayor, M. 2009, A&A, 495, 335
Lagrange-Henri, A. M., Beust, H., Ferlet, R., Vidal-Madjar, A., & Hobbs, L. M. 1990a, A&A, 227, L13
Lagrange-Henri, A. M., Ferlet, R., Vidal-Madjar, A., & Beust, H. 1991, A&A, 246, 507
Lagrange-Henri, A. M., Ferlet, R., Vidal-Madjar, A., et al. 1990b, A&AS, 85, 1089
Lagrange-Henri, A. M., Ferlet, R., Vidal-Madjar, A., et al. 1990c, A&AS, 85, 1089
Lecavelier Des Etangs, A., Deleuil, M., Vidal-Madjar, A., et al. 1997, A&A, 325, 228
Lieman-Sifry, J., Hughes, A. M., Carpenter, J. M., et al. 2016, ApJ, 828, 25
Lisse, C. M., Sitko, M. L., Russell, R. W., et al. 2017, ApJ, 840, L20
Maldonado, J., Eiroa, C., Villaver, E., Montesinos, B., & Mora, A. 2012, A&A, 541, A40
Maldonado, J. & Villaver, E. 2017, A&A, 602, A38
Maldonado, J., Villaver, E., & Eiroa, C. 2018, A&A, 612, A93
Mamajek, E. E. & Bell, C. P. M. 2014, MNRAS, 445, 2169
Marboeuf, U., Bonsor, A., & Augereau, J.-C. 2016, Planet. Space Sci., 133, 47
Marino, S., Bonsor, A., Wyatt, M. C., & Kral, Q. 2018, MNRAS, 479, 1651
Marino, S., Matrà, L., Stark, C., et al. 2016, MNRAS, 460, 2933
Marino, S., Wyatt, M. C., Panić, O., et al. 2017, MNRAS, 465, 2595
Matrà, L., Dent, W. R. F., Wyatt, M. C., et al. 2017, MNRAS, 464, 1415
Matthews, B. C., Krivov, A. V., Wyatt, M. C., Bryden, G., & Eiroa, C. 2014, Protostars and Planets VI, 521
Mayor, M. & Queloz, D. 1995, Nature, 378, 355
Mékarnia, D., Chapellier, E., Guillot, T., et al. 2017, A&A, 608, L6
Mellon, S. N., Mamajek, E. E., Zwintz, K., et al. 2019, ApJ, 870, 36
Montesinos, B., Eiroa, C., Lillo-Box, J., et al. 2019, A&A, 629, A19
Montgomery, S. L. & Welsh, B. Y. 2012, PASP, 124, 1042
Montgomery, S. L. & Welsh, B. Y. 2017, MNRAS, 468, L55
Moór, A., Ábrahám, P., Juhász, A., et al. 2011a, ApJ, 740, L7
Moór, A., Curé, M., Kóspál, Á., et al. 2017, ApJ, 849, 123
Moór, A., Henning, T., Juhász, A., et al. 2015a, ApJ, 814, 42
Moór, A., Kóspál, Á., Ábrahám, P., et al. 2015b, MNRAS, 447, 577
Moór, A., Pascucci, I., Kóspál, Á., et al. 2011b, ApJS, 193, 4
Mora, A., Merín, B., Solano, E., et al. 2001, A&A, 378, 116
Morales, F. Y., Bryden, G., Werner, M. W., & Stapelfeldt, K. R. 2016, ApJ, 831, 97
Murphy, S. J., Corbally, C. J., Gray, R. O., et al. 2015a, PASA, 32, e036
Murphy, S. J., Corbally, C. J., Gray, R. O., et al. 2015b, PASA, 32, e036
Murphy, S. J. & Paunzen, E. 2017, MNRAS, 466, 546
Nesvorný, D., Jenniskens, P., Levison, H. F., et al. 2010, ApJ, 713, 816
Nielsen, M. B., Gizon, L., Schunker, H., & Karoff, C. 2013, A&A, 557, L10
Nuñez, P. D., Scott, N. J., Mennesson, B., et al. 2017, A&A, 608, A113
Paunzen, E. 2004, in IAU Symposium, Vol. 224, The A-Star Puzzle, ed. J. Zverko, J. Ziznovsky, S. J. Adelman, & W. W. Weiss, 443–450
Pawellek, N., Krivov, A. V., Marshall, J. P., et al. 2014, ApJ, 792, 65
Pecaut, M. J. & Mamajek, E. E. 2013, ApJS, 208, 9
Pecaut, M. J. & Mamajek, E. E. 2016, MNRAS, 461, 794
Pecaut, M. J., Mamajek, E. E., & Bubar, E. J. 2012, ApJ, 746, 154
Plavchan, P., Werner, M. W., Chen, C. H., et al. 2009, ApJ, 698, 1068
Quirrenbach, A., Amado, P. J., Caballero, J. A., et al. 2016, in Proc. SPIE, Vol. 9908, Ground-based and Airborne Instrumentation for Astronomy VI, 990812
Rappaport, S., Vanderburg, A., Jacobs, T., et al. 2018, MNRAS, 474, 1453
Raskin, G., van Winckel, H., Hensberge, H., et al. 2011, A&A, 526, A69
Rebollido, I., Eiroa, C., Montesinos, B., et al. 2018, A&A, 614, A3
Rebollido, I., Eiroa, C., Montesinos, B., et al. 2019, A&A, 625, C2
Redfield, S. 2007, ApJ, 656, L97
Redfield, S., Kessler-Silacci, J. E., & Cieza, L. A. 2007, ApJ, 661, 944
Redfield, S. & Linsky, J. L. 2008a, ApJ, 673, 283
Redfield, S. & Linsky, J. L. 2008b, ApJ, 673, 283
Riviere-Marichalar, P., Barrado, D., Augereau, J.-C., et al. 2012, A&A, 546, L8
Riviere-Marichalar, P., Barrado, D., Montesinos, B., et al. 2014, A&A, 565, A68
Riviere-Marichalar, P., Pinte, C., Barrado, D., et al. 2013, A&A, 555, A67
Roberge, A., Feldman, P. D., Weinberger, A. J., Deleuil, M., & Bouret, J.-C. 2006, Nature, 441, 724
Roberge, A., Kamp, I., Montesinos, B., et al. 2013, ApJ, 771, 69
Roberge, A. & Weinberger, A. J. 2008, ApJ, 676, 509
Roberge, A., Welsh, B. Y., Kamp, I., Weinberger, A. J., & Grady, C. A. 2014, ApJ, 796, L11
Rodriguez, E., Lopez de Coca, P., Rolland, A., Garrido, R., & Costa, V. 1994, A&AS, 106, 21
Schmitt, J. H. M. M., Schröder, K.-P., Rauw, G., et al. 2014, Astronomische Nachrichten, 335, 787
Schüppler, C., Krivov, A. V., Löhne, T., et al. 2016, MNRAS, 461, 2146
Sezestre, É., Augereau, J. C., & Thébault, P. 2019, A&A, 626, A2
Sibthorpe, B., Kennedy, G. M., Wyatt, M. C., et al. 2018, MNRAS, 475, 3046
Smette, A., Sana, H., Noll, S., et al. 2015, A&A, 576, A77
Somerville, W. B. 1988, The Observatory, 108, 44
Su, K. Y. L., Rieke, G. H., Stansberry, J. A., et al. 2006, ApJ, 653, 675
Thébault, P. & Beust, H. 2001, A&A, 376, 621
Thureau, N. D., Greaves, J. S., Matthews, B. C., et al. 2014, MNRAS, 445, 2558
Tokovinin, A. 2008, MNRAS, 389, 925
Torres, C. A. O., Quast, G. R., Melo, C. H. F., & Sterzik, M. F. 2008, Young Nearby Loose Associations, ed. B. Reipurth, 757
Vican, L., Schneider, A., Bryden, G., et al. 2016, ApJ, 833, 263
Vidal-Madjar, A., Kiefer, F., Lecavelier des Etangs, A., et al. 2017, A&A, 607, A25
Vidal-Madjar, A., Lagrange-Henri, A.-M., Feldman, P. D., et al. 1994, A&A, 290, 245
Welsh, B. Y., Craig, N., Crawford, I. A., & Price, R. J. 1998, A&A, 338, 674
Welsh, B. Y., Lallement, R., Vergely, J.-L., & Raimond, S. 2010, A&A, 510, A54
Welsh, B. Y. & Montgomery, S. 2013, PASP, 125, 759
Welsh, B. Y. & Montgomery, S. L. 2015, Advances in Astronomy, 2015, 980323
Welsh, B. Y. & Montgomery, S. L. 2018, MNRAS, 474, 1515
Welsh, B. Y. & Montgomery, S. L. 2019, Research Notes of the American Astronomical Society, 3, 25
Welty, D. E., Hobbs, L. M., & Kulkarni, V. P. 1994, ApJ, 436, 152
Welty, D. E., Morton, D. C., & Hobbs, L. M. 1996, ApJS, 106, 533
Wenger, M., Ochsenbein, F., Egret, D., et al. 2000, A&AS, 143, 9
Wood, H. J. & Hollis, J. M. 1971, A&A, 12, 468
Zieba, S., Zwintz, K., Kenworthy, M. A., & Kennedy, G. M. 2019, A&A, 625, L13
Zuckerman, B. 2019, ApJ, 870, 27
Zuckerman, B. & Song, I. 2012, ApJ, 758, 77

Appendix A: Figures

Appendix A.1: Narrow Stable Absorptions

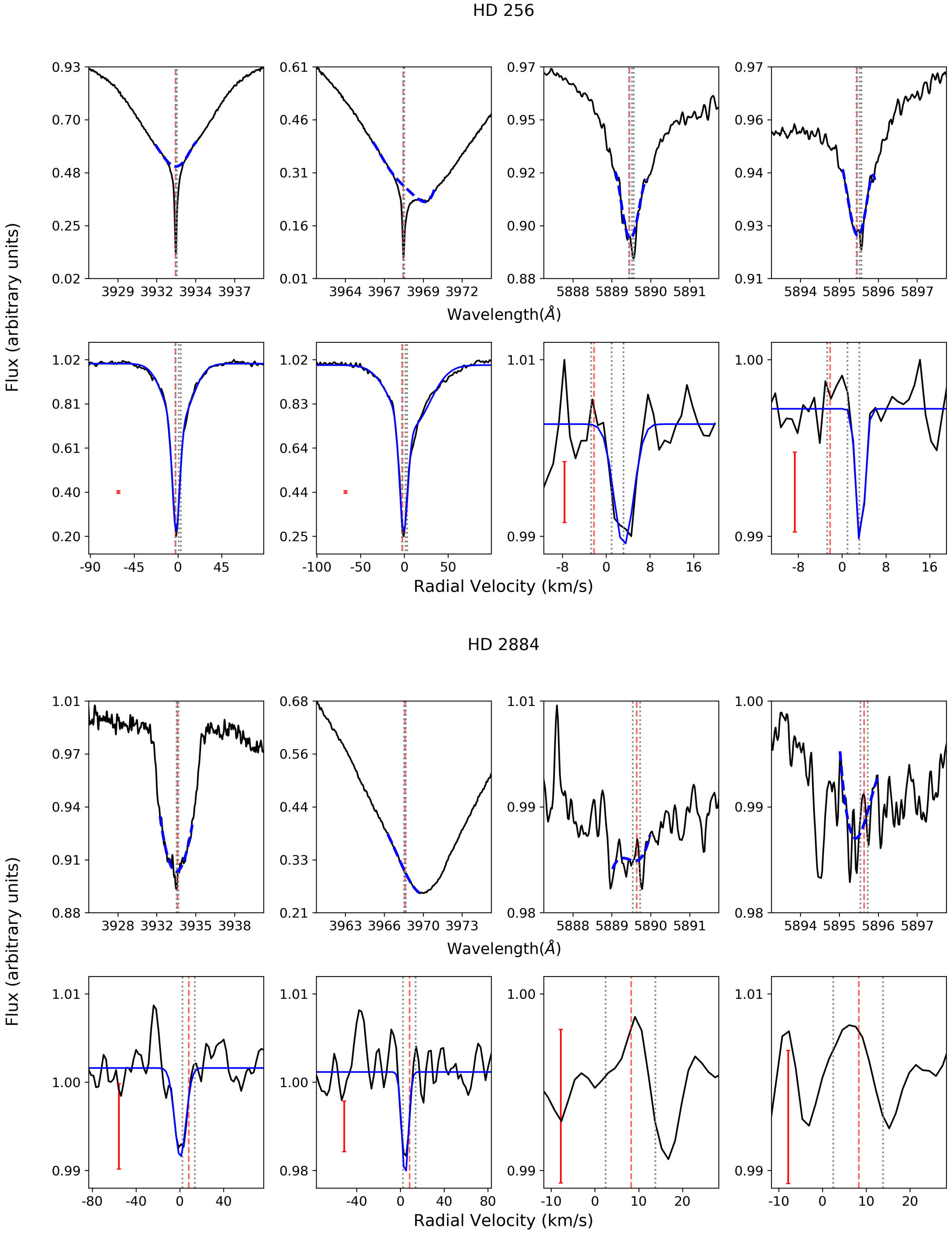

Fig. A.1: Stars showing narrow non-photospheric absorptions. Top panels: Photospheric Ca ɪɪ H & K and Na ɪ D lines with fitted modeling dashed blue line, x-axis shows the wavelength. Bottom panels: Residuals once the spectrum is divided by the photosphere, x-axis in velocity. Blue lines mark the fits to the non-photospheric absorptions. Vertical red dashed and grey dotted lines represent the stellar radial velocity and the ISM velocities respectively. Red error bars show three sigma value measured in the continuum adjacent to the photospheric line.

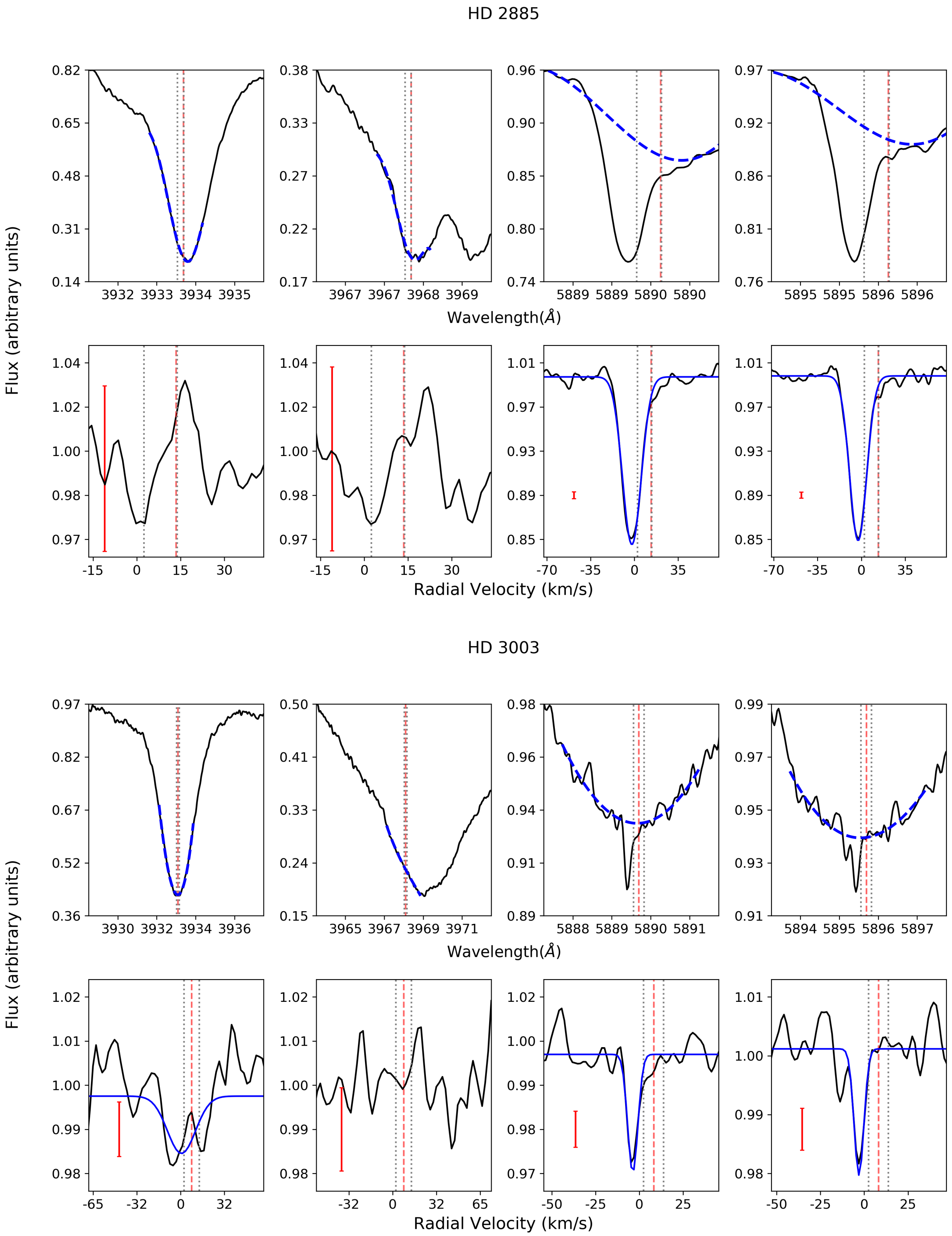

Fig. A.1: Stars showing narrow non-photospheric absorptions. Top panels: Photospheric Ca II H & K and Na I D lines with fitted modeling dashed blue line, x-axis shows the wavelength. Bottom panels: Residuals once the spectrum is divided by the photosphere, x-axis in velocity. Blue lines mark the fits to the non-photospheric absorptions. Vertical red dashed and grey dotted lines represent the stellar radial velocity and the ISM velocities respectively. Red error bars show three sigma value measured in the continuum adjacent to the photospheric line.

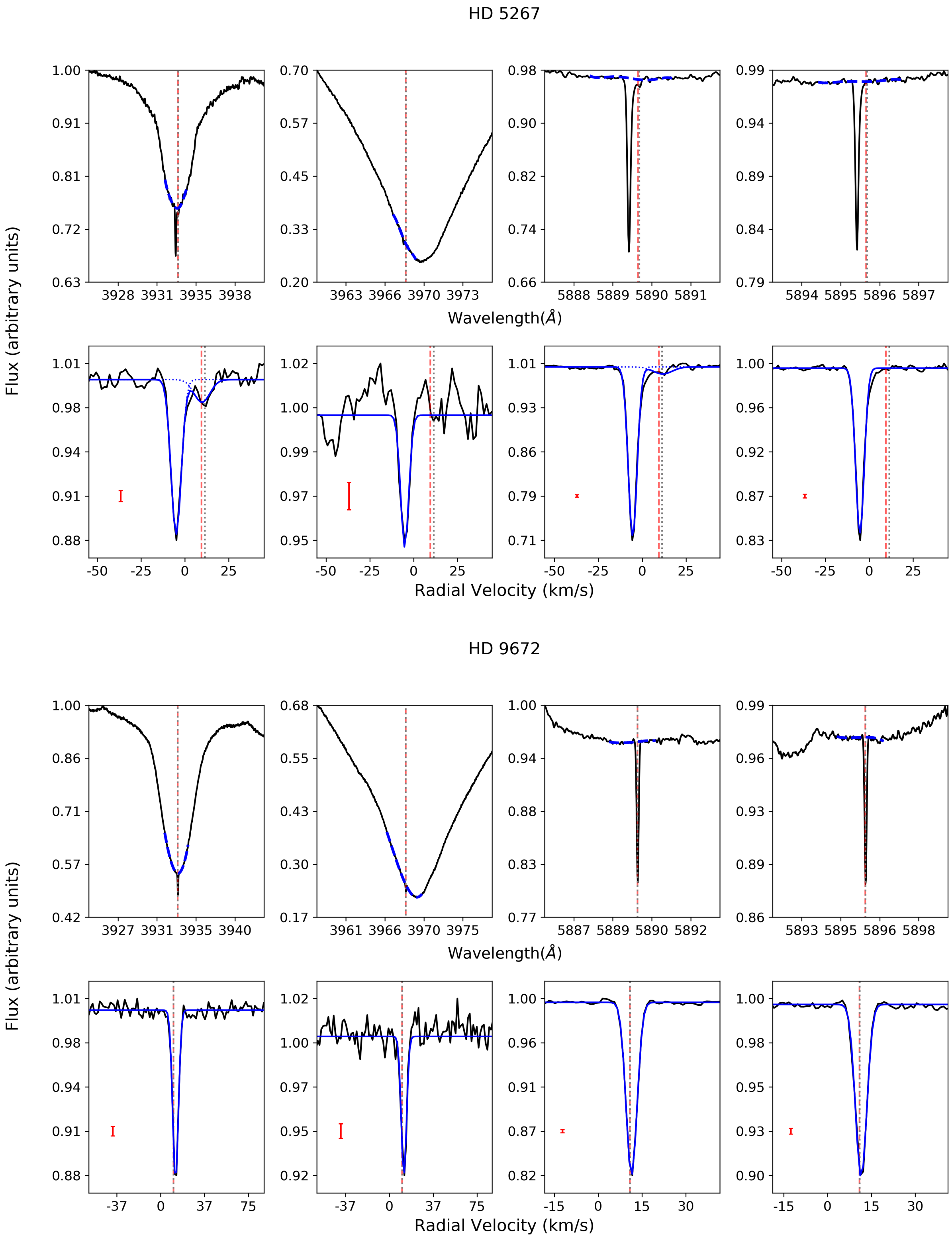

Fig. 1 (Cont.): Stars showing narrow non-photospheric absorptions. Top panels: Photospheric Ca ii H & K and Na i D lines with fitted modeling dashed blue line, x-axis shows the wavelength. Bottom panels: Residuals once the spectrum is divided by the photosphere, x-axis in velocity. Blue lines mark the fits to the non-photospheric absorptions. Vertical red dashed and grey dotted lines represent the stellar radial velocity and the ISM velocities respectively. Red error bars show three sigma value measured in the continuum adjacent to the photospheric line.

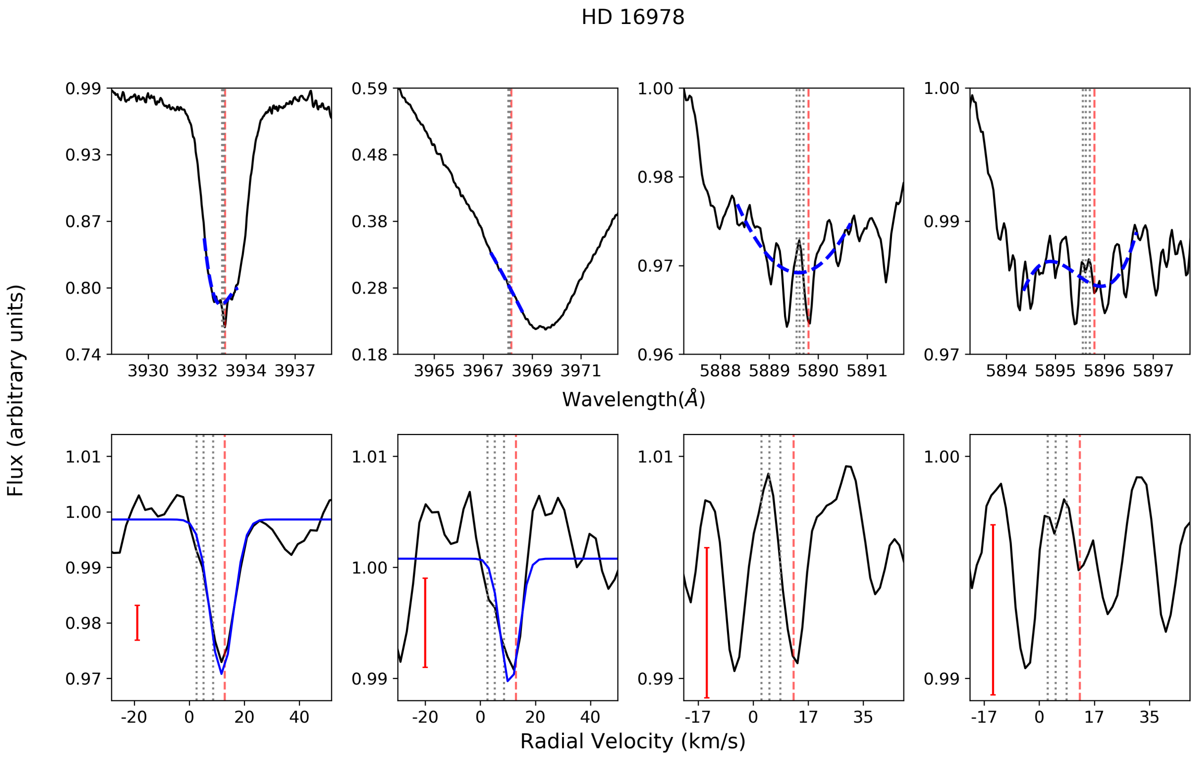

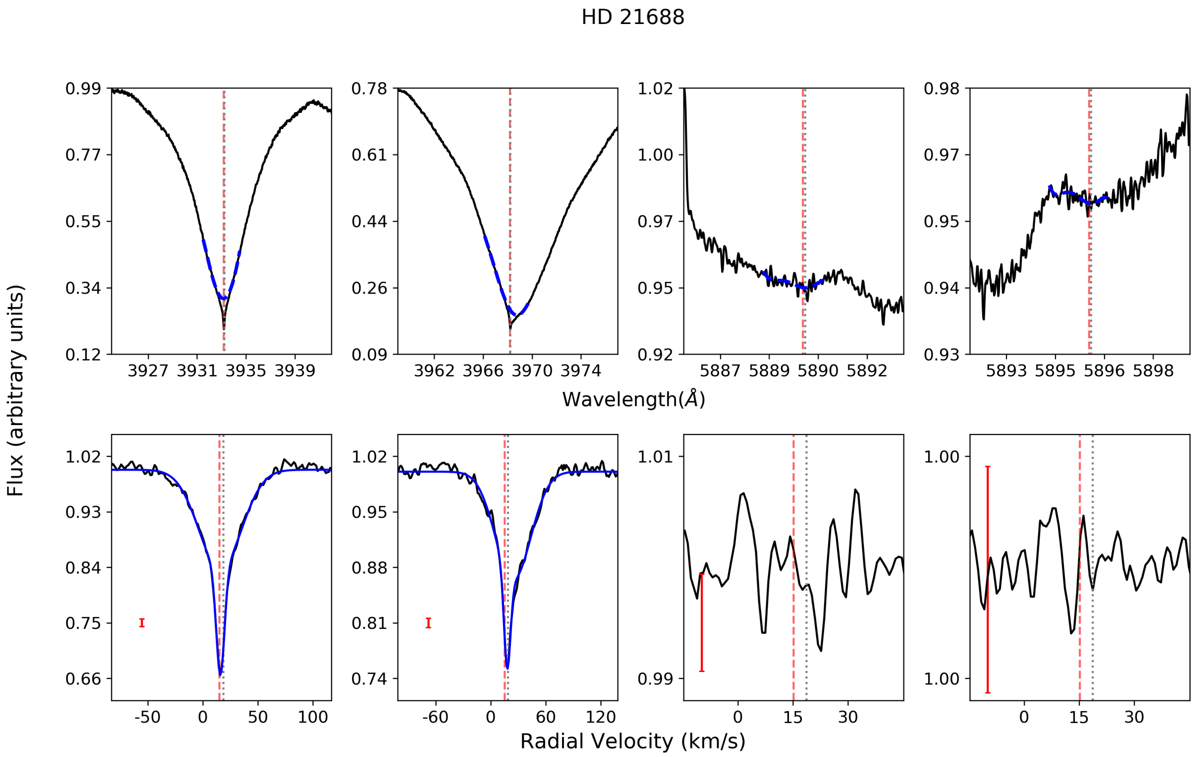

Fig. 1 (Cont.): Stars showing narrow non-photospheric absorptions. Top panels: Photospheric Ca II H & K and Na I D lines with fitted modeling dashed blue line, x-axis shows the wavelength. Bottom panels: Residuals once the spectrum is divided by the photosphere, x-axis in velocity. Blue lines mark the fits to the non-photospheric absorptions. Vertical red dashed and grey dotted lines represent the stellar radial velocity and the ISM velocities respectively. Red error bars show three sigma value measured in the continuum adjacent to the photospheric line.

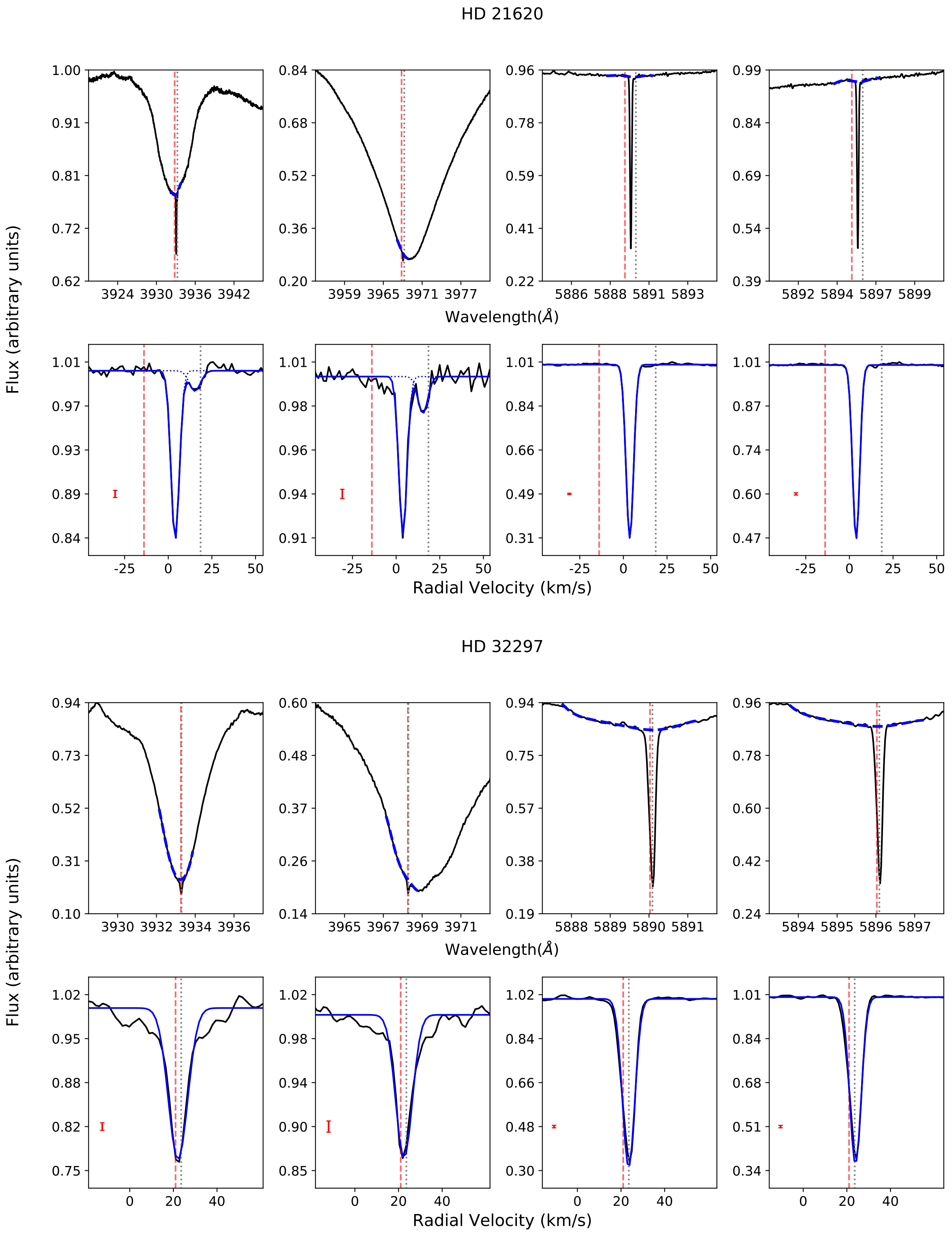

Fig. 1 (Cont.): Stars showing narrow non-photospheric absorptions. Top panels: Photospheric Ca II H & K and Na I D lines with fitted modeling dashed blue line, x-axis shows the wavelength. Bottom panels: Residuals once the spectrum is divided by the photosphere, x-axis in velocity. Blue lines mark the fits to the non-photospheric absorptions. Vertical red dashed and grey dotted lines represent the stellar radial velocity and the ISM velocities respectively. Red error bars show three sigma value measured in the continuum adjacent to the photospheric line.

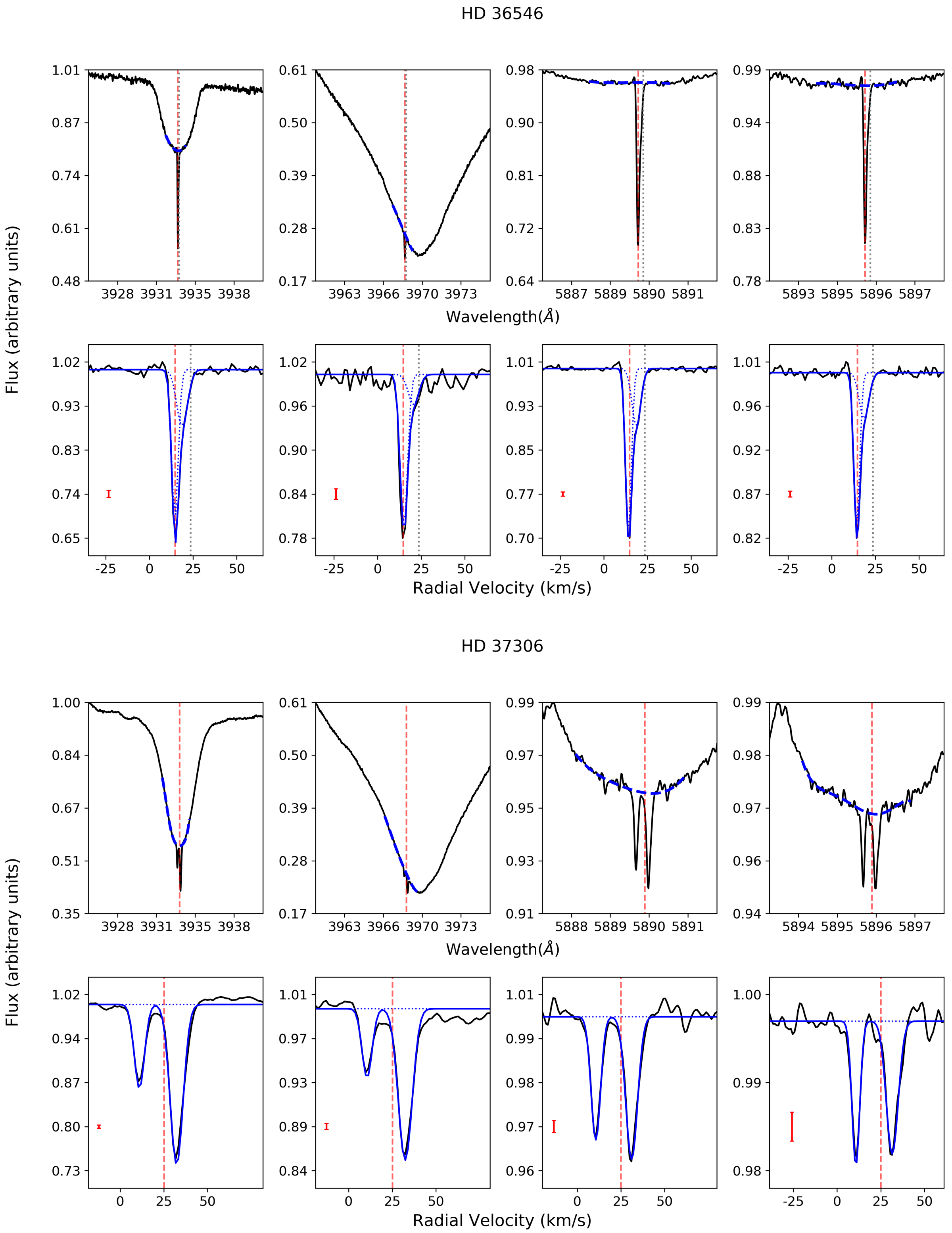

Fig. 1 (Cont.): Stars showing narrow non-photospheric absorptions. Top panels: Photospheric Ca II H & K and Na I D lines with fitted modeling dashed blue line, x-axis shows the wavelength. Bottom panels: Residuals once the spectrum is divided by the photosphere, x-axis in velocity. Blue lines mark the fits to the non-photospheric absorptions. Vertical red dashed and grey dotted lines represent the stellar radial velocity and the ISM velocities respectively. Red error bars show three sigma value measured in the continuum adjacent to the photospheric line.

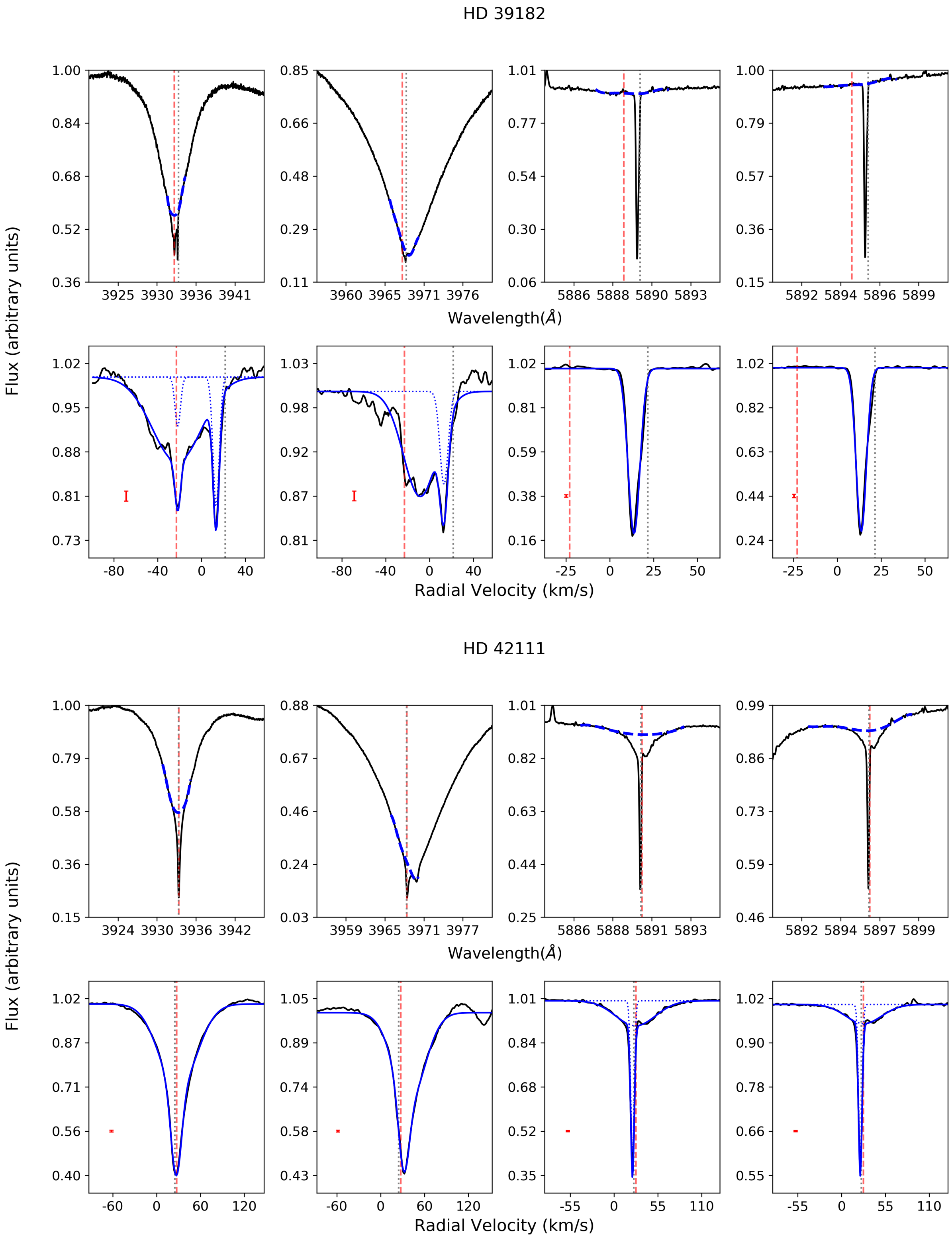

Fig. 1 (Cont.): Stars showing narrow non-photospheric absorptions. Top panels: Photospheric Ca ii H & K and Na i D lines with fitted modeling dashed blue line, x-axis shows the wavelength. Bottom panels: Residuals once the spectrum is divided by the photosphere, x-axis in velocity. Blue lines mark the fits to the non-photospheric absorptions. Vertical red dashed and grey dotted lines represent the stellar radial velocity and the ISM velocities respectively. Red error bars show three sigma value measured in the continuum adjacent to the photospheric line.

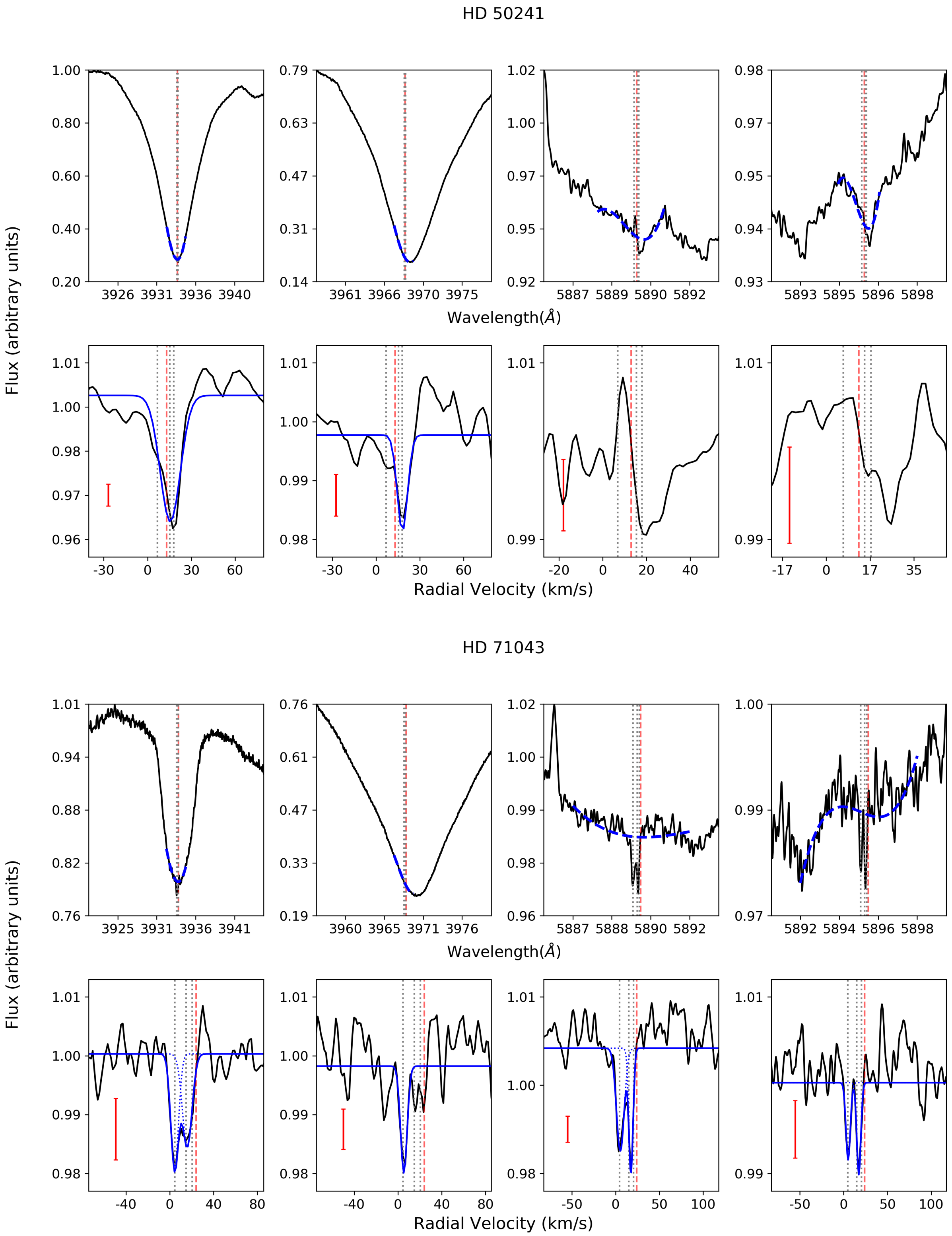

Fig. 1 (Cont.): Stars showing narrow non-photospheric absorptions. Top panels: Photospheric Ca II H & K and Na I D lines with fitted modeling dashed blue line, x-axis shows the wavelength. Bottom panels: Residuals once the spectrum is divided by the photosphere, x-axis in velocity. Blue lines mark the fits to the non-photospheric absorptions. Vertical red dashed and grey dotted lines represent the stellar radial velocity and the ISM velocities respectively. Red error bars show three sigma value measured in the continuum adjacent to the photospheric line.

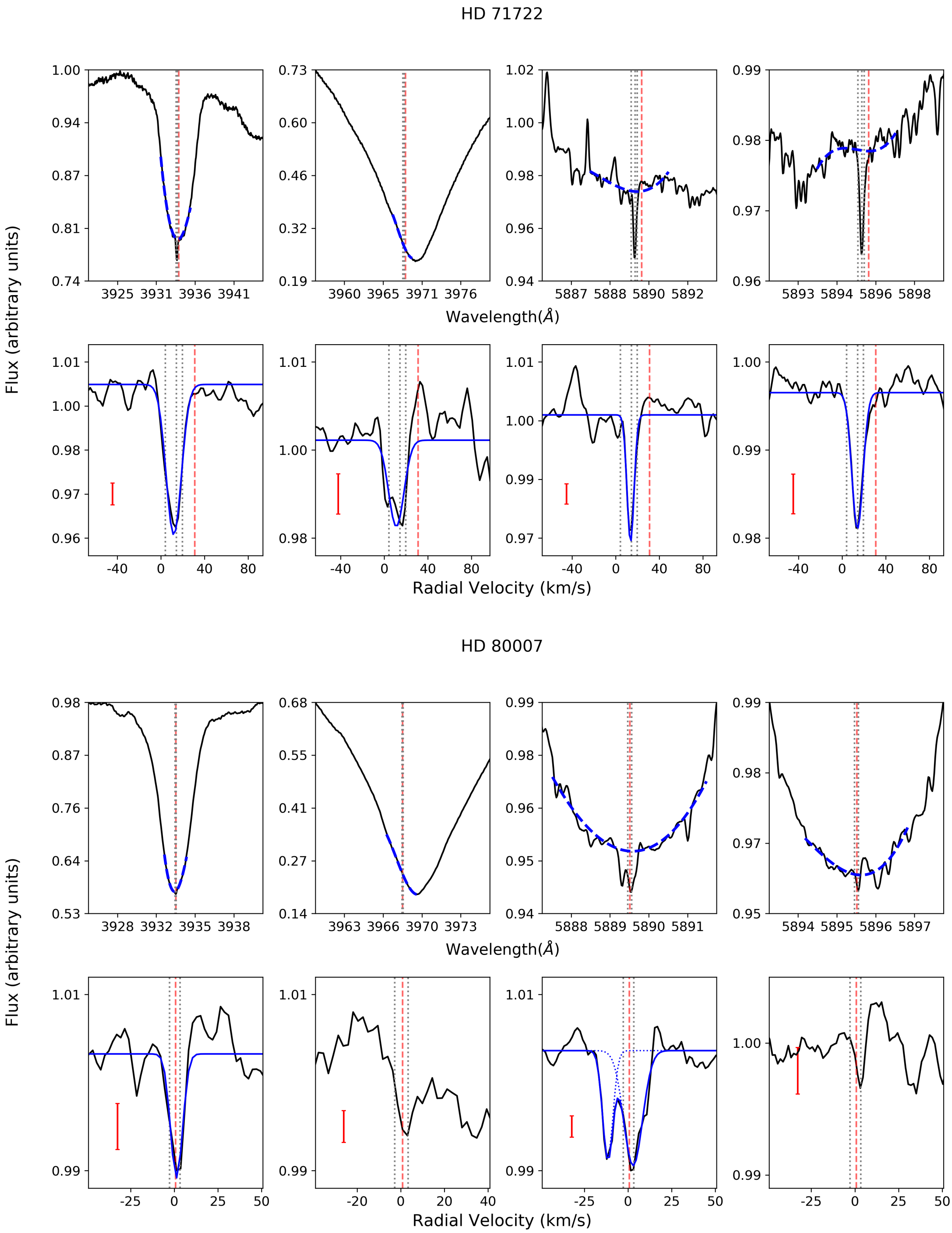

Fig. 1 (Cont.): Stars showing narrow non-photospheric absorptions. Top panels: Photospheric Ca II H & K and Na I D lines with fitted modeling dashed blue line, x-axis shows the wavelength. Bottom panels: Residuals once the spectrum is divided by the photosphere, x-axis in velocity. Blue lines mark the fits to the non-photospheric absorptions. Vertical red dashed and grey dotted lines represent the stellar radial velocity and the ISM velocities respectively. Red error bars show three sigma value measured in the continuum adjacent to the photospheric line.

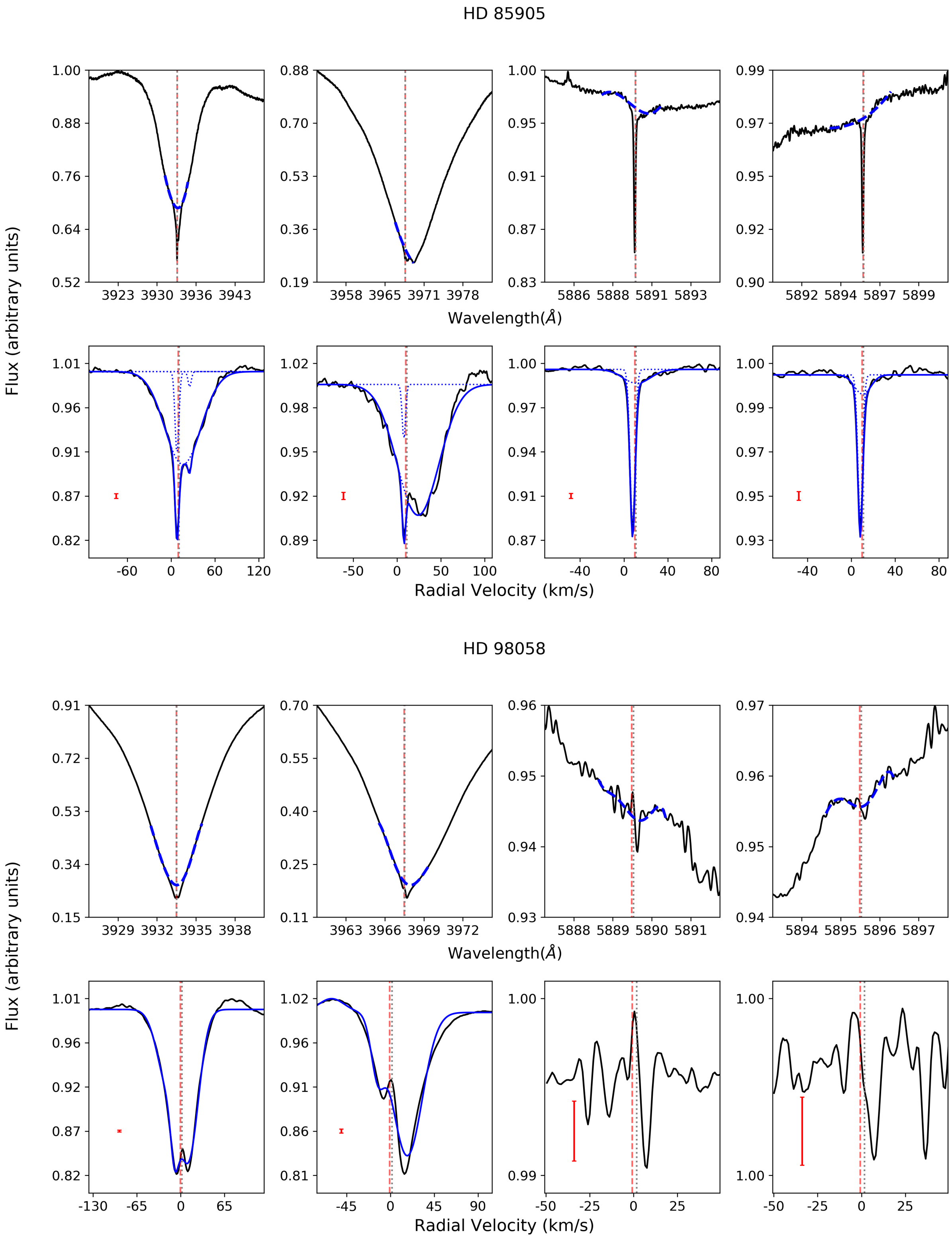

Fig. 1 (Cont.): Stars showing narrow non-photospheric absorptions. Top panels: Photospheric Ca II H & K and Na I D lines with fitted modeling dashed blue line, x-axis shows the wavelength. Bottom panels: Residuals once the spectrum is divided by the photosphere, x-axis in velocity. Blue lines mark the fits to the non-photospheric absorptions. Vertical red dashed and grey dotted lines represent the stellar radial velocity and the ISM velocities respectively. Red error bars show three sigma value measured in the continuum adjacent to the photospheric line.

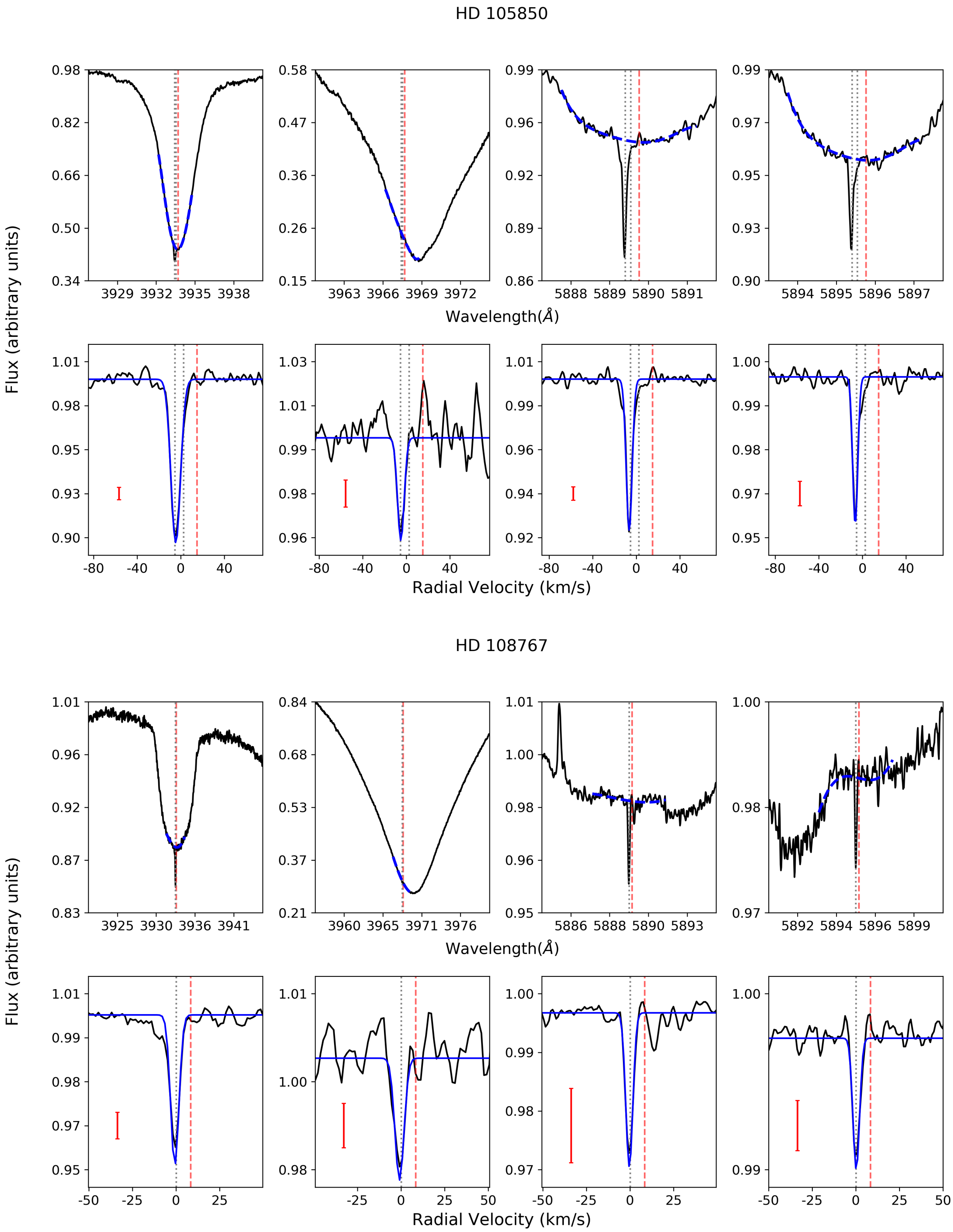

Fig. 1 (Cont.): Stars showing narrow non-photospheric absorptions. Top panels: Photospheric Ca II H & K and Na I D lines with fitted modeling dashed blue line, x-axis shows the wavelength. Bottom panels: Residuals once the spectrum is divided by the photosphere, x-axis in velocity. Blue lines mark the fits to the non-photospheric absorptions. Vertical red dashed and grey dotted lines represent the stellar radial velocity and the ISM velocities respectively. Red error bars show three sigma value measured in the continuum adjacent to the photospheric line.

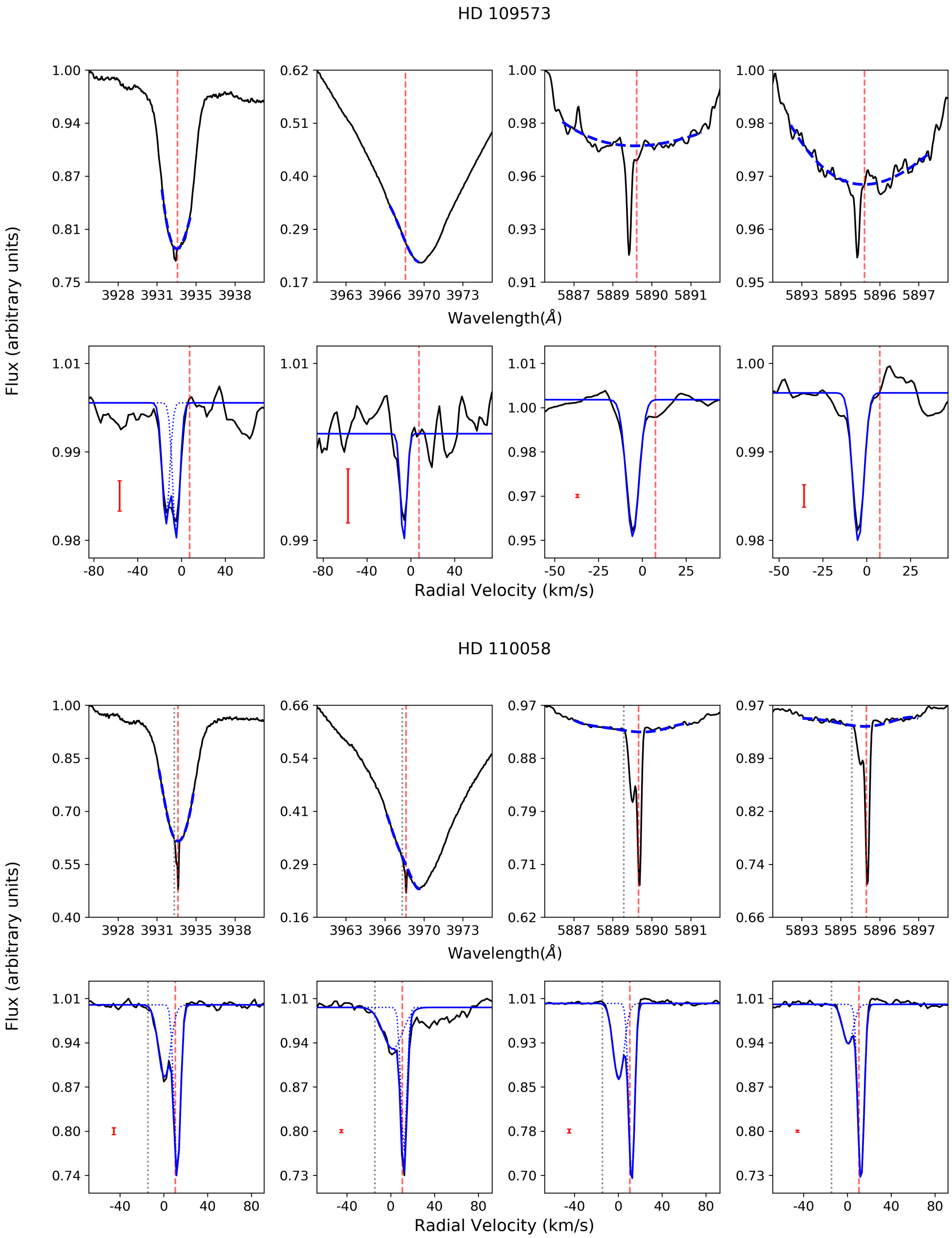

Fig. 1 (Cont.): Stars showing narrow non-photospheric absorptions. Top panels: Photospheric Ca ii H & K and Na i D lines with fitted modeling dashed blue line, x-axis shows the wavelength. Bottom panels: Residuals once the spectrum is divided by the photosphere, x-axis in velocity. Blue lines mark the fits to the non-photospheric absorptions. Vertical red dashed and grey dotted lines represent the stellar radial velocity and the ISM velocities respectively. Red error bars show three sigma value measured in the continuum adjacent to the photospheric line.

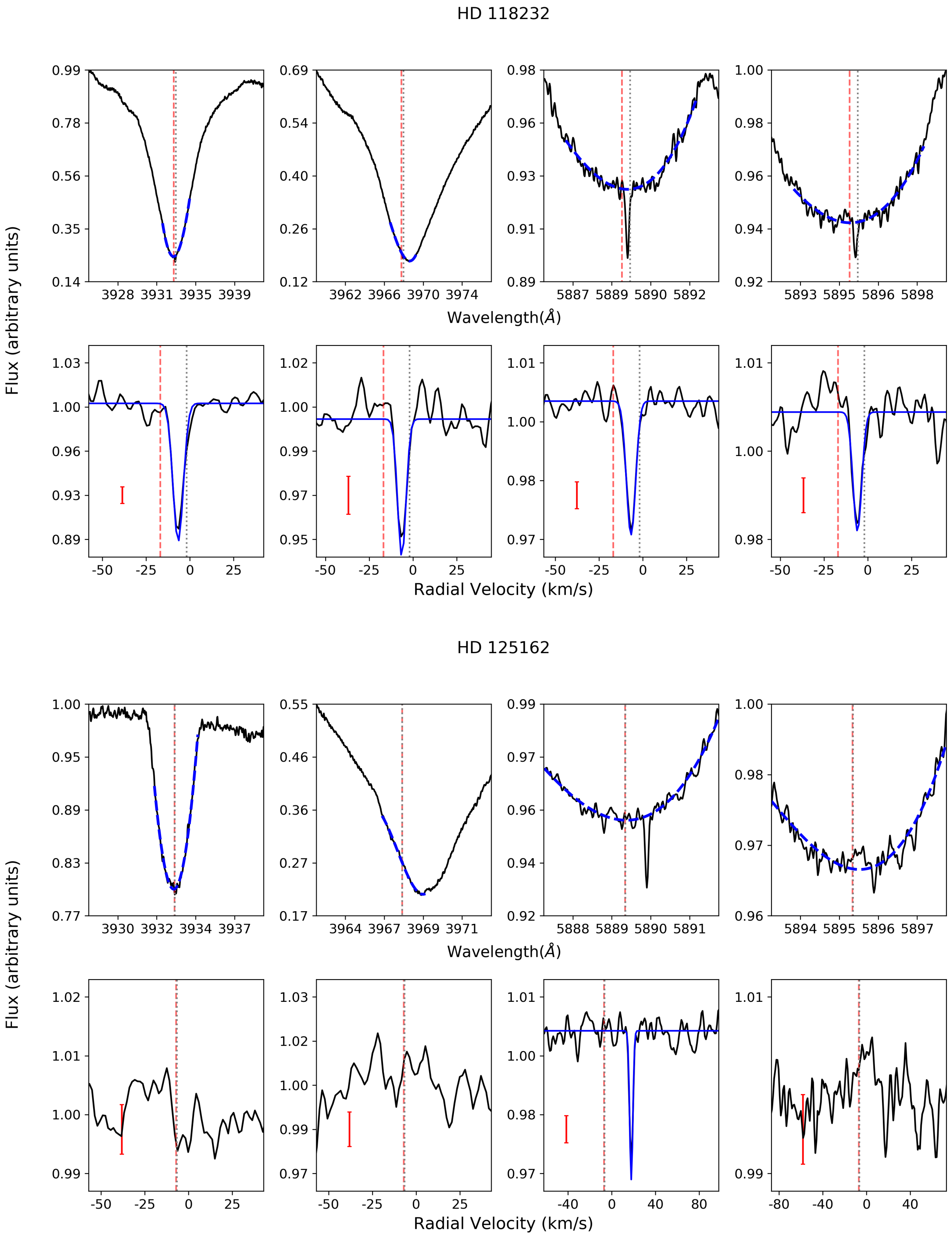

Fig. 1 (Cont.): Stars showing narrow non-photospheric absorptions. Top panels: Photospheric Ca II H & K and Na I D lines with fitted modeling dashed blue line, x-axis shows the wavelength. Bottom panels: Residuals once the spectrum is divided by the photosphere, x-axis in velocity. Blue lines mark the fits to the non-photospheric absorptions. Vertical red dashed and grey dotted lines represent the stellar radial velocity and the ISM velocities respectively. Red error bars show three sigma value measured in the continuum adjacent to the photospheric line.

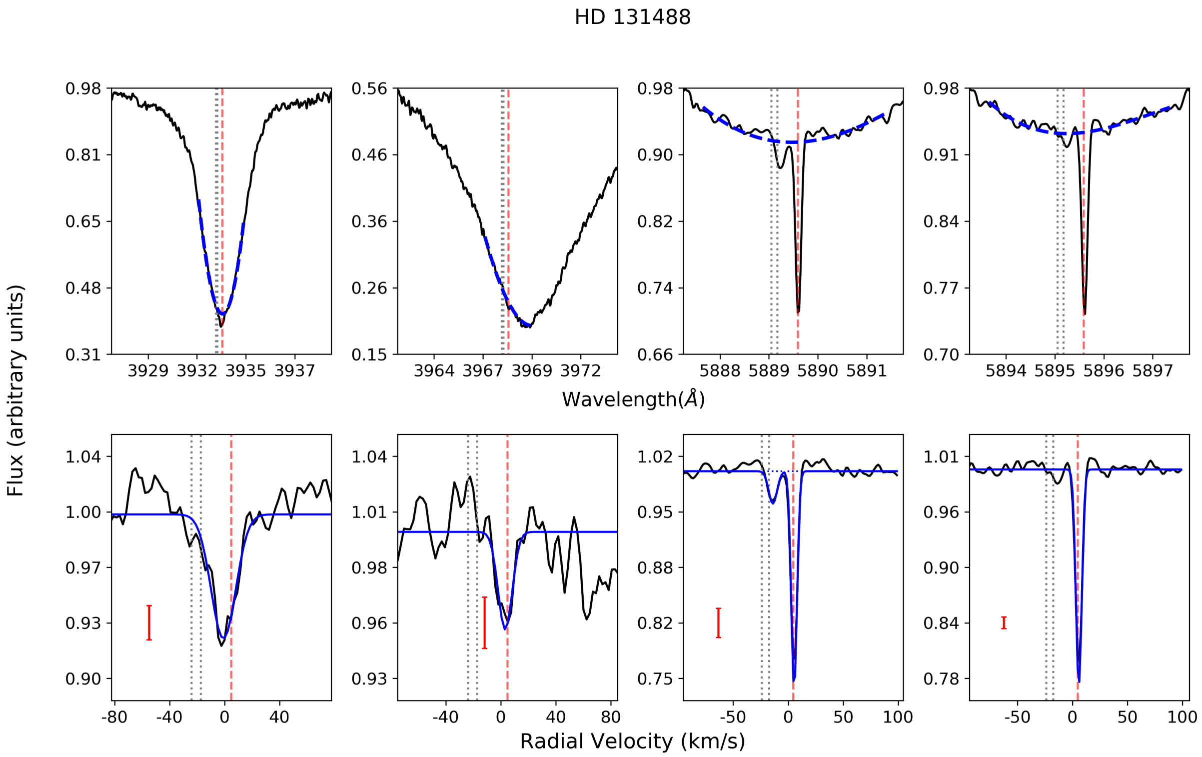

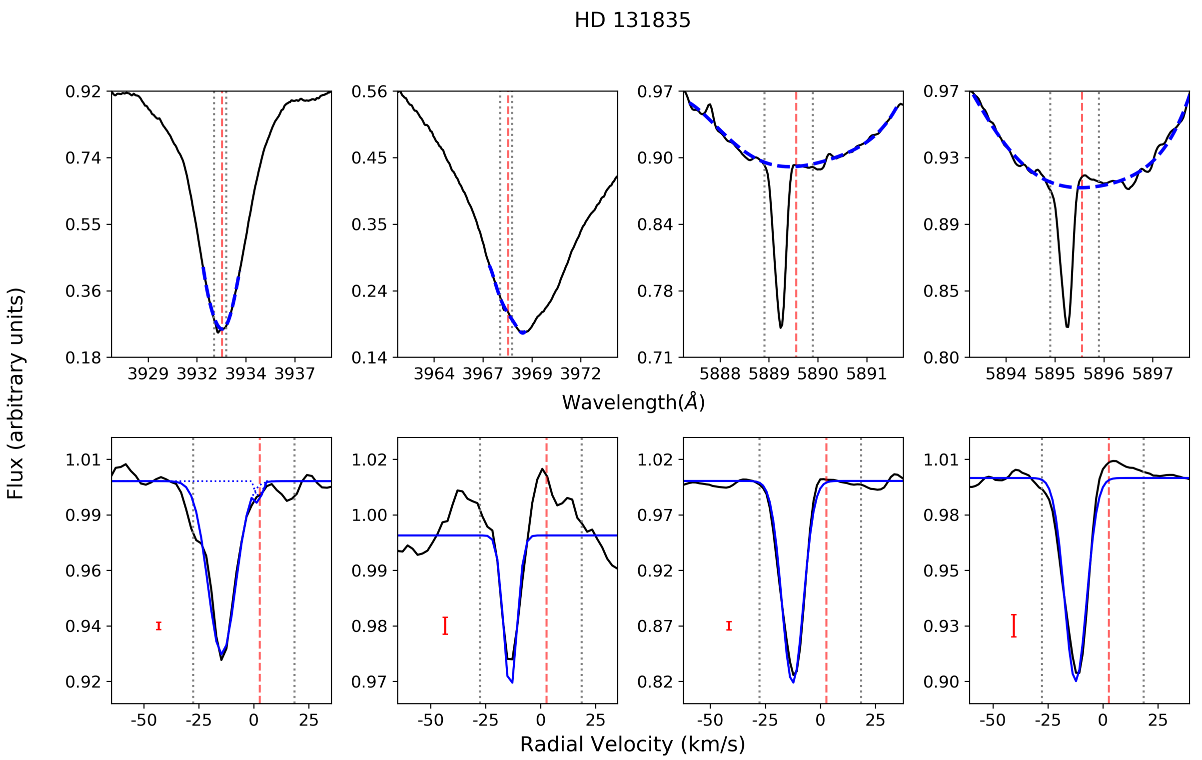

Fig. 1 (Cont.): Stars showing narrow non-photospheric absorptions. Top panels: Photospheric Ca II H & K and Na I D lines with fitted modeling dashed blue line, x-axis shows the wavelength. Bottom panels: Residuals once the spectrum is divided by the photosphere, x-axis in velocity. Blue lines mark the fits to the non-photospheric absorptions. Vertical red dashed and grey dotted lines represent the stellar radial velocity and the ISM velocities respectively. Red error bars show three sigma value measured in the continuum adjacent to the photospheric line.

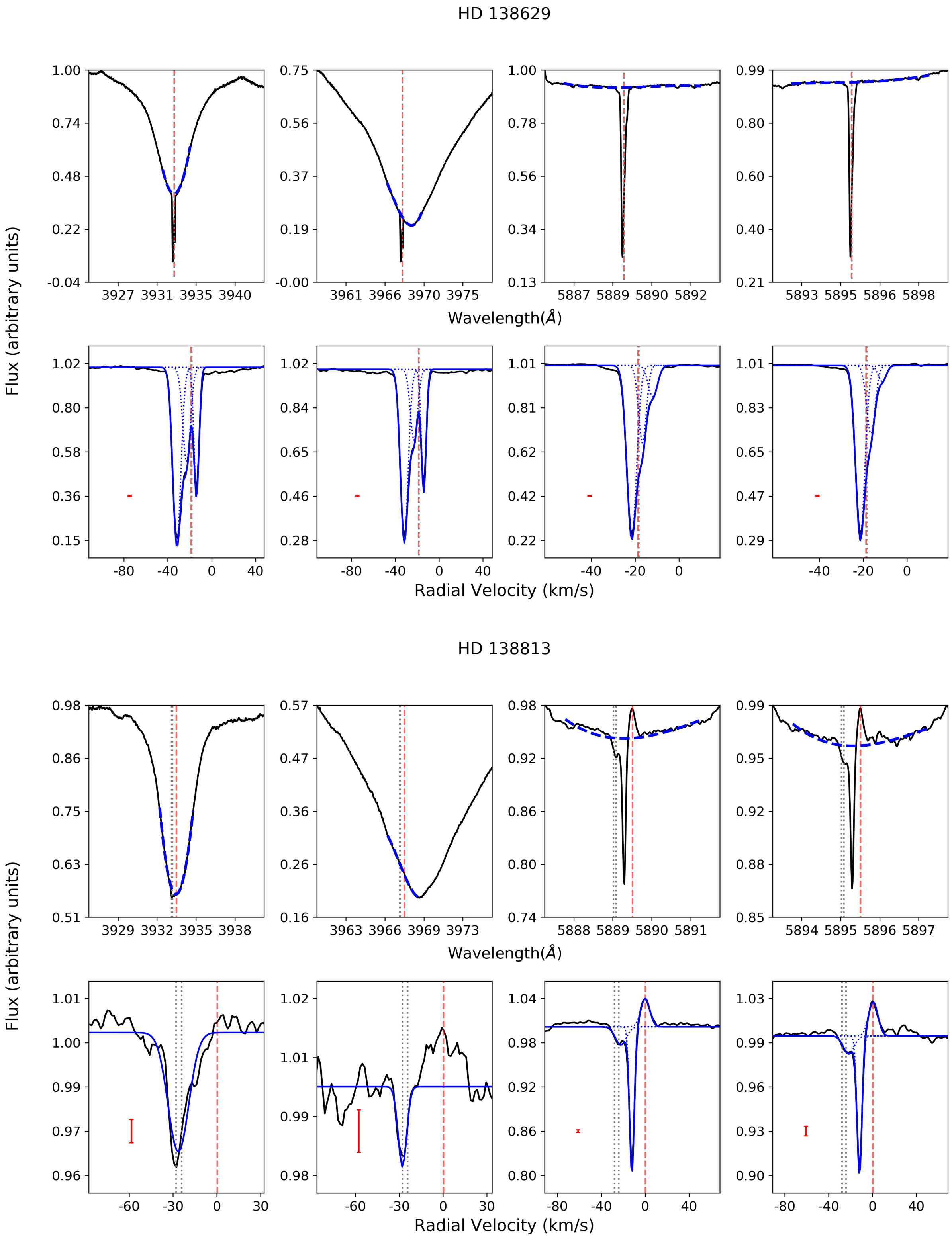

Fig. 1 (Cont.): Stars showing narrow non-photospheric absorptions. Top panels: Photospheric Ca ii H & K and Na i D lines with fitted modeling dashed blue line, x-axis shows the wavelength. Bottom panels: Residuals once the spectrum is divided by the photosphere, x-axis in velocity. Blue lines mark the fits to the non-photospheric absorptions. Vertical red dashed and grey dotted lines represent the stellar radial velocity and the ISM velocities respectively. Red error bars show three sigma value measured in the continuum adjacent to the photospheric line.

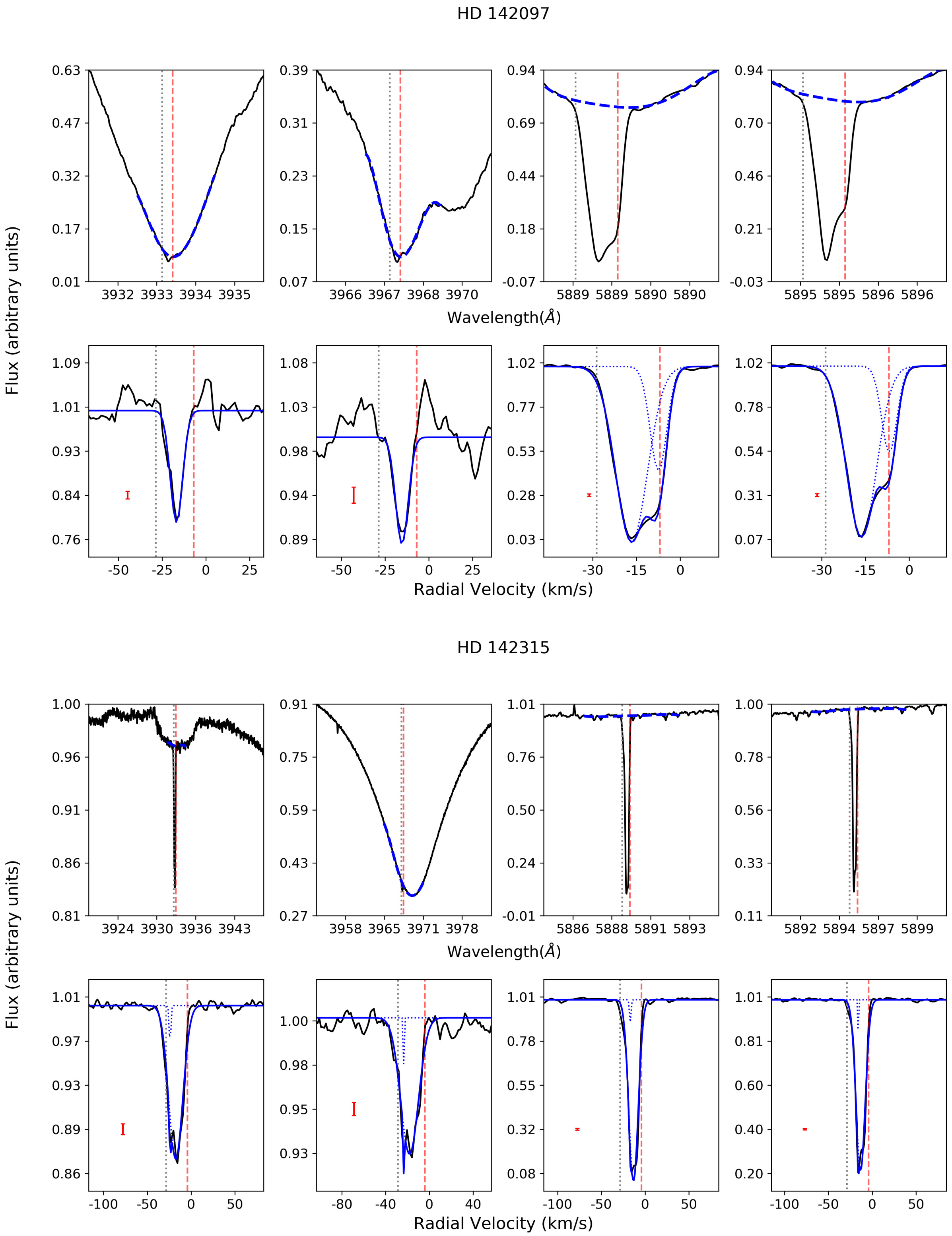

Fig. 1 (Cont.): Stars showing narrow non-photospheric absorptions. Top panels: Photospheric Ca II H & K and Na I D lines with fitted modeling dashed blue line, x-axis shows the wavelength. Bottom panels: Residuals once the spectrum is divided by the photosphere, x-axis in velocity. Blue lines mark the fits to the non-photospheric absorptions. Vertical red dashed and grey dotted lines represent the stellar radial velocity and the ISM velocities respectively. Red error bars show three sigma value measured in the continuum adjacent to the photospheric line.

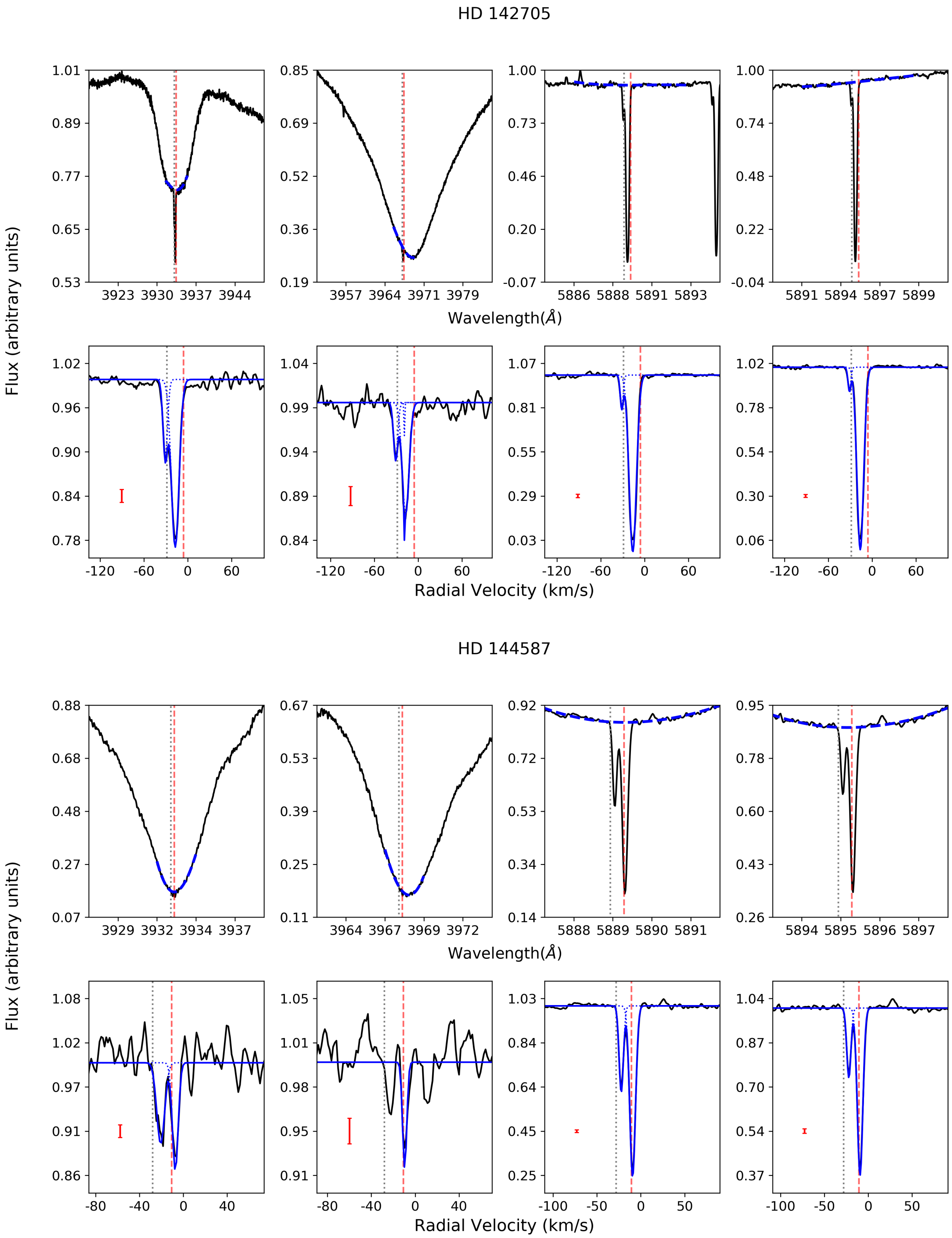

Fig. 1 (Cont.): Stars showing narrow non-photospheric absorptions. Top panels: Photospheric Ca II H & K and Na I D lines with fitted modeling dashed blue line, x-axis shows the wavelength. Bottom panels: Residuals once the spectrum is divided by the photosphere, x-axis in velocity. Blue lines mark the fits to the non-photospheric absorptions. Vertical red dashed and grey dotted lines represent the stellar radial velocity and the ISM velocities respectively. Red error bars show three sigma value measured in the continuum adjacent to the photospheric line.

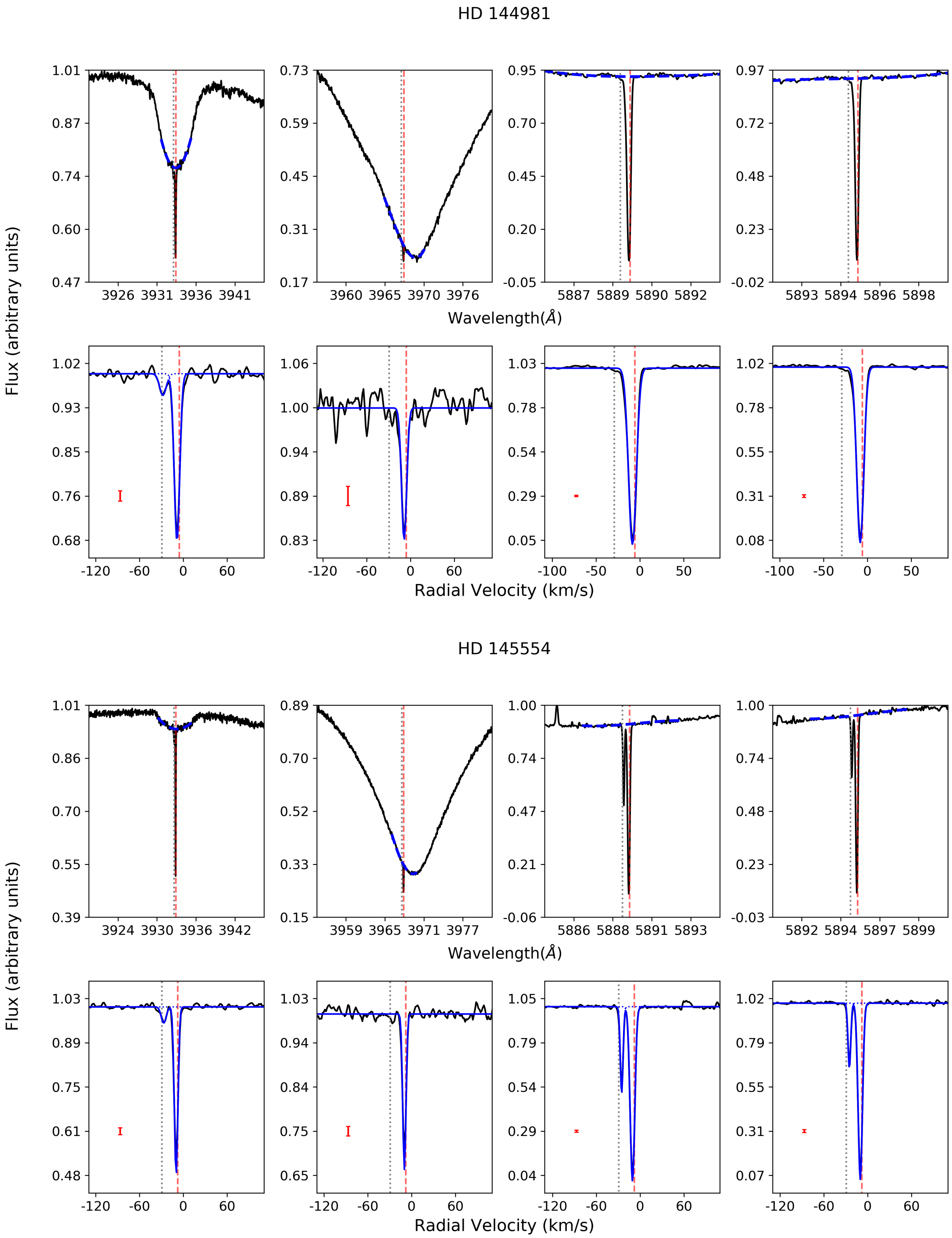

Fig. 1 (Cont.): Stars showing narrow non-photospheric absorptions. Top panels: Photospheric Ca ii H & K and Na i D lines with fitted modeling dashed blue line, x-axis shows the wavelength. Bottom panels: Residuals once the spectrum is divided by the photosphere, x-axis in velocity. Blue lines mark the fits to the non-photospheric absorptions. Vertical red dashed and grey dotted lines represent the stellar radial velocity and the ISM velocities respectively. Red error bars show three sigma value measured in the continuum adjacent to the photospheric line.

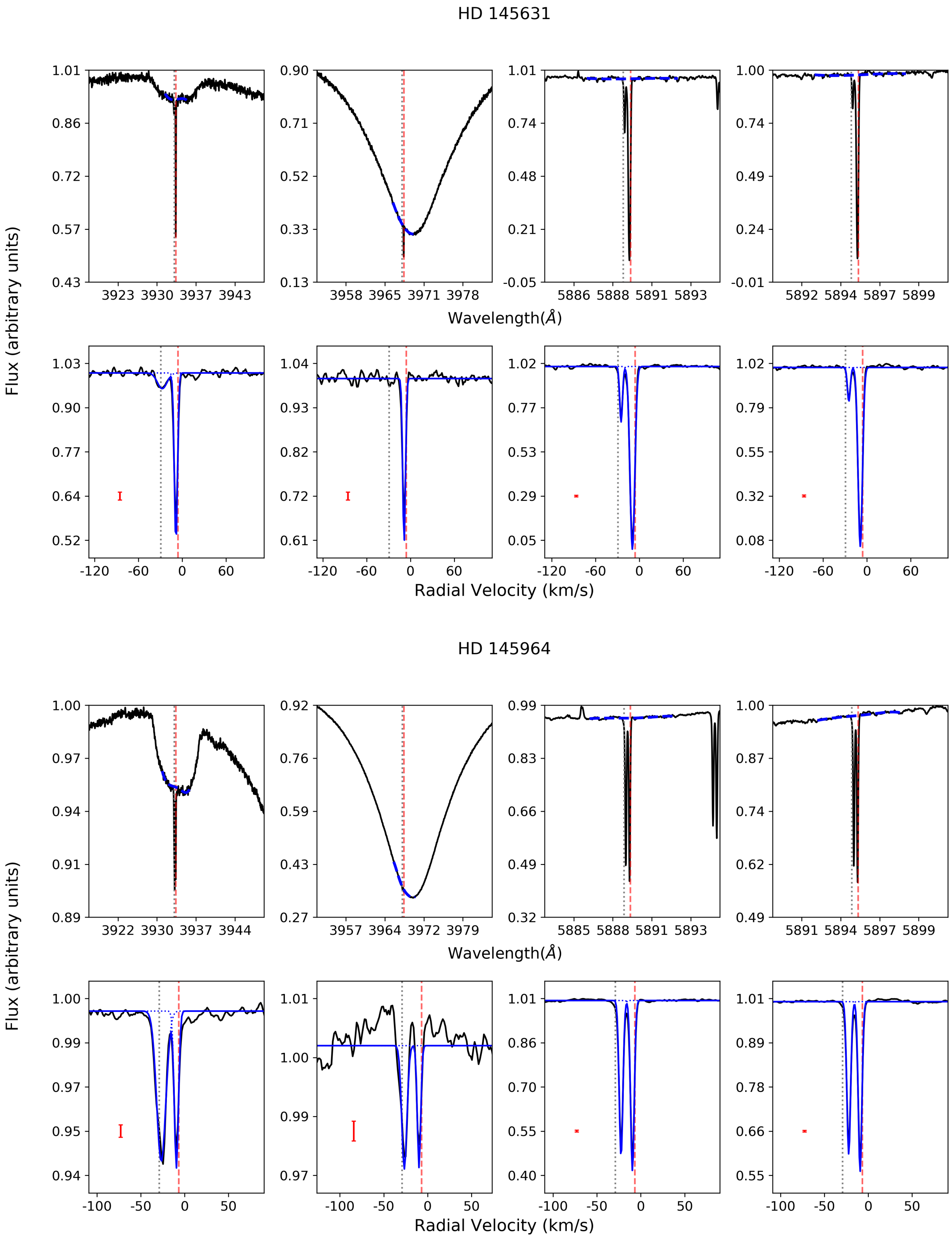

Fig. 1 (Cont.): Stars showing narrow non-photospheric absorptions. Top panels: Photospheric Ca II H & K and Na I D lines with fitted modeling dashed blue line, x-axis shows the wavelength. Bottom panels: Residuals once the spectrum is divided by the photosphere, x-axis in velocity. Blue lines mark the fits to the non-photospheric absorptions. Vertical red dashed and grey dotted lines represent the stellar radial velocity and the ISM velocities respectively. Red error bars show three sigma value measured in the continuum adjacent to the photospheric line.

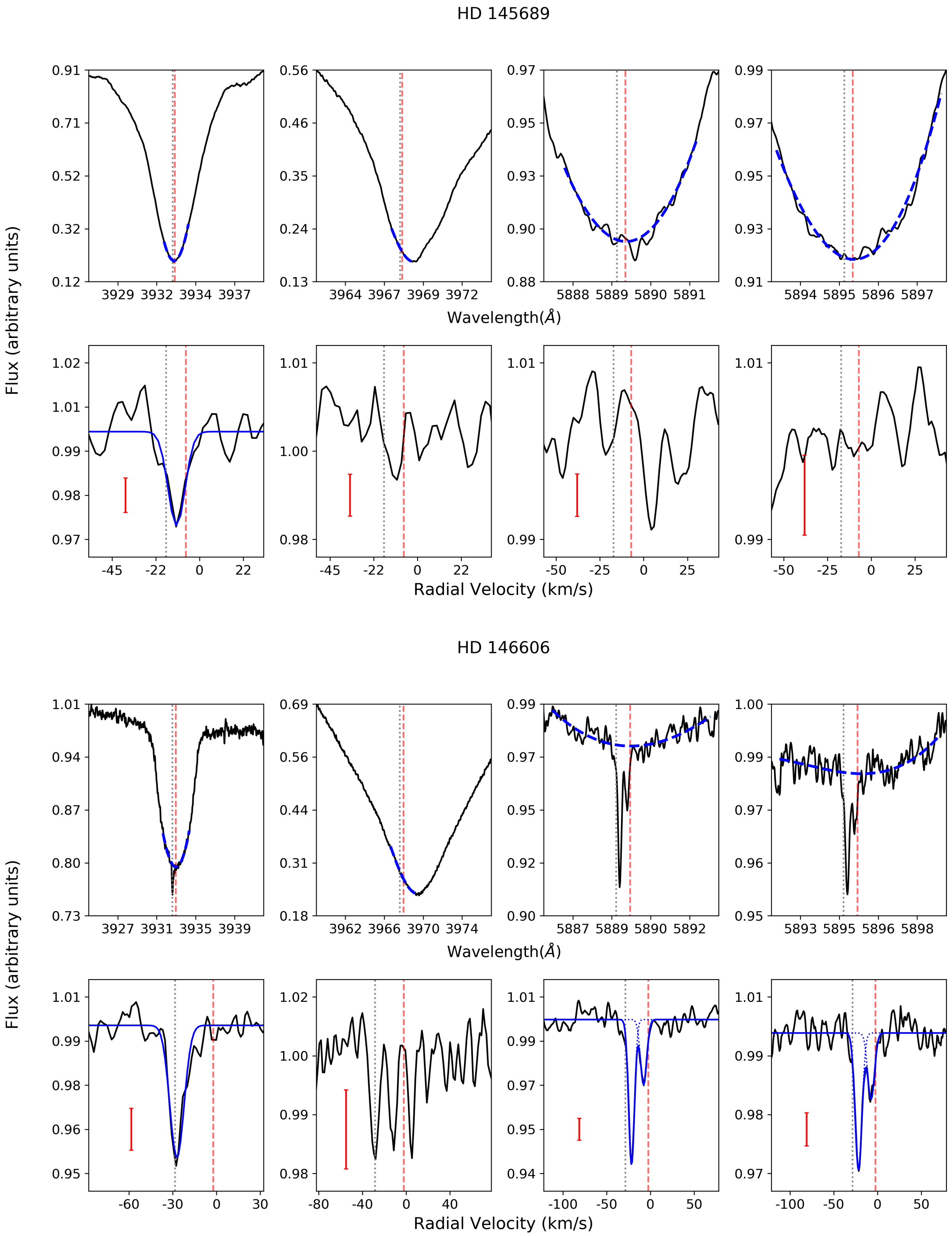

Fig. 1 (Cont.): Stars showing narrow non-photospheric absorptions. Top panels: Photospheric Ca II H & K and Na I D lines with fitted modeling dashed blue line, x-axis shows the wavelength. Bottom panels: Residuals once the spectrum is divided by the photosphere, x-axis in velocity. Blue lines mark the fits to the non-photospheric absorptions. Vertical red dashed and grey dotted lines represent the stellar radial velocity and the ISM velocities respectively. Red error bars show three sigma value measured in the continuum adjacent to the photospheric line.

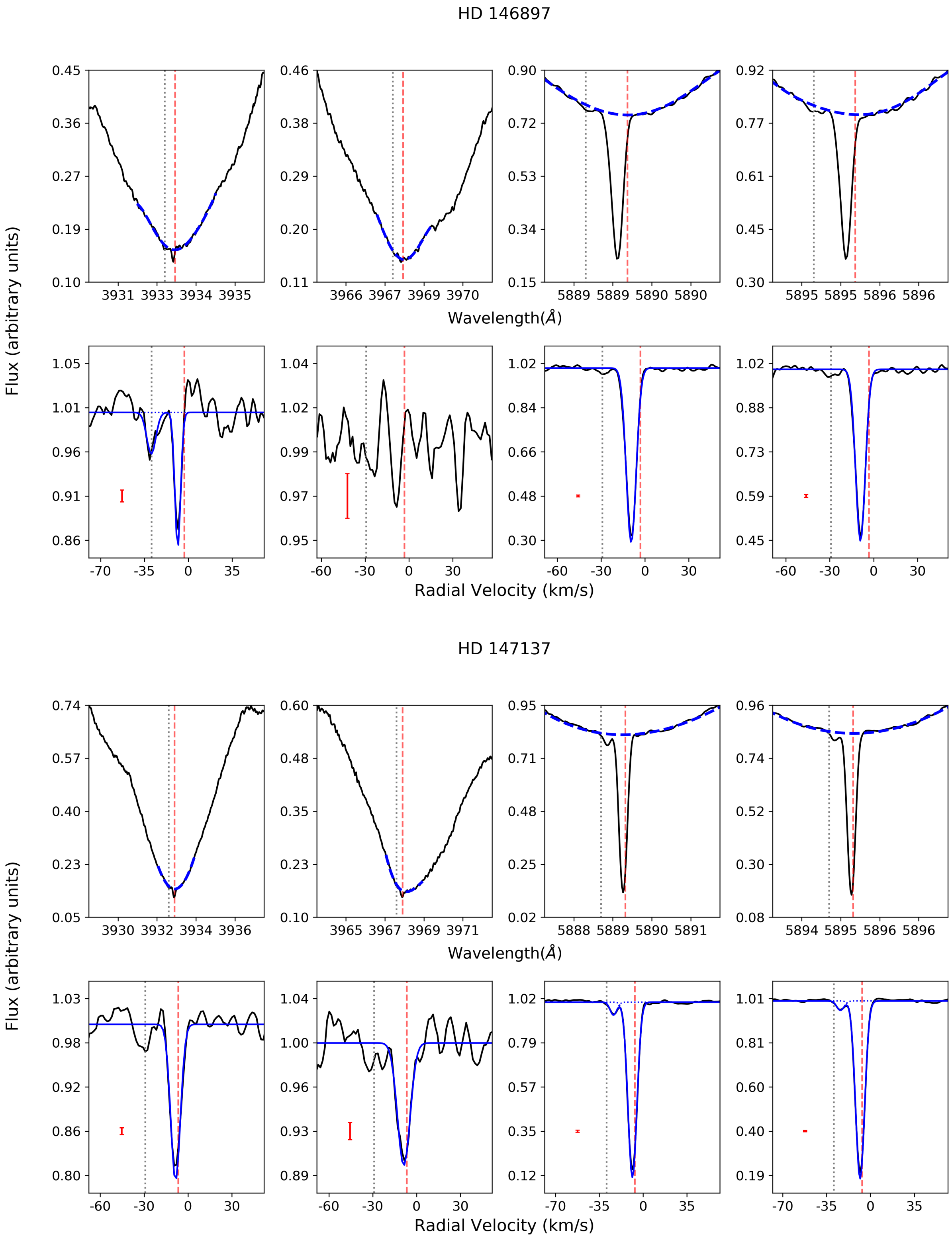

Fig. 1 (Cont.): Stars showing narrow non-photospheric absorptions. Top panels: Photospheric Ca II H & K and Na I D lines with fitted modeling dashed blue line, x-axis shows the wavelength. Bottom panels: Residuals once the spectrum is divided by the photosphere, x-axis in velocity. Blue lines mark the fits to the non-photospheric absorptions. Vertical red dashed and grey dotted lines represent the stellar radial velocity and the ISM velocities respectively. Red error bars show three sigma value measured in the continuum adjacent to the photospheric line.

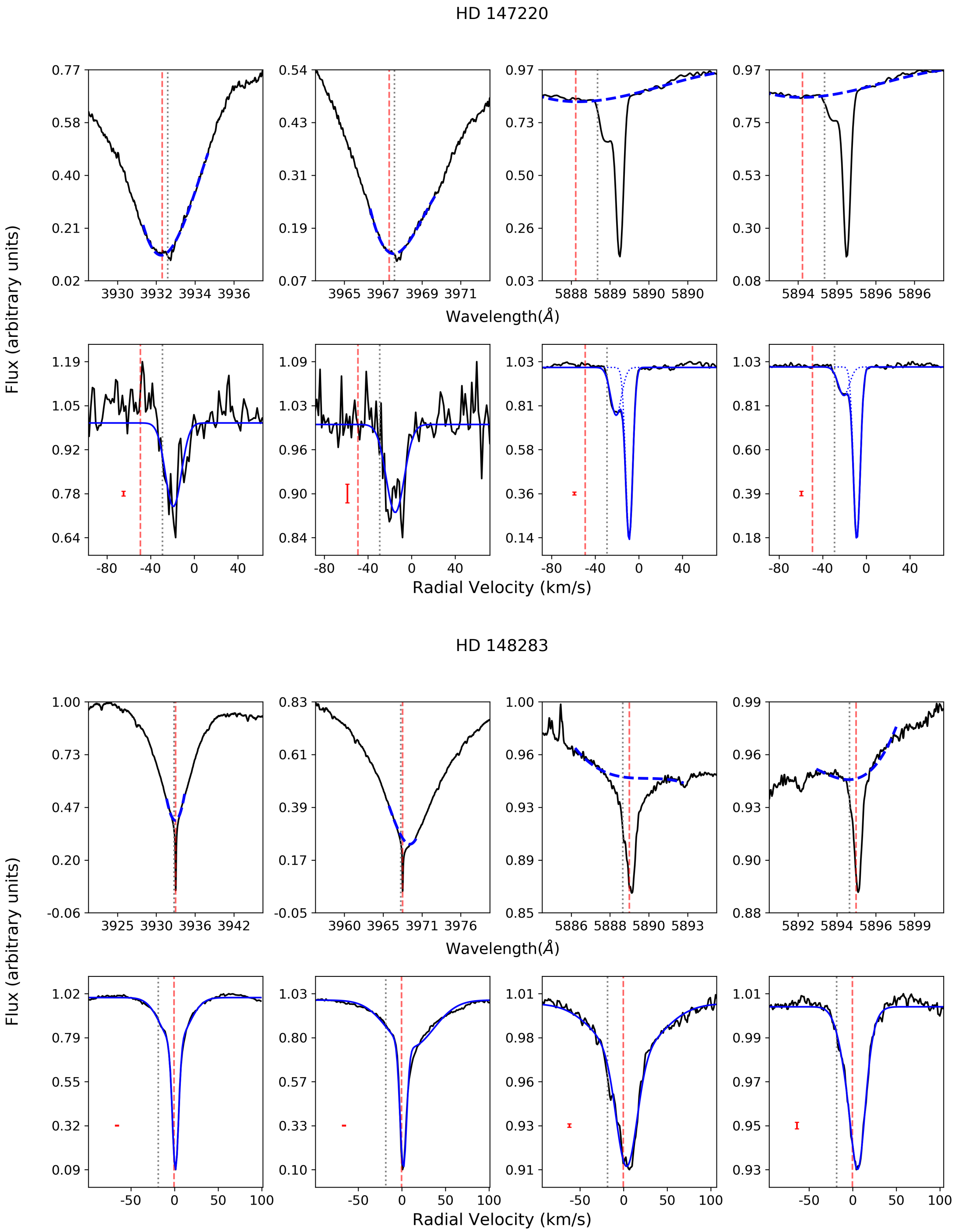

Fig. 1 (Cont.): Stars showing narrow non-photospheric absorptions. Top panels: Photospheric Ca II H & K and Na I D lines with fitted modeling dashed blue line, x-axis shows the wavelength. Bottom panels: Residuals once the spectrum is divided by the photosphere, x-axis in velocity. Blue lines mark the fits to the non-photospheric absorptions. Vertical red dashed and grey dotted lines represent the stellar radial velocity and the ISM velocities respectively. Red error bars show three sigma value measured in the continuum adjacent to the photospheric line.

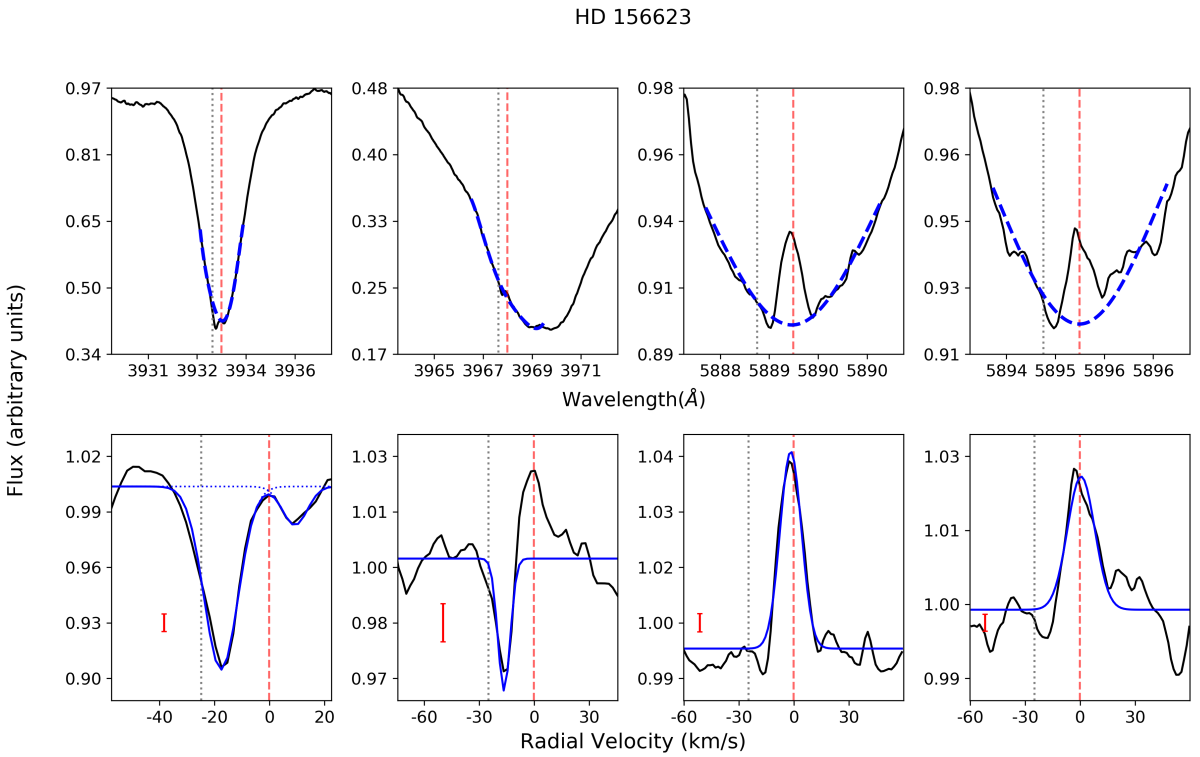

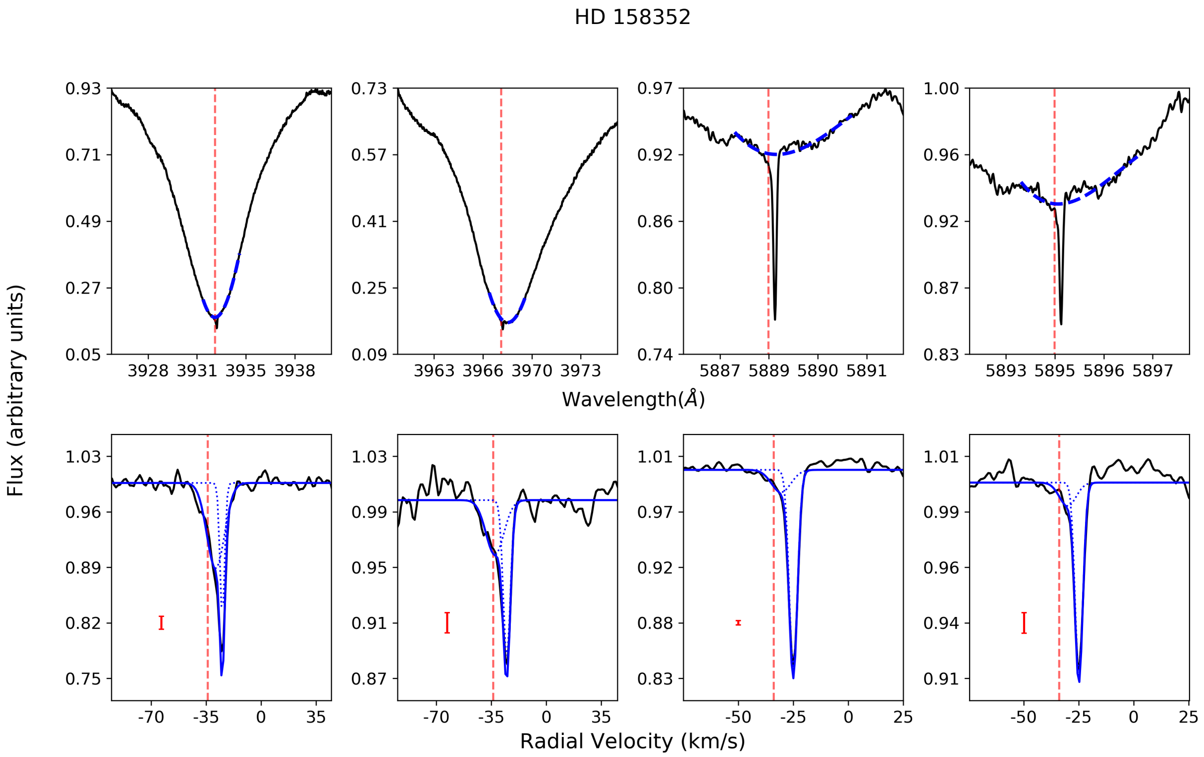

Fig. 1 (Cont.): Stars showing narrow non-photospheric absorptions. Top panels: Photospheric Ca II H & K and Na I D lines with fitted modeling dashed blue line, x-axis shows the wavelength. Bottom panels: Residuals once the spectrum is divided by the photosphere, x-axis in velocity. Blue lines mark the fits to the non-photospheric absorptions. Vertical red dashed and grey dotted lines represent the stellar radial velocity and the ISM velocities respectively. Red error bars show three sigma value measured in the continuum adjacent to the photospheric line.

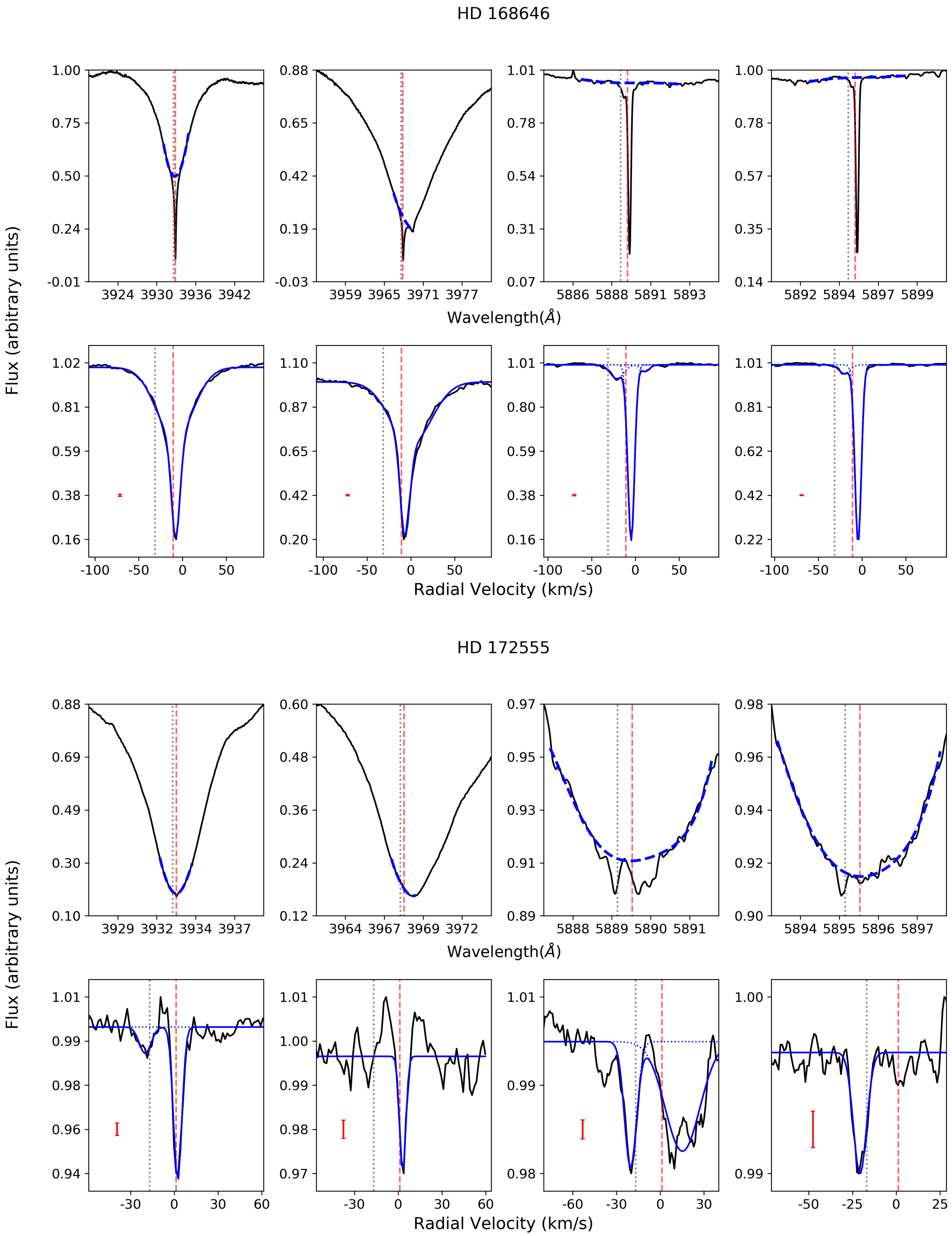

Fig. 1 (Cont.): Stars showing narrow non-photospheric absorptions. Top panels: Photospheric Ca II H & K and Na I D lines with fitted modeling dashed blue line, x-axis shows the wavelength. Bottom panels: Residuals once the spectrum is divided by the photosphere, x-axis in velocity. Blue lines mark the fits to the non-photospheric absorptions. Vertical red dashed and grey dotted lines represent the stellar radial velocity and the ISM velocities respectively. Red error bars show three sigma value measured in the continuum adjacent to the photospheric line.

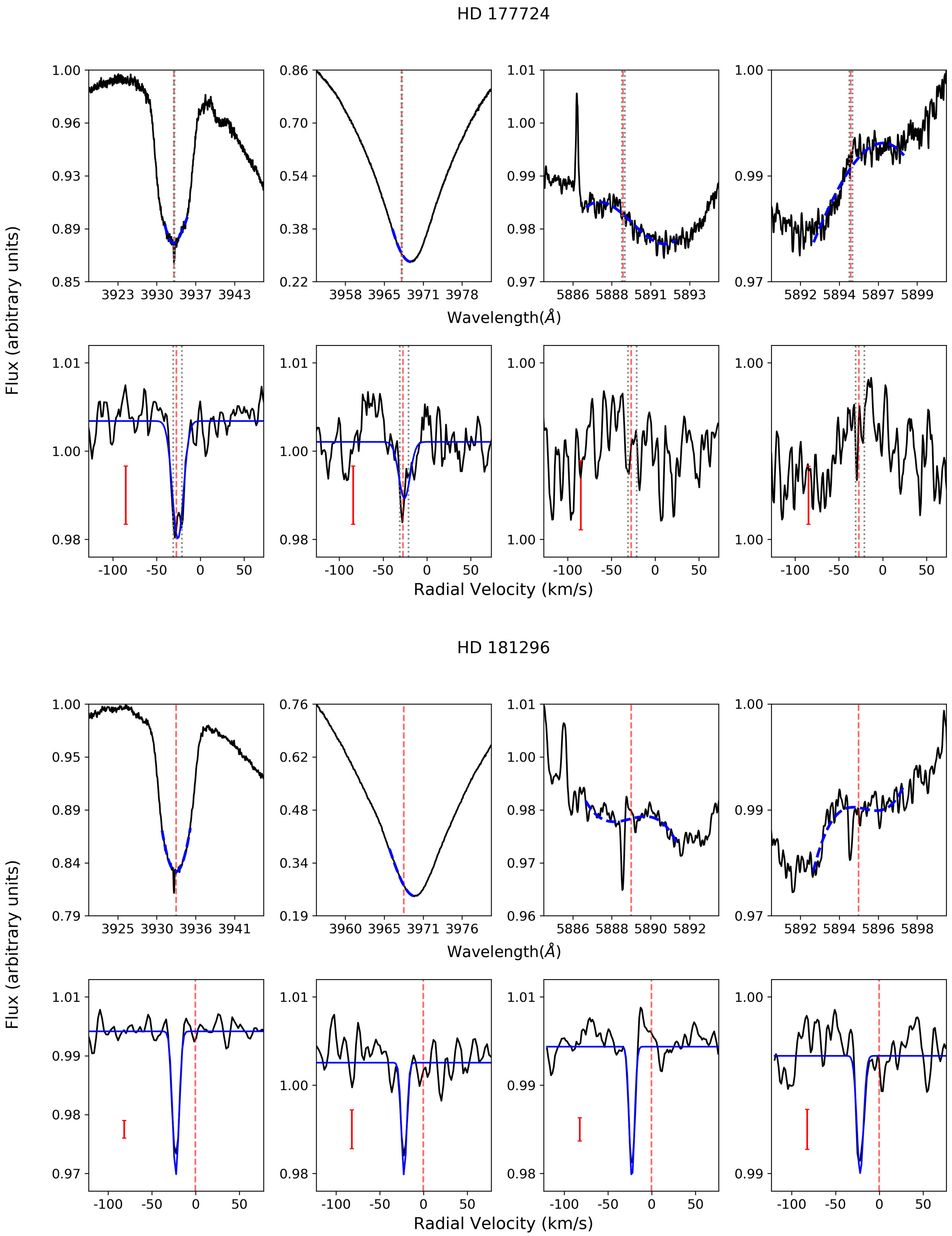

Fig. 1 (Cont.): Stars showing narrow non-photospheric absorptions. Top panels: Photospheric Ca II H & K and Na I D lines with fitted modeling dashed blue line, x-axis shows the wavelength. Bottom panels: Residuals once the spectrum is divided by the photosphere, x-axis in velocity. Blue lines mark the fits to the non-photospheric absorptions. Vertical red dashed and grey dotted lines represent the stellar radial velocity and the ISM velocities respectively. Red error bars show three sigma value measured in the continuum adjacent to the photospheric line.

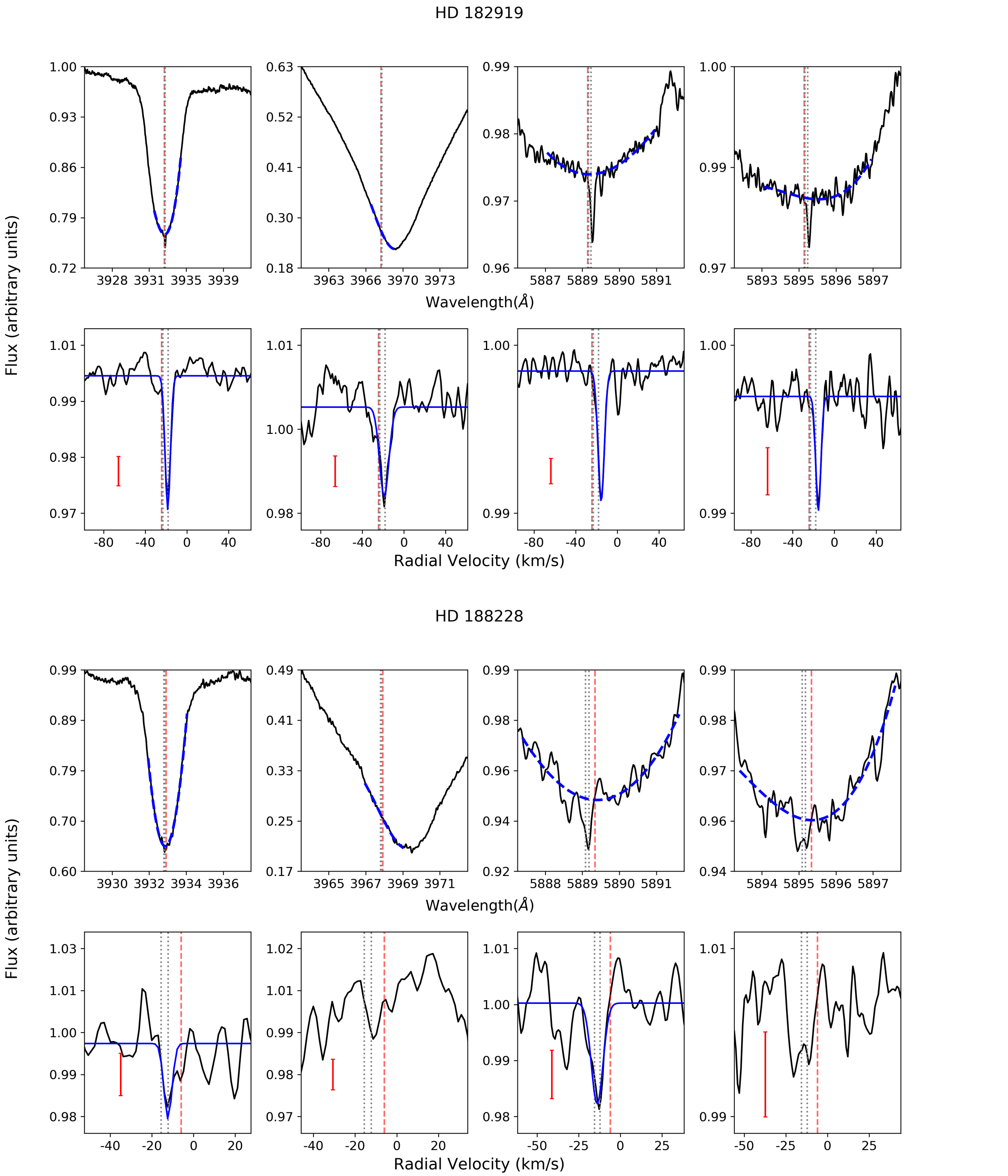

Fig. 1 (Cont.): Stars showing narrow non-photospheric absorptions. Top panels: Photospheric Ca II H & K and Na I D lines with fitted modeling dashed blue line, x-axis shows the wavelength. Bottom panels: Residuals once the spectrum is divided by the photosphere, x-axis in velocity. Blue lines mark the fits to the non-photospheric absorptions. Vertical red dashed and grey dotted lines represent the stellar radial velocity and the ISM velocities respectively. Red error bars show three sigma value measured in the continuum adjacent to the photospheric line.

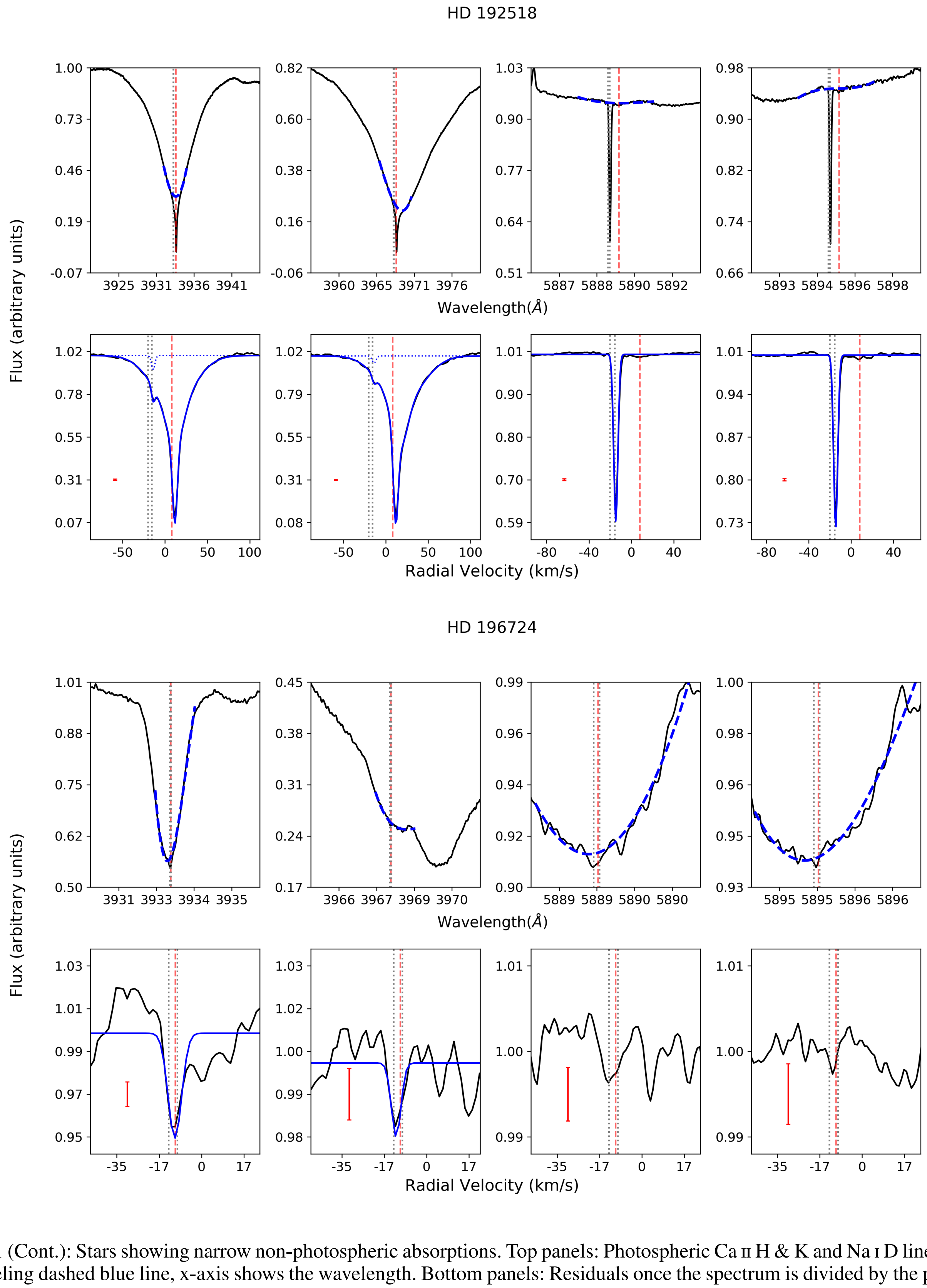

Fig. 1 (Cont.): Stars showing narrow non-photospheric absorptions. Top panels: Photospheric Ca II H & K and Na I D lines with fitted modeling dashed blue line, x-axis shows the wavelength. Bottom panels: Residuals once the spectrum is divided by the photosphere, x-axis in velocity. Blue lines mark the fits to the non-photospheric absorptions. Vertical red dashed and grey dotted lines represent the stellar radial velocity and the ISM velocities respectively. Red error bars show three sigma value measured in the continuum adjacent to the photospheric line.

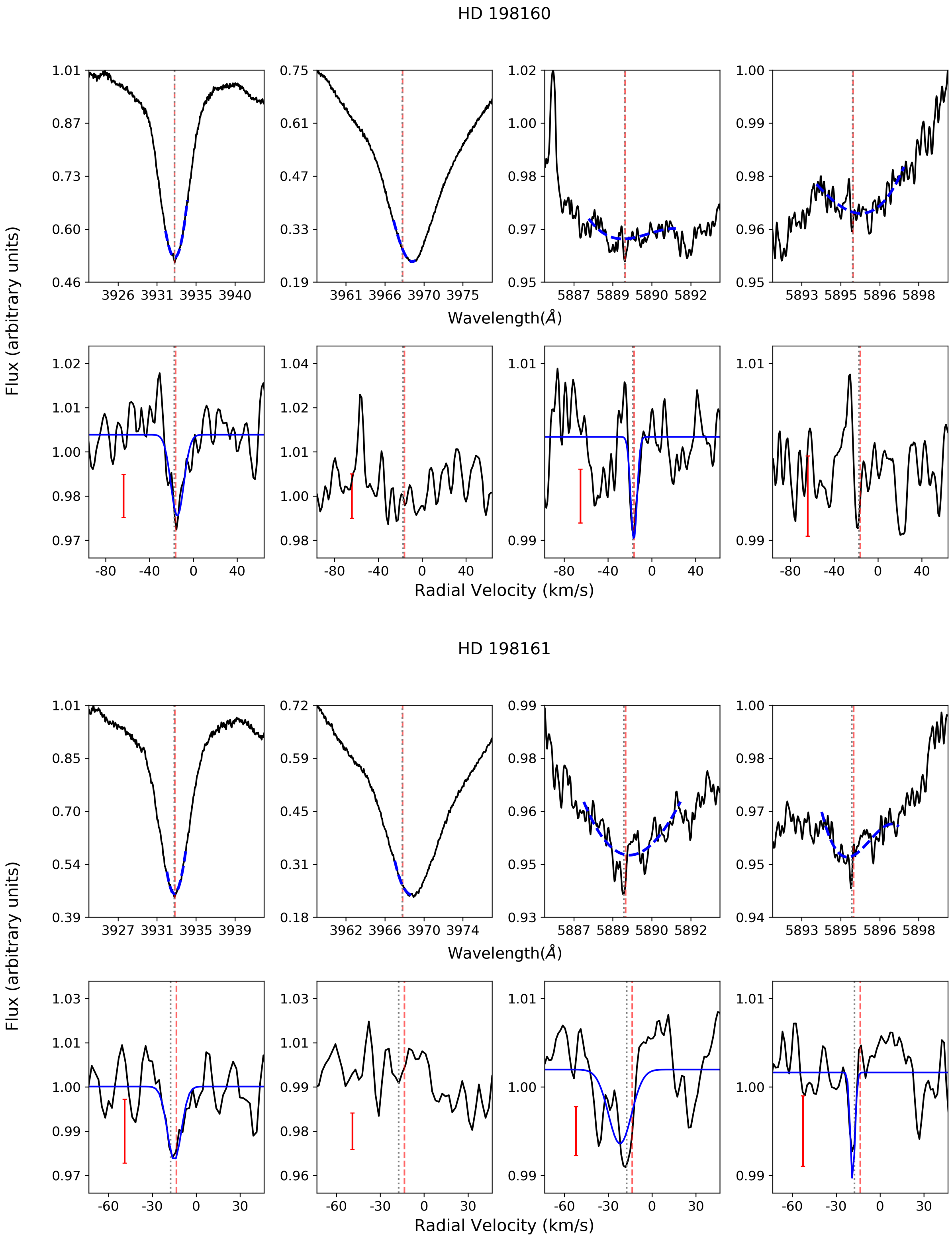

Fig. 1 (Cont.): Stars showing narrow non-photospheric absorptions. Top panels: Photospheric Ca II H & K and Na I D lines with fitted modeling dashed blue line, x-axis shows the wavelength. Bottom panels: Residuals once the spectrum is divided by the photosphere, x-axis in velocity. Blue lines mark the fits to the non-photospheric absorptions. Vertical red dashed and grey dotted lines represent the stellar radial velocity and the ISM velocities respectively. Red error bars show three sigma value measured in the continuum adjacent to the photospheric line.

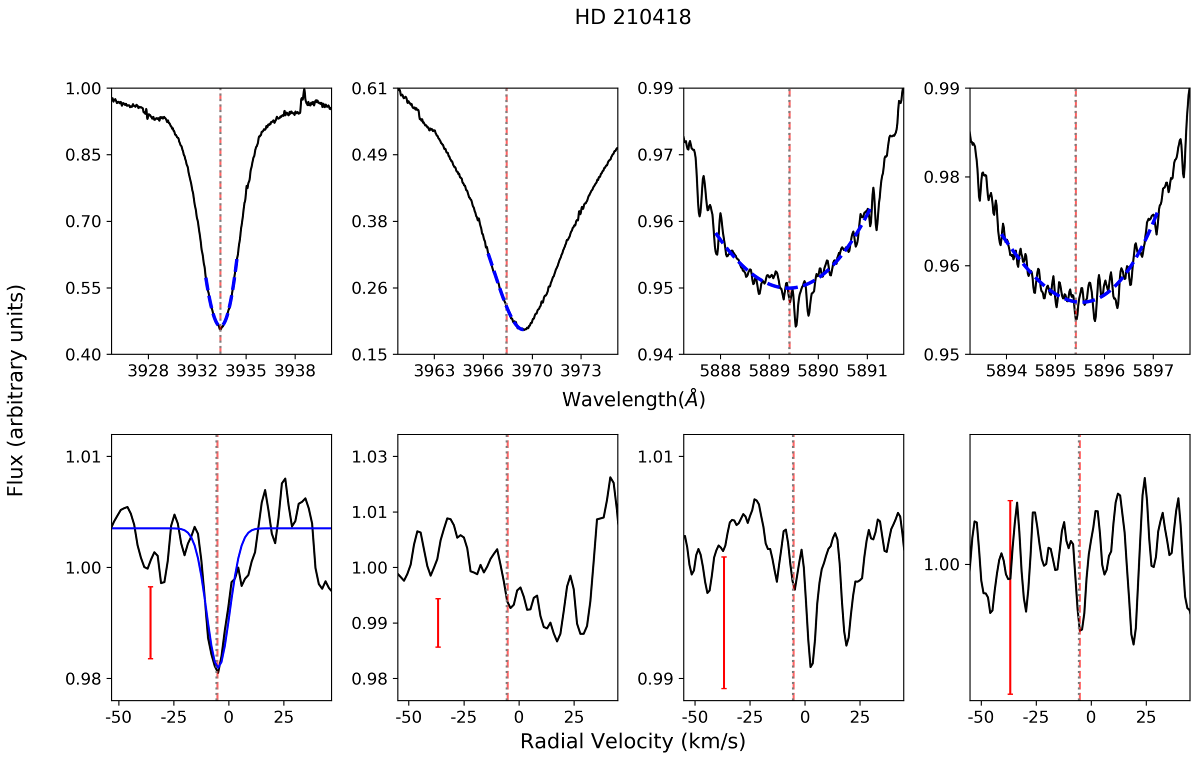

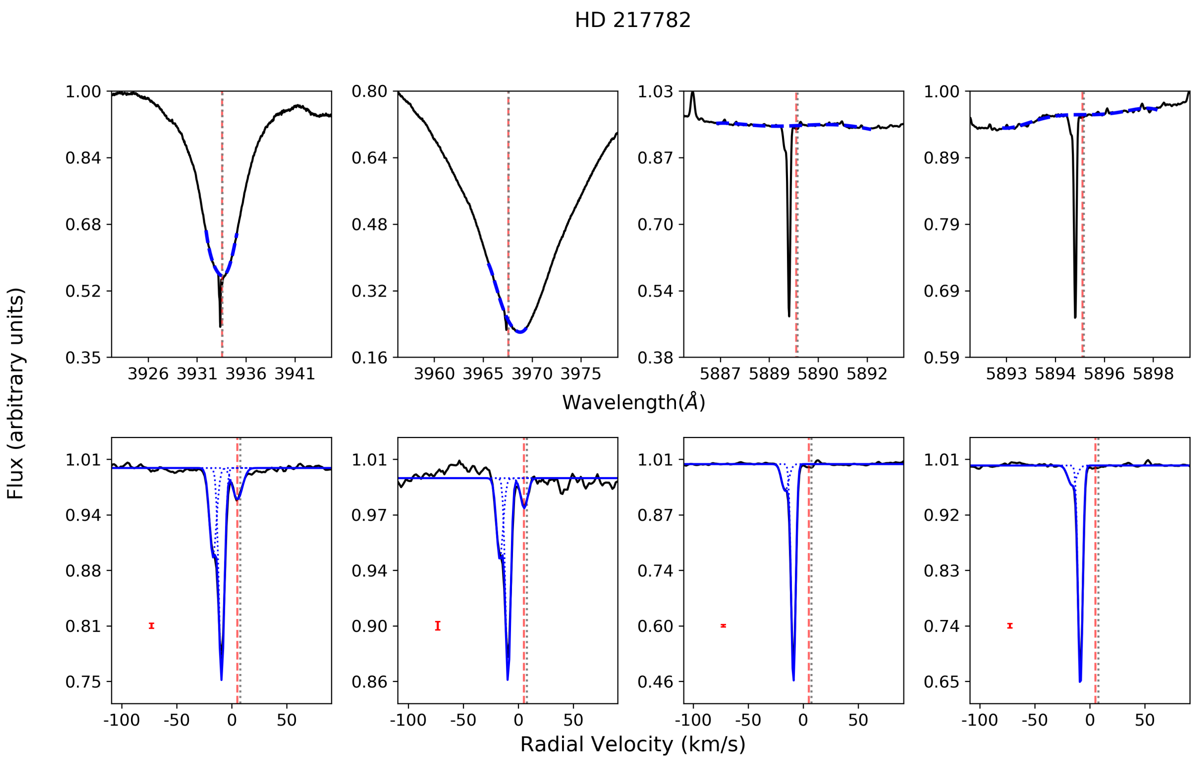

Fig. 1 (Cont.): Stars showing narrow non-photospheric absorptions. Top panels: Photospheric Ca ii H & K and Na i D lines with fitted modeling dashed blue line, x-axis shows the wavelength. Bottom panels: Residuals once the spectrum is divided by the photosphere, x-axis in velocity. Blue lines mark the fits to the non-photospheric absorptions. Vertical red dashed and grey dotted lines represent the stellar radial velocity and the ISM velocities respectively. Red error bars show three sigma value measured in the continuum adjacent to the photospheric line.

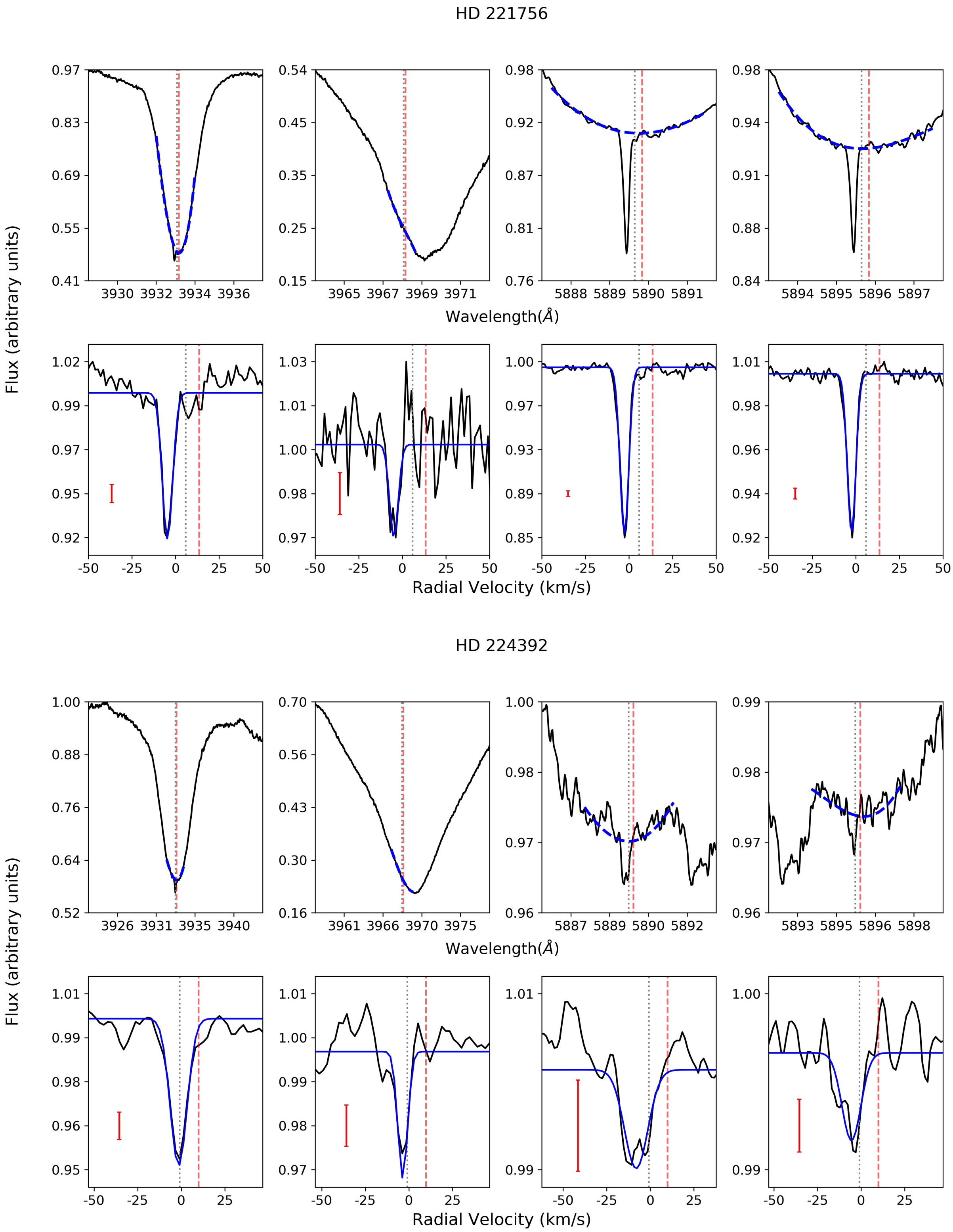

Fig. 1 (Cont.): Stars showing narrow non-photospheric absorptions. Top panels: Photospheric Ca ii H & K and Na i D lines with fitted modeling dashed blue line, x-axis shows the wavelength. Bottom panels: Residuals once the spectrum is divided by the photosphere, x-axis in velocity. Blue lines mark the fits to the non-photospheric absorptions. Vertical red dashed and grey dotted lines represent the stellar radial velocity and the ISM velocities respectively. Red error bars show three sigma value measured in the continuum adjacent to the photospheric line.

Appendix B: Tables

Table B.1: Sample of observed stars. Columns are self-explanatory. Numbers within parenthesis in columns 10 to 13 denote the corresponding references. Column 13 specifies the primary selection criteria as described in the text: 1. Previously detected exocomets; 2. Debris Discs; 3. Debris discs with cold gas; 4. Near-Infrared excesses; 5. Young discs; 6. Shell Stars; 7. λ Boo stars.

HD	Other Name	RA(2000.0)	Dec(2000.0)	Sp. Type	Distance (pc)	V (mag)	B-V (mag)	V_{rad} (km/s)	Age (Myr)	L_{IR} / L_*	Assoc.	Sel.Crit
105	HIP 490	00 : 05 : 52.54	−41 : 45 : 11.0	G0V	38.85	7.53	0.6	1.7	45 (9)	$2.4\cdot 10^{-4}$ (1)	Tuc-Hor (4)	5 (1)
203	HR 9	00 : 06 : 50.09	−23 : 06 : 27.1	F3V	39.96	6.19	0.344	6.5	23 (2)	$1.6\cdot 10^{-4}$ (2)	BPMG (3)	5 (2)
256	HR 10	00 : 07 : 18.27	−17 : 23 : 13.2	A2IV/V	145.18	6.23	0.1	-10.2	549 (3)	$<6.1\cdot 10^{-6}$ (3)		1 (3)
1466	HIP 1481	00 : 18 : 26.12	−63 : 28 : 39.0	F8V	42.97	7.46	0.54	6.4	45 (9)	$6.3\cdot 10^{-5}$ (1)	Tuc-Hor (4)	5 (1)
2262	κ Phe	00 : 26 : 12.20	−43 : 40 : 47.4	A5IV	23.81	3.94	0.17	11.3	200 (1)	$7.4\cdot 10^{-6}$ (4)	Castor (1)	4 (4)
2884	β 1 Tuc	00 : 31 : 32.67	−62 : 57 : 29.6	B9V	41.41	4.33	-0.045	14.0	45 (9)	$<6.7\cdot 10^{-6}$ (1)	Tuc-Hor (4)	5 (1)
2885	β 2 Tuc	00 : 31 : 33.48	−62 : 57 : 56.0	A2V	51.04	4.51	0.135	9.8	45 (9)	$<1.8\cdot 10^{-5}$ (1)	Tuc-Hor (4)	5 (1)
3003	β 3 Tuc	00 : 32 : 43.91	−63 : 01 : 53.4	A0V	45.90	5.09	0.04	7.7	45 (9)	$1.1\cdot 10^{-4}$ (1)	Tuc-Hor (4)	5 (1)
5267	66 Psc	00 : 54 : 35.23	+19 : 11 : 18.3	A1V	108.11	5.79	-0.03	8.5	200 (1)	$3.9\cdot 10^{-5}$ (6)		2 (5)
5448	μ And	00 : 56 : 45.21	+38 : 29 : 57.6	A5V	41.26	3.87	0.12	7.2	687 (3)	$<4.4\cdot 10^{-6}$(4)		4 (6)
7788	κ Tuc	01 : 15 : 46.16	−68 : 52 : 33.3	F6V+K1V	20.96	4.25	0.48	7.7	700 (4)	$<4.4\cdot 10^{-6}$ (8)		4 (4)
9672	49 Cet	01 : 34 : 37.78	−15 : 40 : 34.9	A1V	57.07	5.62	0.062	10.3	40 (5)	$1.1\cdot 10^{-3}$ (7)	Argus (7)	1 (7)
10700	τ Cet	01 : 44 : 04.08	−15 : 56 : 14.9	G8.5V	3.65	3.5	0.72	-16.62	5800 (6)	$6.1\cdot 10^{-6}$ (8)		4 (8)
12039	DK Cet	01 : 57 : 48.98	−21 : 54 : 05.3	G4V	41.41	8.06	0.673	6.12	45 (9)	$6.3\cdot 10^{-5}$ (1)	Tuc-Hor (4)	5 (1)
14055	γ Tri	02 : 17 : 18.87	+33 : 50 : 49.9	A1V	34.44	4.0	0.03	9.9	300 (1)	$7.4\cdot 10^{-5}$ (4)		2 (9)
14412	HR 683	02 : 18 : 58.50	−25 : 56 : 44.5	G8V	12.83	6.34	0.73	7.36	6540 (7)	$<2.0\cdot 10^{-6}$ (9)		4 (4)
15115	HIP 11360	02 : 26 : 16.24	+06 : 17 : 33.2	F2V	49.00	6.8	0.35	0.81	45 (9)	$4.8\cdot 10^{-4}$ (10)	Tuc-Hor (8)	2 (10)
15257	HR 717	02 : 28 : 09.98	+29 : 40 : 09.6	F0III	49.93	5.29	0.29	-24.8	1000 (1)	$8.6\cdot 10^{-5}$ (6)		2 (5)
16978	HR 806	02 : 39 : 35.36	−68 : 16 : 01.0	B9III	46.55	4.11	-0.046	13.6	45 (9)	$<8.6\cdot 10^{-7}$(1)	Tuc-Hor (4)	5 (1)
21688	HR 1062	03 : 29 : 36.03	−12 : 40 : 29.1	A5III/IV	143.21	5.58	0.152	15.1	625 (3)			6 (11)
21620	HR 1056	03 : 31 : 29.34	+49 : 12 : 35.2	A0V	135.00	6.28	0.07	-21.4	80 (17)	$2.5\cdot 10^{-5}$ (11)		1 (7)
21997	HR 1082	03 : 31 : 53.65	−25 : 36 : 50.9	A3IV/V	69.64	6.37	0.13	17.3	42 (9)	$5.7\cdot 10^{-4}$ (7)	Columba (1)	3 (10)
22484	10 Tau	03 : 36 : 52.38	+00 : 24 : 06.0	F8V	13.96	4.3	0.85	28.07	7500 (6)	$1.1\cdot 10^{-5}$ (8)		4 (8)
27290	HR 1338	04 : 16 : 01.59	−51 : 29 : 11.9	F1V	20.45	4.2	0.35	25.2	45 (1)	$1.9\cdot 10^{-5}$ (8)	IC 2391 (1)	2 (9)
28355	b Tau	04 : 28 : 50.16	+13 : 02 : 51.4	A7V	48.57	5.01	0.212	37.3	600 (1)	$4.7\cdot 10^{-5}$ (6)	Hyades (1)	4 (4)
29391	HR 1474	04 : 37 : 36.13	−02 : 28 : 24.8	F0IV	29.78	5.22	0.262	12.6	23 (2)	$2.3\cdot 10^{-6}$ (2)	BPMG (3)	5 (2)
30051	HIP 21965	04 : 43 : 17.20	−23 : 37 : 42.0	F2V	63.59	7.11	0.4	19.3	45 (9)	$2.8\cdot 10^{-5}$ (1)	Tuc-Hor (4)	5 (2)
31295	π 1 Ori	04 : 54 : 53.73	+10 : 09 : 03.0	A3V	35.66	4.66	0.081	11.1	123 (1)	$7.6\cdot 10^{-5}$ (5)		7 (12)
32297	HIP 23451	05 : 02 : 27.44	+07 : 27 : 39.7	A0V	132.79	8.14	0.18	23.0	30 (10)	$4.4\cdot 10^{-3}$ (6)		1 (13)
35850	AF Lep	05 : 27 : 04.76	−11 : 54 : 03.5	F8V	26.88	6.31	0.503	17.0	23 (2)	$3.7\cdot 10^{-5}$ (2)	BPMG (3)	5 (2)
36546	HIP 26062	05 : 33 : 30.76	+24 : 37 : 43.7	B8V	101.35	6.95	0.07	20.4	10 (11)	$4.0\cdot 10^{-3}$ (12)		2 (14)
37286	HR 1915	05 : 36 : 10.30	−28 : 42 : 28.8	A2IV	58.89	6.27	0.149	22.4	45 (9)	$1.0\cdot 10^{-4}$ (6)	Tuc-Hor (1)	2 (5)
37306	HR 1919	05 : 37 : 08.77	−11 : 46 : 31.9	A2V	70.46	6.09	0.056	23.0	42 (9)	$1.2\cdot 10^{-4}$ (6)	Columba (2)	2 (5)
38206	HR 1975	05 : 43 : 21.67	−18 : 33 : 26.9	A0V	71.41	5.73	-0.011	25.3	42 (9)	$1.4\cdot 10^{-4}$ (6)	Columba (1)	2 (5)
39182	HR 2025	05 : 52 : 39.67	+39 : 34 : 28.9	A2V	202.46	6.39	0.09	-14.5	407 (3)			6 (11)
39283	ξ Aur	05 : 54 : 50.78	+55 : 42 : 25.0	A2V	72.51	4.96	0.045	-11.8	540 (8)	$<3.1\cdot 10^{-6}$ (11)		6 (15)
40136	η Lep	05 : 56 : 24.29	−14 : 10 : 03.7	F2V	14.88	3.72	0.33	-2.14	1390 (1)	$2.6\cdot 10^{-5}$ (6)		4 (8)
42111	HR 2174	06 : 08 : 57.90	+02 : 29 : 58.9	A3V	178.42	5.73	0.07	25.3	319 (3)	$<1.0\cdot 10^{-5}$ (11)		1 (7)
53842	HIP 32435	06 : 46 : 13.54	−83 : 59 : 29.5	F5V	58.87	8.62	0.258	12.2	45 (9)	$<2.1\cdot 10^{-4}$ (6)	Tuc-Hor (4)	5 (1)
50241	α Pic	06 : 48 : 11.46	−61 : 56 : 29.0	A8V	29.60	3.3	0.18	15.3	885 (8)	$<4.4\cdot 10^{-6}$ (4)		1 (15)
50571	HR 2562	06 : 50 : 01.01	−60 : 14 : 56.9	F5V	33.64	6.1	0.45	22.1	300 (1)	$1.5\cdot 10^{-4}$ (10)	B3 (1)	2 (9)
56537	λ Gem	07 : 18 : 05.58	+16 : 32 : 25.4	A4IV	30.93	3.58	0.111	-7.4	314 (1)	$<4.4\cdot 10^{-6}$ (4)	UMA (1)	4 (8)
64145	ϕ Gem	07 : 53 : 29.81	+26 : 45 : 56.8	A5IV	76.31	4.96	0.097	8.0	714 (8)			1 (16)
71043	HR 3300	08 : 22 : 55.16	−52 : 07 : 25.4	A0V	73.25	5.89	0.016	22.5	45 (9)	$6.7\cdot 10^{-5}$ (6)	Tuc-Hor (2)	2 (15)
71722	HR 3341	08 : 26 : 25.21	−52 : 48 : 27.0	A0V	69.33	6.05	0.057	30.2	324 (1)	$8.4\cdot 10^{-5}$ (6)		2 (9)
74873	HR 3481	08 : 46 : 56.02	+12 : 06 : 35.8	A1VP	56.19	5.88	0.107	23.3	539 (1)	$4.8\cdot 10^{-5}$ (5)		7 (12)
77190	67 Cnc	09 : 01 : 48.84	+27 : 54 : 09.3	A8Vn	59.65	6.07	0.22	12.0	19 (8)	$<1.3\cdot 10^{-5}$ (11)		6 (15)

Continued on next page

Table B.1 – continued from previous page

HD	Other Name	RA(2000.0)	Dec(2000.0)	Sp. Type	Distance (pc)	V (mag)	B-V (mag)	v_{rad} (km/s)	Age (Myr)	L_{IR} / $L_\star$	Assoc.	Sel.Crit
80007	HR 3685	09 : 13 : 11.98	−69 : 43 : 01.9	A1III	34.70	1.69	0.0	-5.1	260 (12)	<$1.7\cdot 10^{-6}$ (3)		1 (3)
85905	HR 3921	09 : 54 : 31.82	−22 : 29 : 14.9	A1IV	176.03	6.23	0.044	9.2	481 (3)	<$4.8\cdot 10^{-6}$ (3)		1 (3)
95418	β UMa	11 : 01 : 50.48	+56 : 22 : 56.7	A1IV	24.45	2.37	-0.02	-13.1	320 (1)	$1.4\cdot 10^{-5}$ (4)	UMA (1)	2 (9)
98058	ϕ Leo	11 : 16 : 39.70	−03 : 39 : 05.8	A7IV	56.47	4.47	0.198	-3.0	921 (8)	<$7.4\cdot 10^{-5}$ (23)		6 (11)
102647	β Leo	11 : 49 : 03.58	+14 : 34 : 19.4	A3Va	11.00	2.13	0.09	-0.2	45 (1)	$2.2\cdot 10^{-5}$ (4)	IC 2391 (1)	4 (8)
104731	HR 4600	12 : 03 : 39.57	−42 : 26 : 02.6	F5V	24.73	5.15	0.41	38.5	360 (6)		CANE (1)	4 (4)
104860	HIP 58876	12 : 04 : 33.73	+66 : 20 : 11.7	F8	45.20	7.91	0.59	-11.73	3140 (1)	$3.0\cdot 10^{-4}$ (6)		2 (9)
105234	EF Cha	12 : 07 : 05.52	−78 : 44 : 28.0	A9III/4	104.54	7.46	0.28	0.0	10 (1)	$1.0\cdot 10^{-3}$ (13)		2 (5)
105850	HR 4635	12 : 11 : 03.84	−23 : 36 : 08.7	A1V	58.81	5.47	0.05	11.0	45 (9)	$6.2\cdot 10^{-5}$ (6)	Tuc-Hor (2)	2 (5)
108767	δ Crv	12 : 29 : 51.86	−16 : 30 : 55.6	A0IV	26.63	2.94	-0.05	13.9	216 (8)	<$4.4\cdot 10^{-6}$ (4)		4 (4)
109085	η Crv	12 : 32 : 04.23	−16 : 11 : 45.6	F2V	18.28	4.31	0.38	-2.8	1400 (13)	$3.4\cdot 10^{-4}$ (14)		3 (17)
109573	HR 4796	12 : 36 : 01.03	−39 : 52 : 10.2	A0V	71.91	5.78	0.009	7.1	8 (1)	$4.6\cdot 10^{-3}$ (15)	TWA (1)	2 (5)
110058	HIP 61782	12 : 39 : 46.20	−49 : 11 : 55.5	A0V	129.98	7.97	0.15	5.0	15 (14)	$1.4\cdot 10^{-3}$ (6)	LCC (5)	3 (18)
110411	ρ Vir	12 : 41 : 53.06	+10 : 14 : 08.3	A3V	38.16	4.88	0.09	-0.7	86 (1)	$6.4\cdot 10^{-5}$ (4)		1 (7)
118232	24 CVn	13 : 34 : 27.26	+49 : 00 : 57.5	A4V	55.28	4.7	0.12	-18.3	612 (1)	$2.6\cdot 10^{-5}$ (11)		6 (15)
121191	SAO 241295	13 : 55 : 18.86	−53 : 31 : 43.0	A5IV/V	132.11	8.16	0.24	12.0	16 (14)	$4.7\cdot 10^{-3}$ (16)	LCC/UCL (8)	3 (18)
121617	SAO 224570	13 : 57 : 41.13	−47 : 00 : 34.2	A1V	116.87	7.29	0.07	7.8	16 (14)	$4.8\cdot 10^{-3}$ (17)	UCL (9)	3 (18)
125162	*λ Böo*	14 : 16 : 23.02	+46 : 05 : 17.9	A3	30.36	4.18	0.08	7.9	313 (1)	$4.4\cdot 10^{-5}$ (4)		7 (12)
131488	SAO 225290	14 : 55 : 08.03	−41 : 07 : 13.4	A1V	154.62	8.0	0.09	5.8	16 (14)	$5.5\cdot 10^{-3}$ (16)	UCL (8)	3 (18)
131835	HIP 73145	14 : 56 : 54.47	−35 : 41 : 43.7	A2IV	133.65	7.86	0.19	0.5	16 (14)	$3.0\cdot 10^{-3}$ (18)	UCL (5)	3 (18)
138629	HR 5774	15 : 31 : 46.98	+40 : 53 : 57.6	A5V	127.20	4.98	0.96	-16.0	–			1 (19)
139006	α CrB	15 : 34 : 41.27	+26 : 42 : 52.9	A0V	23.01	2.24	-0.02	1.4	314 (1)	$1.5\cdot 10^{-5}$ (4)	UMA (1)	2 (9)
138813	HIP 76310	15 : 35 : 16.11	−25 : 44 : 03.0	A0V	137.41	7.3	0.07	4.4	10 (14)	$9.0\cdot 10^{-4}$ (6)	US (6)	3 (18)
142097	HIP 77815	15 : 53 : 21.93	−21 : 58 : 16.7	A5V	140.92	8.39	0.41	-0.1	11 (16)	<$3.0\cdot 10^{-4}$ (19)	US (6)	5 (20)
142315	HIP 77911	15 : 54 : 41.60	−22 : 45 : 58.5	B9V	145.34	6.87	0.034	-7.4	11 (1)	$3.8\cdot 10^{-4}$ (19)	US (6)	5 (20)
142705	HIP 78099	15 : 56 : 47.85	−23 : 11 : 02.7	A0V	144.33	7.74	0.18	-6.5	11 (16)	<$1.7\cdot 10^{-4}$ (19)	US (6)	5 (20)
144587	HIP 78996	16 : 07 : 29.93	−23 : 57 : 02.4	A9V	144.01	8.31	0.42	0.0	11 (1)	$3.2\cdot 10^{-4}$ (19)	US (6)	5 (20)
144981	HIP 79156	16 : 09 : 20.89	−19 : 27 : 25.9	A0V	150.59	8.04	0.18	-1.3	11 (1)	$1.2\cdot 10^{-4}$(19)	US (6)	5 (20)
145554	HIP 79410	16 : 12 : 21.83	−19 : 34 : 44.6	B9V	136.83	7.64	0.13	-9.4	11 (1)	$1.4\cdot 10^{-4}$ (19)	US (6)	5 (20)
145631	HIP 79439	16 : 12 : 44.10	−19 : 30 : 10.3	B9V	140.72	7.6	0.13	-9.5	11 (1)	$6.3\cdot 10^{-5}$ (19)	US (6)	5 (20)
145964	HR 6051	16 : 14 : 28.88	−21 : 06 : 27.5	B9V	112.18	6.41	0.001	-7.8	11 (1)	$1.5\cdot 10^{-5}$ (6)	US (6)	1 (7)
145689	HIP 79797	16 : 17 : 05.41	−67 : 56 : 28.6	A6V	55.55	5.95	0.148	-9.0	40 (1)	$4.9\cdot 10^{-5}$ (6)	Argus (1)	5 (21)
146606	HIP 79878	16 : 18 : 16.16	−28 : 02 : 30.2	A0V	137.27	7.06	-0.01	0.8	11 (1)	$9.5\cdot 10^{-5}$ (19)	US (6)	5 (20)
146624	d Sco	16 : 18 : 17.90	−28 : 36 : 50.5	A0V	41.29	4.79	0.03	-13.0	23 (2)	<$5.0\cdot 10^{-7}$ (2)	BPMG (3)	5 (2)
146897	HIP 79977	16 : 19 : 29.24	−21 : 24 : 13.3	F2/3V	131.50	9.11	0.47	-1.1	15 (16)	$5.6\cdot 10^{-3}$ (6)	US (6)	3 (21)
147137	HIP 80088	16 : 20 : 50.23	−22 : 35 : 38.8	A9V	143.92	9.03	0.39	-0.8	11 (1)	$5.7\cdot 10^{-4}$ (19)	US (6)	5 (20)
147220	HIP 80130	16 : 21 : 21.15	−22 : 06 : 32.3	A9V	158.88	8.59	0.45	-1.0	–	<$3.3\cdot 10^{-4}$ (19)	US (6)	5 (20)
148283	HR 6123	16 : 25 : 24.17	+37 : 23 : 38.7	A5V	77.45	5.54	0.17	-1.3	854 (8)	<$8.4\cdot 10^{-6}$ (11)		6 (11)
156623	HIP 84881	17 : 20 : 50.62	−45 : 25 : 15.0	A0V	111.75	7.26	0.09	-0.2	16 (14)	$7.8\cdot 10^{-3}$ (20)	UCL (5)	3 (21)
157728	73 Her	17 : 24 : 06.59	+22 : 57 : 37.0	A7V	42.75	5.72	0.21	-19.7	534 (1)	$2.9\cdot 10^{-4}$ (6)		2 (5)
158352	HR 6507	17 : 28 : 49.66	+00 : 19 : 50.3	A8Vp	63.46	5.41	0.23	-36.1	890 (1)	$9.3\cdot 10^{-5}$ (11)		2 (5)
162003	ψ 1 Dra A	17 : 41 : 56.35	+72 : 08 : 55.8	F5IV/V	21.42	4.56	0.44	-13.3	2326 (8)	<$4.4\cdot 10^{-6}$ (8)		4 (6)
162917	HR 6670	17 : 53 : 14.19	+06 : 06 : 05.1	F4IV/V	30.80	5.77	0.4	-29.1	1210 (1)	$6.5\cdot 10^{-5}$ (6)		2 (5)
164249	HIP 88399	18 : 03 : 03.41	−51 : 38 : 56.4	F6V+M2V	49.61	7.01	0.456	-0.4	23 (2)	$8.4\cdot 10^{-4}$ (2)	BPMG (3)	5 (2)
168646	HR 6864	18 : 22 : 00.14	−28 : 25 : 47.9	A3III	191.33	6.15	0.242	-11.5	662 (3)			6 (11)
172555	HR 7012	18 : 45 : 26.90	−64 : 52 : 16.5	A7V	28.55	4.78	0.191	2.0	23 (2)	$7.1\cdot 10^{-4}$ (4)	BPMG (3)	1 (22)
173667	110 Her	18 : 45 : 39.73	+20 : 32 : 46.7	F6V	19.21	4.19	0.46	23.05	2687 (8)	$7.0\cdot 10^{-7}$ (9)		4 (8)
177724	ζ Aql	19 : 05 : 24.61	+13 : 51 : 48.5	A0IV/Vn	25.46	2.99	0.01	-25.0	356 (1)	<$1.6\cdot 10^{-6}$		4 (8)
181296	η Tel	19 : 22 : 51.21	−54 : 25 : 26.1	A0V+M7V	48.22	5.02	0.015	13.0	23 (2)	$2.4\cdot 10^{-4}$ (6)	BPMG (3)	3 (2)
181327	HIP 95270	19 : 22 : 58.94	−54 : 32 : 17.0	F5/F6V	48.21	7.04	0.46	0.2	23 (2)	$2.0\cdot 10^{-3}$ (6)	BPMG (3)	3 (23)

Continued on next page

Table B.1 – continued from previous page

HD	Other Name	RA(2000.0)	Dec(2000.0)	Sp. Type	Distance (pc)	V (mag)	B-V (mag)	v_{rad} (km/s)	Age (Myr)	L_{IR} / $L_\star$	Assoc.	Sel.Crit
182640	δ Aql	19 : 25 : 29.90	+03 : 06 : 53.2	F1IV	15.53	3.36	0.32	-34.0	1385 (8)			4 (6)
182919	5 Vul	19 : 26 : 13.25	+20 : 05 : 51.8	A0V	71.98	5.59	0.002	-20.9	198 (1)	$3.4\cdot 10^{-5}$ (6)		1 (7)
183324	c Aql	19 : 29 : 00.99	+01 : 57 : 01.6	A0IV	60.68	5.79	0.083	12.0	140 (1)	$1.8\cdot 10^{-5}$ (5)		1 (7)
187642	α Aql	19 : 50 : 47.00	+08 : 52 : 06.0	A7V	5.13	0.76	0.22	-26.6	991 (8)	$<4.4\cdot 10^{-6}$ (4)		4 (8)
188228	ϵ Pav	20 : 00 : 35.56	−72 : 54 : 37.8	A0V	32.22	3.95	-0.006	-6.7	40 (1)	$4.4\cdot 10^{-6}$ (4)	Argus (7)	2 (9)
192518	HR 7731	20 : 14 : 14.53	+28 : 41 : 41.3	A5IV	93.37	5.2	0.17	7.0	607 (8)			6 (11)
196724	29 Vul	20 : 38 : 31.34	+21 : 12 : 04.3	A0	64.00	4.82	-0.02	-17.1	224 (8)	$<2.4\cdot 10^{-6}$ (11)		6 (15)
198160	HR 7959	20 : 51 : 38.47	−62 : 25 : 45.6	A2III	74.00	6.21	0.14	-16.0	735 (8)	$2.0\cdot 10^{-5}$ (5)		7 (12)
198161	HR 7960	20 : 51 : 38.76	−62 : 25 : 44.9	A3III	73.90	6.56	0.18	-10.0	735 (8)			7 (12)
199143	HIP 103311	20 : 55 : 47.67	−17 : 06 : 51.0	F8V	45.66	7.32	0.52	-4.5	23 (2)	$<2.6\cdot 10^{-6}$ (2)	BPMG	5 (2)
203280	α Cep	21 : 18 : 34.77	+62 : 35 : 08.1	A8V	15.04	2.46	0.22	-15.8	987 (8)	$<2.1\cdot 10^{-6}$ (24)		4 (8)
202917	HIP 105388	21 : 20 : 49.96	−53 : 02 : 03.1	G7V	46.85	8.67	0.65	-0.9	45 (9)	$2.5\cdot 10^{-4}$ (1)	Tuc-Hor (4)	5 (1)
210302	τ PsA	22 : 10 : 08.78	−32 : 32 : 54.3	F6V	18.35	4.92	0.48	-16.25	3530 (7)	$<4.4\cdot 10^{-6}$ (8)		4 (4)
210418	θ Peg	22 : 10 : 11.99	+06 : 11 : 52.3	A1V	28.30	3.55	0.07	-7.9	545 (8)	$<4.4\cdot 10^{-6}$ (4)		4 (6)
211336	ϵ Cep	22 : 15 : 02.20	+57 : 02 : 36.9	F0IV	26.30	4.19	0.28	-4.7	1063 (1)	$1.9\cdot 10^{-5}$ (6)		4 (8)
213617	39 Peg	22 : 32 : 35.48	+20 : 13 : 48.1	F1V	53.58	6.44	0.33	-18.9	930 (1)	$6.5\cdot 10^{-5}$ (6)		2 (5)
217782	2 And	23 : 02 : 36.38	+42 : 45 : 28.1	A3V	129.20	5.1	0.08	2.1	478 (3)	$<9.6\cdot 10^{-6}$ (11)		1 (7)
221756	15 And	23 : 34 : 37.54	+40 : 14 : 11.2	A1V	77.28	5.56	0.089	13.1	613 (8)	$1.5\cdot 10^{-5}$ (5)		7 (12)
222368	ι Psc	23 : 39 : 57.04	+05 : 37 : 34.6	F7V	13.71	4.12	0.5	5.67	3287 (3)	$1.1\cdot 10^{-6}$ (8)		4 (6)
224392	η Tuc	23 : 57 : 35.08	−64 : 17 : 53.6	A1V	47.07	5.0	0.056	32.5	45 (9)	$<1.6\cdot 10^{-5}$ (1)	Tuc-Hor (4)	5 (1)

References for age: (1) Chen et al. (2014); (2) Mamajek & Bell (2014); (3) Gontcharov (2012); (4) Gáspár et al. (2013); (5) Torres et al. (2008); (6) Maldonado et al. (2012); (7) Eiroa et al. (2013); (8) David & Hillenbrand (2015); (9) Bell et al. (2015); (10) Kalas (2005); (11) Lisse et al. (2017); (12) Su et al. (2006); (13) Marino et al. (2017); (14) Pecaut & Mamajek (2016); (15) Bochanski et al. (2018); (16) Pecaut et al. (2012); (17) Roberge & Weinberger (2008)
References for $L_{IR}/L_\star$: (1) Donaldson et al. (2012); (2) Riviere-Marichalar et al. (2014); (3) Redfield et al. (2007) ; (4) Thureau et al. (2014); (5) Draper et al. (2016); (6) Chen et al. (2014); (7) Moór et al. (2015b); (8) Sibthorpe et al. (2018); (9) Eiroa et al. (2013); (10) Moór et al. (2011b); (11) Roberge & Weinberger (2008); (12) Lisse et al. (2017); (13) Currie et al. (2011)5; (14) Duchêne et al. (2014); (15) Riviere-Marichalar et al. (2013); (16) Vican et al. (2016); (17) Moór et al. (2011a); (18) Moór et al. (2015a); (19) Donaldson et al., private communication; (20) Cotten & Song (2016); (21) Plavchan et al. (2009); (22) Cataldi et al. (2019)
References for associations: (1) Chen et al. (2014); (2) Zuckerman & Song (2012); (3) Riviere-Marichalar et al. (2013); (4) Donaldson et al. (2012);(5) Lieman-Sifry et al. (2016); (6) de Zeeuw et al. (1999);(7) Zuckerman (2019); (8) Desidera et al. (2015)
References for selection criteria: (1) Donaldson et al. (2012); (2) Riviere-Marichalar et al. (2014); (3) Redfield et al. (2007) ; (4) Ertel et al. (2014); (5) Chen et al. (2014); (6) Nuñez et al. (2017); (7) Welsh & Montgomery (2013); (8) Absil et al. (2013); (9) Pawellek et al. (2014); (10) Moór et al. (2011a); (11) Abt (2008); (12) Draper et al. (2016); (13) Redfield (2007); (14) Currie et al. (2017); (15) Roberge & Weinberger (2008); (16) Welsh & Montgomery (2015); (17) Marino et al. (2017); (18) Moór et al. (2017); (19) Lagrange-Henri et al. (1990b); (20) Donaldson et al., private communication; (21) Lieman-Sifry et al. (2016); (22) Kiefer et al. (2014a); (23) Marino et al. (2016); (24) Chen et al. (2005)

Table B.2: Stellar Parameters estimated according to Sect. 3.2.

HD	RA(2000.0)	Dec(2000.0)	Sp. Type	v_{rad} (km/s)	T_{eff} (K)	log g [cgs]	[M/H]	$v \sin i$ (km/s)
105	00 : 05 : 52.54	−41 : 45 : 11.0	G0V	+1.6 ± 0.4	6000±60	4.38±0.14	−0.03	14.6
203	00 : 06 : 50.09	−23 : 06 : 27.1	F3V	+7.1 ± 1.7	6850±200	4.25±0.30	0.00	170
256	00 : 07 : 18.27	−17 : 23 : 13.2	A2IV/V	−2.2 ± 0.3	8690±50	3.48±0.20	0.00	270
1466	00 : 18 : 26.12	−63 : 28 : 39.0	F8V	+6.4 ± 0.4	6270±60	4.45±0.15	−0.01	18
2262	00 : 26 : 12.20	−43 : 40 : 47.4	A5IV	+11.3 ± 3.7	8110±30	4.01±0.13	0.00	200
2884	00 : 31 : 32.67	−62 : 57 : 29.6	B9V	+8.3 ± 1.6	11620±30	4.45±0.10	−0.05	135
2885	00 : 31 : 33.48	−62 : 57 : 56.0	A2V	+13.5 ± 3.9	9630±30	4.27±0.10	+0.20	40
3003	00 : 32 : 43.91	−63 : 01 : 53.4	A0V	+8.2 ± 2.3	9490±50	4.35±0.14	0.00	95
5267	00 : 54 : 35.23	+19 : 11 : 18.3	A1V	+9.5 ± 1.8	10450±50	4.16±0.10	0.00	144
5448	00 : 56 : 45.21	+38 : 29 : 57.6	A5V	+6.4 ± 0.6	8590±70	3.18±0.10	+0.20	65
7788	01 : 15 : 46.16	−68 : 52 : 33.3	F6V+K1V	+12.4 ± 3.3	6550±200	4.30±0.10	0.00	70
9672	01 : 34 : 37.78	−15 : 40 : 34.9	A1V	+10.9 ± 2.5	9120±50	4.32±0.16	0.00	186
10700	01 : 44 : 04.08	−15 : 56 : 14.9	G8.5V	−16.8 ± 0.1	5330±10	4.55±0.10	−0.51	1.6
12039	01 : 57 : 48.98	−21 : 54 : 05.3	G4V	+5.8 ± 0.4	5700±40	4.31±0.10	−0.06	15.9
14055	02 : 17 : 18.87	+33 : 50 : 49.9	A1V	+7.3 ± 0.2	10040±50	4.34±0.10	0.00	254
14412	02 : 18 : 58.50	−25 : 56 : 44.5	G8V	+7.3 ± 0.2	5310±20	4.55±0.10	−0.53	0.90
15115	02 : 26 : 16.24	+06 : 17 : 33.2	F2V	+6.0 ± 2.7	6750±200	4.25±0.30	0.00	89.8
15257	02 : 28 : 09.98	+29 : 40 : 09.6	F0III	−20.6 ± 0.2	7100±200	3.50±0.30	0.00	65
16978	02 : 39 : 35.36	−68 : 16 : 01.0	B9III	−24.8 ± 0.8	11330±100	4.43±0.11	0.00	96
21688	03 : 29 : 36.03	−12 : 40 : 29.1	A5III/IV	+15.2 ± 0.1	7880±90	4.52±0.30	0.00	180
21620	03 : 31 : 29.34	+49 : 12 : 35.2	A0V	−13.9 ± 0.3	9650±50	3.90±0.10	0.00	260
21997	03 : 31 : 53.65	−25 : 36 : 50.9	A3IV/V	+19.0 ± 1.5	8520±140	4.27±0.31	0.00	60
22484	03 : 36 : 52.38	+00 : 24 : 06.0	F8V	+27.9 ± 0.1	5960±30	3.93±0.10	−0.09	4
27290	04 : 16 : 01.59	−51 : 29 : 11.9	F1V	+26.7 ± 1.6	7300±200	4.25±0.25	0.00	60
28355	04 : 28 : 50.16	+13 : 02 : 51.4	A7V	+39.8 ± 0.3	8730±50	3.53±0.30	+0.50	105
29391	04 : 37 : 36.13	−02 : 28 : 24.8	F0IV	+20.4 ± 3.8	7200±100	4.25±0.25	0.00	84
30051	04 : 43 : 17.20	−23 : 37 : 42.0	F2V	+15.9 ± 5.6	6900±200	4.25±0.25	0.00	50
31295	04 : 54 : 53.73	+10 : 09 : 03.0	A3V	+16.0 ± 0.2	9130±80	4.25±0.26	−1.00	120
32297	05 : 02 : 27.44	+07 : 27 : 39.7	A0V	+21.0 ± 0.9	7980±100	3.77±0.30	−0.50	90
35850	05 : 27 : 04.76	−11 : 54 : 03.5	F8V	+21.1 ± 3.3	6400±200	4.25±0.25	0.00	50
36546	05 : 33 : 30.76	+24 : 37 : 43.7	B8V	+14.7 ± 0.6	9510±50	4.44±0.10	−1.00	150
37286	05 : 36 : 10.30	−28 : 42 : 28.8	A2IV	+24.9 ± 2.9	8640±50	4.11±0.12	0.00	70
37306	05 : 37 : 08.77	−11 : 46 : 31.9	A2V	+25.1 ± 1.3	9600±50	4.48±0.10	0.00	144
38206	05 : 43 : 21.67	−18 : 33 : 26.9	A0V	+26.6 ± 2.3	10480±100	4.50±0.10	0.00	35
39182	05 : 52 : 39.67	+39 : 34 : 28.9	A2V	−22.9 ± 1.0	9020±80	3.42±0.30	+0.20	238
39283	05 : 54 : 50.78	+55 : 42 : 25.0	A2V	−18.3 ± 0.6	9140±40	3.91±0.15	−0.25	68
40136	05 : 56 : 24.29	−14 : 10 : 03.7	F2V	+1.6 ± 0.8	7150±200	4.25±0.25	0.00	18
42111	06 : 08 : 57.90	+02 : 29 : 58.9	A3V	+27.5 ± 1.9	9380±40	3.48±0.10	0.00	252
53842	06 : 46 : 13.54	−83 : 59 : 29.5	F5V	+17.0 ± 0.5	6500±200	4.25±0.25	0.00	50
50241	06 : 48 : 11.46	−61 : 56 : 29.0	A8V	+13.0 ± 2.9	7580±90	3.52±0.30	−0.25	206
50571	06 : 50 : 01.01	−60 : 14 : 56.9	F5V	+26.2 ± 3.1	6450±100	4.25±0.25	0.00	50
56537	07 : 18 : 05.58	+16 : 32 : 25.4	A4IV	−9.6 ± 2.7	8190±100	4.10±0.39	0.00	154
64145	07 : 53 : 29.81	+26 : 45 : 56.8	A5IV	+4.2 ± 3.2	8320±50	3.48±0.10	0.00	165
71043	08 : 22 : 55.16	−52 : 07 : 25.4	A0V	+24.1 ± 2.2	10280±50	4.51±0.10	0.00	224
71722	08 : 26 : 25.21	−52 : 48 : 27.0	A0V	+31.0 ± 2.6	8870±50	4.19±0.12	−1.00	220
74873	08 : 46 : 56.02	+12 : 06 : 35.8	A1VP	+23.0 ± 0.2	8800±70	4.02±0.37	−1.00	115
77190	09 : 01 : 48.84	+27 : 54 : 09.3	A8Vn	+14.5 ± 3.1	8010±120	3.41±0.30	0.00	185
80007	09 : 13 : 11.98	−69 : 43 : 01.9	A1III	+0.8 ± 1.8	9350±40	3.47±0.10	0.00	135
85905	09 : 54 : 31.82	−22 : 29 : 14.9	A1IV	+9.9 ± 2.5	9040±40	3.50±0.10	0.00	285
95418	11 : 01 : 50.48	+56 : 22 : 56.7	A1IV	−12.2 ± 0.6	9700±40	4.01±0.19	0.00	46
98058	11 : 16 : 39.70	−03 : 39 : 05.8	A7IV	−0.3 ± 0.8	7500±50	3.75±0.32	0.00	230
102647	11 : 49 : 03.58	+14 : 34 : 19.4	A3Va	−0.4 ± 3.5	8580±50	4.14±0.32	0.00	128
104731	12 : 03 : 39.57	−42 : 26 : 02.6	F5V	+38.5 ± 0.4	6510±70	3.87±0.10	−0.25	7
104860	12 : 04 : 33.73	+66 : 20 : 11.7	F8	−11.9 ± 0.4	6060±70	4.48±0.14	−0.01	15
105234	12 : 07 : 05.52	−78 : 44 : 28.0	A9III/4	+15.3 ± 1.9	8590±50	4.40±0.10	+0.50	85
105850	12 : 11 : 03.84	−23 : 36 : 08.7	A1V	+15.0 ± 3.6	9160±50	4.21±0.13	0.00	128
108767	12 : 29 : 51.86	−16 : 30 : 55.6	A0IV	+8.5 ± 1.1	10850±50	4.35±0.10	0.00	236
109085	12 : 32 : 04.23	−16 : 11 : 45.6	F2V	+0.0 ± 0.5	6950±100	4.20±0.25	0.00	60
109573	12 : 36 : 01.03	−39 : 52 : 10.2	A0V	+7.5 ± 2.0	10060±50	4.44±0.10	−0.50	150
110058	12 : 39 : 46.20	−49 : 11 : 55.5	A0V	10.6 ± 2.6	9000±50	4.13±0.15	−0.50	150
110411	12 : 41 : 53.06	+10 : 14 : 08.3	A3V	−7.9 ± 1.1	9240±50	4.29±0.10	−1.00	154
118232	13 : 34 : 27.26	+49 : 00 : 57.5	A4V	−16.9 ± 0.4	8130±40	3.49±0.10	0.00	160
121191	13 : 55 : 18.86	−53 : 31 : 43.0	A5IV/V	21.5 ± 1.0	7970±90	4.38±0.10	0.00	65
121617	13 : 57 : 41.13	−47 : 00 : 34.2	A1V	+7.0 ± 3.7	9160±70	4.13±0.36	0.00	90
125162	14 : 16 : 23.02	+46 : 05 : 17.9	A3	−10.1 ± 1.5	8660±50	3.96±0.23	−2.00	100
131488	14 : 55 : 08.03	−41 : 07 : 13.4	A1V	+4.8 ± 0.2	9130±60	4.18±0.22	0.00	120
131835	14 : 56 : 54.47	−35 : 41 : 43.7	A2IV	+2.7 ± 2.5	8610±40	4.24±0.18	0.00	105
138629	15 : 31 : 46.98	+40 : 53 : 57.6	A5V	−18.7 ± 1.1	8680±40	3.54±0.10	+0.20	190
139006	15 : 34 : 41.27	+26 : 42 : 52.9	A0V	+9.9 ± 01	9780±40	3.91±0.10	0.00	130
138813	15 : 35 : 16.11	−25 : 44 : 03.0	A0V	+0.3 ± 2.1	9620±50	4.30±0.11	0.00	130
142097	15 : 53 : 21.93	−21 : 58 : 16.7	A5V	−7.0 ± 2.0	8290±70	3.67±0.10	+0.20	45
142315	15 : 54 : 41.60	−22 : 45 : 58.5	B9V	−4.0 ± 2.4	12500±250	4.50±0.25	0.00	275
142705	15 : 56 : 47.85	−23 : 11 : 02.7	A0V	−5.6 ± 3.0	9300±50	3.97±0.11	0.00	300

Continued on next page

Table B.2 – continued from previous page

HD	RA(2000.0)	Dec(2000.0)	Sp. Type	v_{rad} (km/s)	T_{eff} (K)	log g [cgs]	[M/H]	$v \sin i$ (km/s)
144587	16 : 07 : 29.93	−23 : 57 : 02.4	A9V	−10.7 ± 4.7	7390±250	4.50±0.30	0.00	112
144981	16 : 09 : 20.89	−19 : 27 : 25.9	A0V	−5.6 ± 4.3	9950±100	4.32±0.22	0.00	215
145554	16 : 12 : 21.83	−19 : 34 : 44.6	B9V	−7.8 ± 3.9	12030±40	4.44±0.10	0.00	260
145631	16 : 12 : 44.10	−19 : 30 : 10.3	B9V	−5.7 ± 2.3	11410±80	4.36±0.10	0.00	287
145964	16 : 14 : 28.88	−21 : 06 : 27.5	B9V	−6.8 ± 3.1	12080±90	4.47±0.13	0.00	306
145689	16 : 17 : 05.41	−67 : 56 : 28.6	A6V	−7.1 ± 1.7	8340±50	4.04±0.10	0.00	105
146606	16 : 18 : 16.16	−28 : 02 : 30.2	A0V	−2.3 ± 1.3	10540±50	4.39±0.10	0.00	165
146624	16 : 18 : 17.90	−28 : 36 : 50.5	A0V	−14.0 ± 1.9	9880±40	4.50±0.10	0.00	34
146897	16 : 19 : 29.24	−21 : 24 : 13.3	F2/3V	−3.1 ± 0.9	6700±200	4.30±0.30	0.00	55
147137	16 : 20 : 50.23	−22 : 35 : 38.8	A9V	−6.6 ± 1.9	7670±40	4.49±0.10	0.00	82
147220	16 : 21 : 21.15	−22 : 06 : 32.3	A9V	−49.3 ± 2.0	7560±80	4.12±0.10	0.00	80
148283	16 : 25 : 24.17	+37 : 23 : 38.7	A5V	−0.5 ± 0.2	8380±40	4.46±0.30	0.00	240
156623	17 : 20 : 50.62	−45 : 25 : 15.0	A0V	−0.2 ± 2.1	9430±80	4.48±0.20	−0.30	75
157728	17 : 24 : 06.59	+22 : 57 : 37.0	A7V	−21.2 ± 0.3	7690±46	3.98±0.10	0.00	60
158352	17 : 28 : 49.66	+00 : 19 : 50.3	A8Vp	−33.9 ± 0.6	7470±140	3.98±0.21	0.00	150
162003	17 : 41 : 56.35	+72 : 08 : 55.8	F5IV/V	−13.3 ± 0.2	6370±50	3.62±0.10	−0.15	13
162917	17 : 53 : 14.19	+06 : 06 : 05.1	F4IV/V	−29.1 ± 0.9	6620±220	4.28±0.14	0.00	28.4
164249	18 : 03 : 03.41	−51 : 38 : 56.4	F6V+M2V	−0.4 ± 0.5	6570±90	4.03±0.13	+0.02	21
168646	18 : 22 : 00.14	−28 : 25 : 47.9	A3III	−10.8 ± 2.6	8750±100	3.00±0.30	0.00	260
172555	18 : 45 : 26.90	−64 : 52 : 16.5	A7V	+1.2 ± 2.9	7994±60	4.23±0.10	0.00	107
173667	18 : 45 : 39.73	+20 : 32 : 46.7	F6V	22.7 ± 0.1	6380±80	3.67±0.12	−0.10	18
177724	19 : 05 : 24.61	+13 : 51 : 48.5	A0IV/Vn	−27.3 ± 2.5	10260±50	4.26±0.10	−0.15	290
181296	19 : 22 : 51.21	−54 : 25 : 26.1	A0V+M7V	−0.3 ± 1.9	10500±170	4.57±0.30	0.00	230
181327	19 : 22 : 58.94	−54 : 32 : 17.0	F5/F6V	+0.1 ± 0.4	6360±60	4.09±0.10	−0.05	28
182640	19 : 25 : 29.90	+03 : 06 : 53.2	F1IV	−37.2 ± 1.8	7000±200	4.25±0.30	0.00	91
182919	19 : 26 : 13.25	+20 : 05 : 51.8	A0V	−24.3 ± 1.4	10460±80	4.47±0.10	0.00	154
183324	19 : 29 : 00.99	+01 : 57 : 01.6	A0IV	17.4 ± 0.4	9830±40	4.50±0.10	−1.00	100
187642	19 : 50 : 47.00	+08 : 52 : 06.0	A7V	−27.2 ± 0.4	7930±40	4.21±0.10	0.00	205
188228	20 : 00 : 35.56	−72 : 54 : 37.8	A0V	−6.0 ± 3.5	10620±50	4.47±0.10	0.00	85
192518	20 : 14 : 14.53	+28 : 41 : 41.3	A5IV	+8.1 ± 0.3	8020±40	4.61±0.10	0.00	220
196724	20 : 38 : 31.34	+21 : 12 : 04.3	A0	−10.8 ± 2.4	10820±80	4.35±0.12	0.00	52
198160	20 : 51 : 38.47	−62 : 25 : 45.6	A2III	−16.2 ± 1.9	8300±40	4.15±0.30	−0.50	200
198161	20 : 51 : 38.76	−62 : 25 : 44.9	A3III	−13.5 ± 3.6	8160±40	3.79±0.30	−0.50	180
199143	20 : 55 : 47.67	−17 : 06 : 51.0	F8V	−4.5 ± 2.1	6200±150	4.25±0.30	0.00	155
203280	21 : 18 : 34.77	+62 : 35 : 08.1	A8V	−11.8 ± 1.1	7800±100	3.72±0.26	0.00	210
202917	21 : 20 : 49.96	−53 : 02 : 03.1	G7V	+0.1 ± 0.2	5520±60	4.42±0.14	−0.04	14
210302	22 : 10 : 08.78	−32 : 32 : 54.3	F6V	−16.4 ± 0.2	6460±100	4.17±0.17	+0.18	13.6
210418	22 : 10 : 11.99	+06 : 11 : 52.3	A1V	−5.1 ± 0.8	8820±60	4.18±0.18	−0.25	140
211336	22 : 15 : 02.20	+57 : 02 : 36.9	F0IV	−5.5 ± 0.5	7400±200	4.25±0.30	0.20	91
213617	22 : 32 : 35.48	+20 : 13 : 48.1	F1V	−13.1 ± 0.7	7200±200	4.25±0.30	0.00	94
217782	23 : 02 : 36.38	+42 : 45 : 28.1	A3V	+5.1 ± 1.1	8830±40	3.45±0.10	0.00	212
221756	23 : 34 : 37.54	+40 : 14 : 11.2	A1V	13.5 ± 0.3	9050±60	4.11±0.20	−0.50	100
222368	23 : 39 : 57.04	+05 : 37 : 34.6	F7V	+5.6 ± 0.1	6130±40	3.90±0.10	−0.16	6.8
224392	23 : 57 : 35.08	−64 : 17 : 53.6	A1V	+9.9 ± 2.3	9400±40	4.25±0.10	+0.10	195

Table B.3: Plausible origin of the observed narrow non-photospheric absorptions for each star. Equivalent widths (EW), radial velocities (RV), full width half maximum (FWHM), and column densities (N) are given for each absorption as estimated from the median spectra. Uncertainty estimates of these parameters are detailed in Sect. 4.1. as follows: 10% for EW; 2.5 and 1.5 km/s for RV and FWHM in the Ca and Na regime respectively; and propagated errors of those values for N (approx. ∼ 10%). Radial velocities of the stars (v_{rad}) and the radial velocity of the interstellar clouds (v_{ISM}), if present, are also given. The convention for the plausible origin is the following. CS: circumstellar; ISM: interstellar medium; CS+ISM: both types origins are plausible. A question mark indicates that the origin is ambiguous. Absorptions marked with an asterisk (*) in the EW are triangular shell-like absorptions.

Star	V_{rad}	V_{ISM}	Ca II K/H				Na I D2/D1				Origin
			EW	RV	FWHM	N	EW	RV	FWHM	N	
	(km/s)	(km/s)	(mÅ)	(km/s)	(km/s)	(cm^{-2})	(mÅ)	(km/s)	(km/s)	(cm^{-2})	
HD 256	-2.2±0.3	3.16 (LIC)	190.9*/180.3*	-1.8/-0.82	10.67/11.05	$4.88\cdot 10^{12}$	1.2/0.4	3.2/3.3	4.17/1.80	$5.91\cdot 10^{9}$	CS
		-2.73 (Mic)									
		1.01 (Cet)									
HD 2884	8.3±1.6	13.85 (Dor)	2.1/1.66	0.5/4.3	12.13/7.1	$4.28\cdot 10^{10}$					?
		2.46 (Vel)									
HD 2885	13.5±3.9	13.84 (Dor)					56.8/52.3	-2.0/-2.5	17.68/16.1	$1.85\cdot 10^{12}$	?
		2.46 (Vel)									
HD 3003	8.2±2.3	13.84 (Dor)	4.5/<1.5	0.6/-	24.55/-	$4.82\cdot 10^{10}$	4.8/2.9	-3.7/-3.0	6.84/6.57	$4.61\cdot 10^{10}$	?
		2.46 (Vel)									
HD 5267	9.5±1.8	11.44 (LIC)	11.4/5.1	-5.0/-5.1	6.86/5.47	$1.22\cdot 10^{11}$	34.8/20.0	-5.4/-5.3	6.00/5.80	$3.79\cdot 10^{11}$	?
			2.6/<1.0	9.7/-	10.64/-	$2.78\cdot 10^{10}$	1.2/<1.0	11.7/-	12.8/-	$1.53\cdot 10^{10}$	
HD 9672	10.9±2.5	11.01 (LIC)	10.6/6.0	13.5/12.9	7.4/7.1	$1.83\cdot 10^{11}$	16.4/9.3	11.5/10.6	4.4/4.0	$3.21\cdot 10^{11}$	CS+ISM
HD 16978	12.9±1.8	2.65 (G)	4.9/1.6	11.6/10.8	10.57/7.98	$5.24\cdot 10^{10}$					CS
		5.19 (Cet)									
		8.66 (Vel)									
HD 21688	15.2±0.1	18.71 (LIC)	123.9*/99.84	15.7/17.9	13.92/13.45	$2.61\cdot 10^{12}$					CS
HD 21620	-13.9±0.3	18.52 (LIC)	12.4/6.7	4.0/3.9	5.67/5.50	$3.65\cdot 10^{11}$	73.5/54.9	3.7/3.8	5.11/4.87	$6.55\cdot 10^{11}$	CS+ISM
			2.0/1.9	15.3/15.3	7.60/6.63	$2.12\cdot 10^{11}$					
HD 32297	21.0±0.9	23.59 (LIC)	19.4/9.8	22.7/21.9	9.7/6.9	$2.08\cdot 10^{11}$	93.0/84.0	19.7/20.8	6.69/6.23	$1.05\cdot 10^{12}$	CS
HD 36546	14.7±0.6	23.53 (LIC)	18.7/14.5	14.6/15.0	4.43/5.04	$3.74\cdot 10^{11}$	24.3/13.9	14.1/14.33	4.01/4.02	$2.56\cdot 10^{11}$	CS
			10.9/4.0	18.7/20.8	7.40/8.67	$1.28\cdot 10^{11}$	12.9/6.8	18.6/18.5	6.04/6.49	$2.05\cdot 10^{10}$	
HD 37306	25.1±1.3		13.1/6.3	11.0/10.6	6.91/6.75	$1.40\cdot 10^{11}$	4.6/2.23	10.6/10.7	6.41/5.22	$2.27\cdot 10^{10}$	CS+ISM
			31.6/19.3	32.3/32.5	8.71/9.39	$3.38\cdot 10^{11}$	6.7/3.17	31.2/31.6	7.95/8.08	$3.30\cdot 10^{10}$	
HD 39182	-22.9±1.0	21.62 (LIC)	19.6/14.5	13.3/13.3	6.70/8.81	$3.81\cdot 10^{11}$	131.8/102.5	13.8/13.7	7.83/6.8	$1.21\cdot 10^{12}$	CS
			6.9/<3.0	-21.8/-	5.92/-	$7.28\cdot 10^{10}$					
			103.1*/67.1	-22.6/-18.3	55.43/36.49	$1.92\cdot 10^{12}$					
HD 42111	27.5±1.9	24.83 (Aur)	318.3*/285.9	27.2/29.3	25.93/26.86	$9.66\cdot 10^{12}$	61.8/43.5	23.2/23.5	5.23/5.14	$5.40\cdot 10^{11}$	CS+ISM
							113.7/55.9	27.0/27.8	58.67/52.84	$5.60\cdot 10^{11}$	
HD 50241	13.0±2.9	6.81 (Blue)	8.4/4.0	15.6/16.8	16.25/8.92	$9.35\cdot 10^{10}$					CS
		17.9 (Cet)									
		15.34 (Vel)									
HD 71043	24.1±2.2	4.62 (G)	2.5/<1.5	16.0/-	10.35/-	$2.68\cdot 10^{10}$	1.9/0.99	17.5/17.3	5.66/5.47	$4.33\cdot 10^{10}$	ISM
		20.5 (Cet)	2.5/1.9	4.5/5.4	8.28/7.10	$5.01\cdot 10^{10}$	2.9/0.88	5.3/5.1	10.47/5.88	$1.43\cdot 10^{10}$	
		15.0 (Vel)									
HD 71722	31.0±2.6	4.19 (G)	7.9/3.2	11.8/11.0	16.49/16.45	$8.46\cdot 10^{10}$	4.5/4.1	13.6/14.1	7.55/12.01	$9.56\cdot 10^{10}$	ISM
		19.65 (Cet)									
		14.33 (Vel)									
HD 80007	0.8±1.8	-2.75 (G)	1.5/<1.0	1.3/-	8.2/-	$1.51\cdot 10^{10}$	2.7/<1.0	3.0/-	12.57/-	$1.33\cdot 10^{10}$	CS

Continued on next page

Table B.3 – continued from previous page

Star	V_{rad}	V_{ISM}	Ca II K/H				Na I D2/D1				Origin
			EW	RV	FWHM	N	EW	RV	FWHM	N	
	(km/s)	(km/s)	(mÅ)	(km/s)	(km/s)	(cm^{-2})	(mÅ)	(km/s)	(km/s)	(cm^{-2})	
		3.35 (Blue)					1.4/<1.0	-11.6/-	7.04/-	$6.90\cdot 10^{9}$	
HD 85905	9.9±2.5	11.01 (G)	80.5*/75.3	16.2/18.5	58.25/56.35	$4.29\cdot 10^{12}$	6.3/2.9	11.6/10.3	29.08/17.56	$3.10\cdot 10^{10}$	CS+ISM
			7.6/3.56	8.1/7.7	6.22/4.49	$8.13\cdot 10^{10}$	13.4/6.5	7.9/8.1	5.52/5.23	$6.60\cdot 10^{10}$	
			1.2/<1.0	25.5/-	5.20/-	$1.28\cdot 10^{10}$					
HD 98058	0.7±1.5	1.75 (Leo)	124.9*/94.4	-7.8/8.9	48.81/50.29	$2.44\cdot 10^{12}$					CS
HD 105850	15.0±3.6	2.54 (Gem)	15.3/4.6	-4.6/-5.1	10.35/7.19	$1.64\cdot 10^{11}$	10.4/4.8	-6.5/-6.6	6.41/5.52	$5.12\cdot 10^{10}$	ISM
		-5.36 (Leo)									
HD 108767	8.5±1.1	0.21 (Gem)	3.4/1.6	-0.6/-0.8	5.59/6.19	$3.64\cdot 10^{10}$	2.9/1.2	-0.3/0.2	4.80/4-48	$1.43\cdot 10^{10}$	ISM
HD 109573	7.5±2.0		2.1/<1.0	-14.2/-	8.05/-	$2.25\cdot 10^{10}$	8.3/3.8	-5.4/-4.8	8.49/7.38	$4.09\cdot 10^{10}$	CS
			2.3/1.1	-4.7/-6.0	7.80/6.62	$2.46\cdot 10^{10}$					
HD 110058	10.6±2.6	-14.46 (G)	27.0/24.1	12.7/12.0	6.8/6.22	$5.41\cdot 10^{11}$	46.0/39.1	12.5/12.4	6.31/6.57	$1.98\cdot 10^{12}$	CS
			19.9/10.0	1.2/1.8	12.6/13.4	$1.21\cdot 10^{14}$	34.0/18.9	0.9/0.6	11.71/11.5	$1.67\cdot 10^{11}$	
HD 118232	-16.9±0.4	-1.87 (NGP)	10.6/4.3	-6.7/-6.4	6.92/5.64	$1.13\cdot 10^{11}$	3.9/1.9	-6.7/-5.9	6.19/584	$1.92\cdot 10^{10}$	ISM
HD 125162	-10.1±1.5	-6.64 (NGP)					1.9/<1.0	17.8/-	3.41/-	$9.36\cdot 10^{9}$	ISM
HD 131488	4.8±0.2	-23.91 (G)	23.0/8.7	-0.8/2.5	21.09/12.1	$2.46\cdot 10^{11}$	33.5/30.1	5.4/5.7	6.18/6.03	$4.83\cdot 10^{11}$	CS
							7.3/<5.0	-13.8/-	8.94/-	$8.23\cdot 10^{10}$	
HD 131835	2.7±2.5	18.56 (Gem)	8.3/4.1	-14.5/-13.8	7.40/7.50	$8.88\cdot 10^{10}$	41.0/32.0	-11.8/-12.4	11.52/11.73	$4.34\cdot 10^{11}$	?
		-27.63 (NGP)	2.1/1.4	-5.9/-4.8	7.91/7.68	$2.25\cdot 10^{10}$					
			0.7/<0.1	2.2/-	2.3/-	$7.49\cdot 10^{9}$					
HD 138629	-18.7±1.1	-18.29 (NGP)	47.5/36.5	-13.8/-13.9	5.41/5.05	$9.39\cdot 10^{11}$	14.7/5.8	-11.9/-11.3	4.95/4.22	$7.24\cdot 10^{10}$	CS+ISM
			53.4/32.8	-22.9/-22.8	8.20/7.77	$1.07\cdot 10^{12}$	83.7/72.0	-21.6/-21.3	5.21/4.94	$9.16\cdot 10^{11}$	
			105.8/84.8	-31.8/-31.8	8.71/8.29	$2.18\cdot 10^{12}$	30.2/26.5	-16.7/-16.5	4.18/4.54	$3.25\cdot 10^{11}$	
HD 138813	0.3±2.1	-27.82 (G)	5.6/1.4	-27.5/-27.8	18.70/6.87	$5.99\cdot 10^{10}$	5.9/3.2	-22.2/-21.7	11.62	$6.92\cdot 10^{10}$	ISM
		-24.16 (Gem)					20.1/11.1	-12.1/-11.8	5.28	$2.36\cdot 10^{11}$	
							-7.55/-5.2	0.2/0.6	10.04	$6.59\cdot 10^{10}$	
HD 142097	-7.0±2.0	-28.67 (G)	24.2/14.0	-16.8/-15.4	8.41/8.50	$5.32\cdot 10^{11}$	263.9/231.9	-16.7/-16.4	12.83/12.11	$3.11\cdot 10^{12}$	ISM
							82.9/59.8	-7.5/-6.8	6.78/6.20	$7.32\cdot 10^{11}$	
HD 142315	-4.0±2.4	-28.64 (G)	35.1/18.3	-17.5/-18.1	19.01/19.18	$1.27\cdot 10^{12}$	255.1/194.9	-13.2/-12.8	12.78/12.22	$2.30\cdot 10^{12}$	ISM
			1.1/0.6	-24.0/-23.6	2.41/2.37	$2.94\cdot 10^{10}$	5.5/5.3	-16.9/-16.7	2.21/2.06	$1.48\cdot 10^{11}$	
HD 142705	-5.6±3.0	-28.66 (G)	11.1/6.1	-30.8/-30.8	7.39/6.78	$2.84\cdot 10^{11}$	19.7/12.6	-31.3/-31.1	4.9/4.71	$1.77\cdot 10^{11}$	ISM
			40.5/19.9	-17.1/17.2	12.45/11.15	$4.33\cdot 10^{11}$	256.4/225.6	-16.2/-16.2	11.8/10.89	$3.02\cdot 10^{12}$	
HD 144587	-10.7±4.7	-28.81 (G)	11.6/5.1	-7.4/-9.6	6.2/4.52	$1.24\cdot 10^{11}$	122.4/97.7	-9.3/-9.4	7.75/7.43	$1.16\cdot 10^{12}$	ISM
			12.0/<6.0	-20.7/-	8.5/-	$1.28\cdot 10^{11}$	46.1/30.5	-22.3/-22.1	5.77/5.58	$4.06\cdot 10^{11}$	
HD 144981	-5.6±4.3	-29.16 (G)	39.9/19.5	-8.7/-8.7	8.90/8.33	$4.27\cdot 10^{11}$	215.7/184.6	-8.5/-8.1	10.59/9.45	$2.31\cdot 10^{12}$	ISM
			6.2/<3.0	-27.9/-	10.68/-	$6.64\cdot 10^{10}$					
HD 145554	-7.8±3.9	-29.2 (G)	5.6/<3.0	-26.8/-	7.95/-	$5.99\cdot 10^{10}$	46.2/32.9	-25.2/-25.0	4.50/4.5	$4.04\cdot 10^{11}$	ISM
			42.3/24.7	-9.8/-9.8	5.79/5.25	$9.16\cdot 10^{11}$	154.3/138.3	-10.5/-10.1	7.45/6.94	$2.02\cdot 10^{12}$	
HD 145631	-5.7±2.3	-29.21 (G)	35.1/24.9	-8.6/-8.7	5.14/4.46	$6.68\cdot 10^{11}$	162.7/139.9	-9.5/-9.1	7.75/7.03	$1.78\cdot 10^{12}$	ISM
			9.8/<1.8	-27.3/-	15.44/-	$1.05\cdot 10^{11}$	28.7/17.6	-25.0/-24.7	4.51/4.66	$2.70\cdot 10^{11}$	
HD 145964	-6.8±3.1	-29.14 (G)	9.9/2.5	-26.7/-26.5	12.38/7.00	$1.06\cdot 10^{11}$	55.5/41.5	-22.5/-22.2	4.98/5.03	$4.97\cdot 10^{11}$	CS
			4.6/1.6	-9.4/-9.8	5.55/5.46	$4.92\cdot 10^{10}$	60.6/45.3	-9.5/-9.3	4.98/4.92	$5.42\cdot 10^{11}$	
HD 145689	-7.1±1.7	-17.21 (G)	4.1/<0.5	-11.9/-	10.3/-	$4.39\cdot 10^{10}$					CS
HD 146606	-2.3±1.3	-28.52 (G)	7.5/<2.5	-27.1/-	11.5/-	$8.03\cdot 10^{10}$	9.8/5.9	-21.6/-21.7	7.82/9.23	$1.57\cdot 10^{11}$	ISM
							4.8/2.8	-7.8/-7.3	8.56/9.18	$8.36\cdot 10^{10}$	
HD 146897	-3.1±0.9	-29.19 (G)	11.2/<0.9	-8.3/-	5.36/-	$1.20\cdot 10^{11}$	118.2/80.0	-9.4/-9.0	7.93/7.72	$1.06\cdot 10^{12}$	ISM
			5.5/<0.9	-29.5/-	8.58/-	$5.89\cdot 10^{10}$					

Continued on next page

Table B.3 – continued from previous page

Star	V_{rad}	V_{ISM}	Ca II K/H				Na I D2/D1				Origin
			EW	RV	FWHM	N	EW	RV	FWHM	N	
	(km/s)	(km/s)	(mÅ)	(km/s)	(km/s)	(cm^{-2})	(mÅ)	(km/s)	(km/s)	(cm^{-2})	
HD 147137	-6.6±-1.9	-29.12 (G)	22.6/14.1	-8.5/-8.7	7.78/10.1	$4.47\cdot 10^{11}$	154.4/145.1	-8.6/-8.3	8.34/8.42	$5.00\cdot 10^{12}$	ISM
							8.5/6.2	-23.7/-23.9	6.24/6.85	$7.53\cdot 10^{10}$	
HD 147220	-49.3±2.0	-29.16 (G)	62.3/34.5	-19.1/-15.0	17.21/19.49	$1.56\cdot 10^{12}$	59.5/34.8	-20.9/-20.6	11.76/12.1	$5.93\cdot 10^{11}$	ISM
							135.2/126.3	-8.9/-8.7	7.50/7.4	$3.31\cdot 10^{12}$	
HD 148283	-0.5±0.2	-18.54 (NGP)	203.1*/198.2*	1.3/1.6	91.50/90.12	$1.47\cdot 10^{13}$	34.6/22.4	3.6/3.4	34.63/23.51	$2.49\cdot 10^{10}$	CS
HD 156623	-0.2±2.1	-24.89 (G)	9.0/3.7	-15.0/-16.4	18.72/8.79	$9.63\cdot 10^{10}$	-10.6/-8.5	-1.8/0.5	13.66/17.66	$1.01\cdot 10^{11}$	CS+ISM
			4.3/>2.0	8.1/-	6.00	$4.60\cdot 10^{10}$					
HD 158352	-33.9±0.6		8.6/8.3	-24.7/-25.2	3.56/5.1	$5.26\cdot 10^{12}$	14.5/7.8	-25.0/-24.9	4.43/4.37	$1.96\cdot 10^{11}$	CS+ISM?
			20.5/8.5	-28.9/-32.2	13.17/13.44	$2.19\cdot 10^{11}$	3.8/1.9	-30.7/-30.0	10.46/9.92	$3.14\cdot 10^{10}$	
HD 168646	-10.8±2.6	-31.44 (Aql)	315.4*/252.9	-7.3/-6.6	16.07/17.00	$6.51\cdot 10^{12}$	156.6/154.5	-4.8/-4.5	8.98/8.59	$2.40\cdot 10^{12}$	CS
							7.7/<3.0	11.1/-	11.51/-	$3.79\cdot 10^{10}$	
							24.7/12.4	-21.1/-19.9	17.84/-14.77	$1.36\cdot 10^{12}$	
HD 172555	1.2±2.9	-16.84 (G)	6.1/3.0	2.3/3.1	6.8/4.94	$6.53\cdot 10^{10}$	8.0/<1.0	15.4/-	28.03/-	$3.94\cdot 10^{10}$	CS+ISM
			1.5/<1.0	-19.9/-	9.5/-	$1.61\cdot 10^{10}$	3.2/1.78	-20.4/-20.3	9.78/8.88	$3.60\cdot 10^{10}$	
HD 177724	-27.3±2.5	-21.03 (G)	3.4/1.9	-25.7/-25.6	15.02/15.2	$8.25\cdot 10^{10}$					?
		-30.96 (Aql)									
HD 181296	-0.3±1.9		3.6/1.8	-22.7/-22.3	8.50/7.03	$4.25\cdot 10^{11}$	2.6/1.5	-22.7/-21.9	7.11/8.83	$2.60\cdot 10^{10}$	CS
HD 182919	-24.3±1.4	-18.05 (G)	2.8/2.6	-18.5/-18.9	5.98/10.5	$1.22\cdot 10^{11}$	1.8/0.7	-15.5/-15.5	7.13/5.81	$8.87\cdot 10^{9}$	CS+ISM
		-24.21 (Mic)									
		-26.30 (Aql)									
HD 188228	-6.0±3.5	-12.18 (G)	1.3/<0.5	-13.9/-	8.24/-	$3.43\cdot 10^{10}$	3.2/<1.5	-13.9/-	8.26/-	$1.58\cdot 10^{10}$	ISM
		-15.57 (Vel)									
HD 192518	8.1±0.3	-20.08 (Mic)	5.2/3.0	-13.9/-13.8	4.79/5.49	$1.10\cdot 10^{11}$	39.3/26.8	-14.6/-14.5	4.64/4.54	$3.44\cdot 10^{11}$	CS+ISM
		-15.53 (Aql)	334.5*/332.6	11.9/11.6	23.8/21.10	$1.21\cdot 10^{13}$					
HD 196724	-10.8±2.3	-13.52 (Eri)	4.3/1.4	-11.7/-12.5	5.03/4.62	$3.10\cdot 10^{10}$					?
		-9.93 (Aql)									
HD 198160	-16.2±1.9	-17.42 (Vel)	3.9/<1.5	-14.7/-	13.96/-	$4.17\cdot 10^{10}$	1.2/<0.5	-16.4/-	6.78/-	$5.70\cdot 10^{9}$	ISM
HD 198161	-13.5±3.6	-17.41 (Vel)	3.8/<1.5	-14.9/-	11.24/-	$4.07\cdot 10^{10}$	3.4/1.0	-21.9/-18.7	18.48/3.8	$1.67\cdot 10^{10}$	ISM
HD 210418	-5.1±0.8	-5.49 (LIC)	3.0/<1.5	-4.8/-	12.29/-	$3.21\cdot 10^{10}$					?
HD 217782	5.1±1.1	7.63 (Hyades)	20.4/10.7	-9.2/-9.4	5.92/5.51	$7.05\cdot 10^{11}$	53.9/36.1	-8.9/-8.6	4.80/4.64	$4.75\cdot 10^{11}$	CS
			11.0/5.5	-17.1/-17.0	7.58/7.04	$1.18\cdot 10^{11}$	10.6/6.2	-16.4/-16.1	7.71/9.18	$1.08\cdot 10^{11}$	
			5.5/2.2	5.2/5.3	10.55/7.6	$5.89\cdot 10^{10}$					
HD 221756	13.5±0.3	5.88 (LIC)	6.3/2.63	-4.7/-4.8	6.12/5.92	$6.74\cdot 10^{10}$	17.9/9.21	-2.6/-2.4	5.96/5.78	$3.70\cdot 10^{12}$	ISM
		9.00 (Hyades)									
HD 224392	9.9±2.3	-0.86 (Vel)	8.2/3.9	-1.5/-3.5	11.37/6.56	$8.78\cdot 10^{10}$	2.9/1.6	-8.1/5.59	15.80/12.81	$3.23\cdot 10^{10}$	?

Appendix C: Observing Log

Table C.1: Instruments and observing campaigns. In brackets below the star's name SNR in the Ca II K continuum measured in the median for all the available spectra. HEROS observations were taken on service mode during several months as complementary observations. *On March 3rd and 21st during service mode only one spectra was obtained each night.

HD 105 (108)	20151022T0403	FEROS	20151023T0354	FEROS	20151024T0421	FEROS
HD 203 (212)	20150803T0314	HEROS	20150803T0400	HEROS	20150804T0427	HEROS
	20150805T0311	HEROS	20150806T0230	HEROS	20150919T2344	HEROS
	20150920T2324	HEROS	20150923T2307	HEROS	20150924T2300	HEROS
	20151022T0401	FEROS	20151023T0338	FEROS	20151024T0428	FEROS
HR 10 (287)	20150904T0007	HERMES	20150904T0020	HERMES	20150904T0051	HERMES
	20150904T0217	HERMES	20150904T0336	HERMES	20150905T0012	HERMES
	20150905T0033	HERMES	20150905T0054	HERMES	20150905T0314	HERMES
	20150906T0024	HERMES	20150906T0045	HERMES	20150906T0353	HERMES
	20150906T0414	HERMES	20150907T0016	HERMES	20150907T0036	HERMES
	20150907T0257	HERMES	20150907T0317	HERMES	20151022T0402	FEROS
	20151023T0102	FEROS	20151023T0439	FEROS	20151220T1943	HERMES
	20151220T2004	HERMES	20151220T2025	HERMES	20151222T2034	HERMES
	20151222T2100	HERMES	20151223T1951	HERMES	20151223T2017	HERMES
	20151223T2145	HERMES	20160712T0447	HERMES		
HD 1466 (316)	20151023T0126	FEROS	20151023T0521	FEROS	20151024T0456	FEROS
κ Phe (247)	20151023T0112	FEROS	20151024T0517	FEROS		
HD 2884 (251)	20151023T0134	FEROS	20151023T0457	FEROS	20151024T0505	FEROS
	20170924T0543	FEROS				
HD 2885 (141)	20151023T0138	FEROS	20151023T0501	FEROS	20151024T0508	FEROS
HD 3003 (160)	20151023T0141	FEROS	20151024T0513	FEROS		
HD 5267 (419)	20160126T2012	FIES	20160127T1958	FIES	20160712T0427	HERMES
	20160713T0301	HERMES	20160714T0300	HERMES	20160715T0315	HERMES
	20160717T0301	FIES	20160717T0516	FIES	20160718T0259	FIES
	20160718T0449	FIES	20160719T0258	FIES	20160719T0501	FIES
	20160720T0316	FIES	20170924T0513	FEROS	20170924T0701	FEROS
	20170926T0639	FEROS	20170927T0619	FEROS	20170930T0457	FEROS
	20171001T0435	FEROS				
HD 5448 (301)	20151220T1914	HERMES	20160126T2026	FIES	20160127T2011	FIES
	20160713T0253	HERMES	20160714T0414	HERMES	20160717T0255	FIES
	20160718T0310	FIES	20160718T0509	FIES	20160719T0308	FIES
	20160720T0355	FIES				
κ Tuc (381)	20151023T0146	FEROS	20151023T0704	FEROS	20151024T0501	FEROS
49 Cet (405)	20150904T0107	HERMES	20150904T0143	HERMES	20150904T0318	HERMES
	20150904T0539	HERMES	20150905T0117	HERMES	20150905T0133	HERMES
	20150905T0335	HERMES	20150905T0523	HERMES	20150906T0126	HERMES
	20150906T0134	HERMES	20150906T0221	HERMES	20150906T0237	HERMES
	20150906T0529	HERMES	20150907T0113	HERMES	20150907T0129	HERMES
	20150907T0414	HERMES	20150907T0430	HERMES	20151220T2058	HERMES
	20151220T2119	HERMES	20151222T2135	HERMES	20151222T2201	HERMES
	20151222T2227	HERMES	20151223T2113	HERMES	20151223T2246	HERMES
	20160126T1956	FIES	20160126T2041	FIES	20160127T1936	FIES
	20160127T1945	FIES	20160127T1948	HERMES	20160127T2001	HERMES
	20160128T1928	HERMES	20160128T1941	HERMES	20160130T1958	HERMES
	20160130T2011	HERMES	20160714T0500	HERMES	20160715T0449	HERMES
	20160717T0506	FIES	20160718T0458	FIES	20160719T0448	FIES
	20170923T0919	FEROS				
τ Cet (481)	20151023T0152	FEROS	20151023T0540	FEROS		
HD 12039	20151023T0604	FEROS				

Star	Date (UT)	Instrument	Date (UT)	Instrument	Date (UT)	Instrument
(453)						
HD 14055	20150831T0123	HEROS	20150831T0533	HEROS	20151024T2225	HEROS
(412)	20151025T2057	HEROS	20151027T2014	HEROS	20151028T0235	HEROS
	20160126T2033	FIES	20160127T2204	FIES	20160127T2207	FIES
	20160303T2020	HERMES	20160303T2024	HERMES	20160304T2018	HERMES
	20160304T2022	HERMES	20160305T2012	HERMES	20160306T2038	HERMES
	20160712T0505	HERMES	20160713T0506	HERMES	20160714T0351	HERMES
	20160715T0403	HERMES	20160717T0349	FIES	20160718T0359	FIES
	20160719T0404	FIES	20160720T0359	FIES		
HD 14412	20151023T0218	FEROS	20151023T0659	FEROS		
(401)						
HD 15115	20160126T2103	FIES	20160127T2134	FIES	20160717T0429	FIES
(166)	20160718T0418	FIES	20160719T0410	FIES		
HD 15257	20160126T2315	FIES	20160127T2217	FIES	20160127T2314	FIES
(149)	20160713T0418	HERMES	20160714T0421	HERMES	20160715T0411	HERMES
	20160717T0340	FIES	20160718T0326	FIES	20160719T0324	FIES
HD 16978	20151023T0229	FEROS	20151024T0534	FEROS	20170923T0845	FEROS
(309)	20170924T0534	FEROS	20170925T0654	FEROS		
HR 1062	20150904T0301	HERMES	20150904T0518	HERMES	20150905T0254	HERMES
(257)	20150905T0504	HERMES	20150906T0317	HERMES	20150906T0332	HERMES
	20150906T0548	HERMES	20150907T0339	HERMES	20150907T0355	HERMES
	20151220T2142	HERMES	20151220T2203	HERMES	20151222T2336	HERMES
	20151224T0030	HERMES	20160127T2131	HERMES	20160128T2134	HERMES
	20160130T2109	HERMES				
HD 21620	20150904T0123	HERMES	20150904T0244	HERMES	20150905T0153	HERMES
(411)	20150905T0209	HERMES	20150905T0400	HERMES	20150906T0257	HERMES
	20150906T0607	HERMES	20150907T0149	HERMES	20150907T0204	HERMES
	20150907T0533	HERMES	20150907T0549	HERMES	20151220T2336	HERMES
	20151221T0002	HERMES	20151221T0253	HERMES	20151223T0005	HERMES
	20151223T0031	HERMES	20151224T0103	HERMES	20151224T0129	HERMES
	20160127T2147	HERMES	20160127T2355	HERMES	20160128T0030	HERMES
	20160128T2105	HERMES	20160128T2319	HERMES	20160130T2130	HERMES
	20160130T2320	HERMES	20160303T2106	HERMES	20160304T2116	HERMES
	20160305T2103	HERMES	20160306T2119	HERMES	20160714T0435	HERMES
	20160715T0425	HERMES	20160717T0442	FIES	20160718T0430	FIES
	20160719T0421	FIES	20160720T0453	FIES	20170306T1957	HERMES
	20170308T2024	HERMES	20170309T2044	HERMES	20170310T2046	HERMES
	20170311T1944	HERMES	20170313T2028	HERMES		
HD 21997	20150904T0503	HERMES	20150905T0422	HERMES	20150905T0443	HERMES
(594)	20150906T0448	HERMES	20150906T0508	HERMES	20150907T0451	HERMES
	20150907T0512	HERMES	20150919T0453	HEROS	20150920T0251	HEROS
	20150924T0340	HEROS	20150925T0311	HEROS	20150926T0440	HEROS
	20151023T0225	FEROS	20151023T0611	FEROS	20151024T0526	FEROS
	20151110T2302	HEROS	20151111T2230	HEROS	20151114T0058	HEROS
	20151114T2216	HEROS	20151220T2236	HERMES	20151220T2307	HERMES
	20151223T2320	HERMES	20160127T2016	HERMES	20160128T1956	HERMES
	20160130T2035	HERMES	20170923T0436	FEROS	20170923T0612	FEROS
	20170923T0859	FEROS	20170924T0522	FEROS	20170924T0810	FEROS
	20170925T0634	FEROS	20170926T0652	FEROS	20170926T0828	FEROS
	20170927T0631	FEROS	20170929T0505	FEROS	20170930T0505	FEROS
	20170930T0927	FEROS	20171001T0426	FEROS		
10 τ	20150919T0519	HEROS	20150920T0148	HEROS	20150924T0133	HEROS
(919)	20150925T0131	HEROS	20151023T0246	FEROS	20151109T2223	HEROS
	20151109T0111	HEROS	20151114T2100	HEROS	20151114T0130	HEROS
	20151221T0017	HERMES				
HD 27290	20151023T0359	FEROS	20151024T0538	FEROS	20160328T0051	FEROS
(199)						
B τ	20150930T0259	HEROS	20151001T0235	HEROS	20151003T0340	HEROS
(148)	20151004T0217	HEROS	20151209T2056	HEROS	20151209T0017	HEROS
	20151221T0035	HERMES				
HD 29391	20151023T0404	FEROS	20160127T0033	FIES		

Star	Date (UT)	Instrument	Date (UT)	Instrument	Date (UT)	Instrument
(191)						
HD 30051	20151023T0416	FEROS	20160126T2240	FIES	20160127T2239	FIES
(291)	20160127T2324	FIES	20160328T0027	FEROS	20160329T0008	FEROS
HD 31295	20151221T0049	HERMES	20151224T0142	HERMES	20160128T2254	HERMES
(209)	20160128T0034	HERMES	20160130T2159	HERMES		
HD 32297	20150904T0405	HERMES	20150904T0436	HERMES	20151221T0122	HERMES
(223)	20151221T0153	HERMES	20151221T0224	HERMES	20151223T0106	HERMES
	20151223T0136	HERMES	20151224T0215	HERMES	20151224T0246	HERMES
	20160126T2133	FIES	20160126T2205	FIES	20160127T2022	FIES
	20160127T2053	FIES	20160127T2216	HERMES	20160127T2246	HERMES
	20160128T2149	HERMES	20160128T2220	HERMES	20160130T2216	HERMES
	20160130T2247	HERMES	20170924T0726	FEROS	20170926T0704	FEROS
	20170926T0847	FEROS	20170927T0703	FEROS	20170927T0847	FEROS
	20170929T0740	FEROS	20170930T0705	FEROS	20170930T0825	FEROS
	20171001T0651	FEROS				
HD 35850	20151015T0217	HEROS	20151016T0230	HEROS	20151017T0545	HEROS
(190)	20151019T0440	HEROS	20151020T0246	HEROS	20151023T0619	FEROS
	20151210T0041	HEROS	20151210T0143	HEROS	20151210T0308	HEROS
	20151213T2132	HEROS	20151217T2152	HEROS	20151218T2157	HEROS
	20160127T0043	FIES	20160128T0054	FIES	20160329T0101	FEROS
HD 36546	20170306T2017	HERMES	20170307T1952	HERMES	20170307T2122	HERMES
(221)	20170308T1951	HERMES	20170309T2056	HERMES	20170310T2013	HERMES
	20170312T2003	HERMES	20170401T2046	HERMES		
HD 37286	20151023T0422	FEROS	20151024T0545	FEROS	20160329T0115	FEROS
(160)						
HD 37306	20151023T0751	FEROS	20151023T0831	FEROS	20160303T2040	HERMES
(441)	20160303T2218	HERMES	20160303T2239	HERMES	20160304T2043	HERMES
	20160304T2230	HERMES	20160304T2251	HERMES	20160305T2031	HERMES
	20160305T2227	HERMES	20160306T2059	HERMES	20160321T2023	FIES
	20160328T0036	FEROS	20160329T0017	FEROS	20170307T2047	HERMES
	20170308T2038	HERMES	20170309T2016	HERMES	20170310T2059	HERMES
	20170311T2053	HERMES	20170312T2128	HERMES	20170313T2051	HERMES
	20170923T0630	FEROS	20170923T0908	FEROS	20170924T0709	FEROS
	20170925T0711	FEROS	20170925T0719	FEROS	20170926T0743	FEROS
	20170927T0655	FEROS	20170930T0914	FEROS		
HD 38206	20151023T0428	FEROS	20151023T0757	FEROS	20160303T1955	HERMES
(353)	20160303T2009	HERMES	20160303T2129	HERMES	20160303T2142	HERMES
	20160304T1949	HERMES	20160304T2005	HERMES	20160304T2141	HERMES
	20160304T2154	HERMES	20160305T1953	HERMES	20160305T2157	HERMES
	20160306T2019	HERMES	20160326T0131	FEROS	20160328T0044	FEROS
	20160328T0128	FEROS	20160329T0026	FEROS	20160329T0124	FEROS
	20161230T0024	FIES	20170307T2103	HERMES	20170308T2100	HERMES
	20170309T2031	HERMES	20170310T2114	HERMES	20170311T2007	HERMES
	20170312T2036	HERMES	20170313T2005	HERMES		
HR 2025	20170307T2024	HERMES	20170307T2155	HERMES	20170308T2113	HERMES
(243)	20170309T2129	HERMES	20170310T2126	HERMES	20170311T2029	HERMES
	20170312T2054	HERMES	20170313T2119	HERMES	20170331T2037	HERMES
	20170403T2029	HERMES				
ξ Aur	20170401T2007	HERMES	20170402T2007	HERMES		
(219)						
η Lep	20151015T0342	HEROS	20151016T0304	HEROS	20151017T0650	HEROS
(212)	20151019T0512	HEROS	20151023T0451	FEROS	20151210T0125	HEROS
	20151213T2157	HEROS	20151217T2217	HEROS	20151218T0306	HEROS
	20151223T0147	HERMES	20160328T0056	FEROS		
HD 42111	20150904T0528	HERMES	20150905T0542	HERMES	20150905T0558	HERMES
(446)	20151221T0321	HERMES	20151223T0215	HERMES	20151224T0314	HERMES
	20160128T2302	HERMES	20160128T0043	HERMES	20160130T2359	HERMES
	20160303T2159	HERMES	20160304T2210	HERMES	20160305T2131	HERMES
	20160305T2329	HERMES	20160306T2246	HERMES	20170308T2136	HERMES
	20170309T2152	HERMES	20170311T2110	HERMES	20170311T2128	HERMES

Star	Date (UT)	Instrument	Date (UT)	Instrument	Date (UT)	Instrument
	20170312T2151	HERMES	20170313T2152	HERMES	20170329T2013	HERMES
	20170330T2009	HERMES	20170402T2017	HERMES	20170403T2012	HERMES
	20170404T0131	FEROS	20170405T0042	FEROS	20170406T0050	FEROS
	20170408T0101	FEROS	20170409T0050	FEROS		
HD 53842 (102)	20151023T0633	FEROS	20160328T0232	FEROS		
HD 50241 (617)	20151023T0526	FEROS	20160326T0144	FEROS	20160326T0304	FEROS
	20160326T0305	FEROS	20160327T0229	FEROS	20160327T0230	FEROS
	20160328T0102	FEROS	20160328T0159	FEROS	20160328T0322	FEROS
	20160329T0031	FEROS	20160329T0153	FEROS	20160329T0314	FEROS
	20170924T0806	FEROS				
HD 50571 (165)	20151023T0532	FEROS	20160326T0232	FEROS		
λ Gem (186)	20151221T0433	HERMES	20160131T0049	HERMES	20160328T0108	FEROS
ϕ Gem (238)	20170328T2002	HERMES	20170331T2012	HERMES	20170402T2028	HERMES
HD 71043 (302)	20151023T0640	FEROS	20160326T0238	FEROS	20170923T0852	FEROS
	20170924T0923	FEROS	20170925T0704	FEROS	20170927T0829	FEROS
HD 71722 (461)	20151023T0648	FEROS	20160326T0151	FEROS	20160326T0326	FEROS
	20160326T0447	FEROS	20160327T0238	FEROS	20160327T0504	FEROS
	20160328T0118	FEROS	20160328T0332	FEROS	20160329T0041	FEROS
	20160329T0203	FEROS	20160329T0324	FEROS	20160329T0440	FEROS
HD 74873 (299)	20151221T0450	HERMES	20151221T0506	HERMES	20151224T0516	HERMES
	20160129T0451	HERMES	20160131T0029	HERMES	20160304T0011	HERMES
	20160304T0027	HERMES	20160304T0203	HERMES	20160305T0020	HERMES
	20160305T0203	HERMES	20160305T2352	HERMES	20160306T0211	HERMES
	20160307T0052	HERMES				
67 Cnc (194)	20170401T2020	HERMES	20170402T2041	HERMES		
HR 3685 (738)	20160326T0156	FEROS	20160326T0157	FEROS	20160326T0331	FEROS
	20160326T0332	FEROS	20160326T0541	FEROS	20160326T0542	FEROS
	20160327T0242	FEROS	20160327T0244	FEROS	20160327T0508	FEROS
	20160327T0510	FEROS	20160328T0133	FEROS	20160328T0134	FEROS
	20160328T0336	FEROS	20160328T0338	FEROS	20160328T0537	FEROS
	20160328T0538	FEROS	20160329T0045	FEROS	20160329T0047	FEROS
	20160329T0208	FEROS	20160329T0209	FEROS	20160329T0330	FEROS
	20160329T0332	FEROS	20160329T0512	FEROS	20160329T0513	FEROS
	20170402T0048	FEROS	20170402T0049	FEROS	20170403T0100	FEROS
	20170403T0101	FEROS	20170405T0057	FEROS	20170405T0058	FEROS
	20170406T0035	FEROS	20170406T0037	FEROS	20170407T0157	FEROS
	20170407T0158	FEROS	20170408T0128	FEROS	20170408T0129	FEROS
HD 85905 (593)	20151221T0534	HERMES	20151221T0600	HERMES	20151223T0453	HERMES
	20151223T0606	HERMES	20151223T0654	HERMES	20151224T0453	HERMES
	20151224T0558	HERMES	20151224T0701	HERMES	20160127T0340	FIES
	20160129T0314	HERMES	20160129T0357	HERMES	20160131T0157	HERMES
	20160131T0313	HERMES	20160303T2304	HERMES	20160303T2326	HERMES
	20160304T0050	HERMES	20160304T0116	HERMES	20160304T2315	HERMES
	20160304T2338	HERMES	20160305T0055	HERMES	20160305T0121	HERMES
	20160305T2300	HERMES	20160306T0051	HERMES	20160306T0122	HERMES
	20160306T2317	HERMES	20160306T2348	HERMES	20160307T0127	HERMES
	20170308T2148	HERMES	20170310T2144	HERMES	20170311T2147	HERMES
	20170311T2337	HERMES	20170312T0021	HERMES	20170329T2234	HERMES
	20170331T2231	HERMES	20170401T2225	HERMES	20170402T0029	FEROS
	20170402T0416	FEROS	20170402T2227	HERMES	20170403T0114	FEROS
	20170403T2216	HERMES	20170404T0145	FEROS	20170405T0111	FEROS
	20170406T0104	FEROS	20170407T0209	FEROS	20170408T0113	FEROS
	20170408T0513	FEROS	20170409T0104	FEROS		
HD 95418 (426)	20160108T0034	HEROS	20160127T0212	FIES	20160127T0214	FIES
	20160127T0530	FIES	20160127T0531	FIES	20160128T0129	FIES

Star	Date (UT)	Instrument	Date (UT)	Instrument	Date (UT)	Instrument
	20160128T0143	FIES	20160128T0145	FIES	20160303T0228	FIES
	20160303T2356	HERMES	20160303T2358	HERMES	20160304T0215	HERMES
	20160304T0218	HERMES	20160305T0007	HERMES	20160305T0143	HERMES
	20160305T0146	HERMES	20160306T0008	HERMES	20160306T0249	HERMES
	20160307T0107	HERMES	20160711T2057	HERMES	20160718T2134	FIES
	20160719T2137	FIES	20170307T0154	HERMES	20170307T0157	HERMES
	20170307T0202	HERMES	20170307T0317	HERMES	20170307T0318	HERMES
	20170307T0345	HERMES	20170307T0348	HERMES	20170307T0510	HERMES
	20170307T0514	HERMES	20170307T2115	HERMES	20170307T2117	HERMES
	20170308T0410	HERMES	20170308T2212	HERMES	20170308T2214	HERMES
	20170309T2204	HERMES	20170309T2206	HERMES	20170311T0455	HERMES
	20170311T2328	HERMES	20170311T2331	HERMES	20170312T2209	HERMES
ϕ Leo	20151221T0627	HERMES	20151223T0501	HERMES	20151223T0614	HERMES
(1934)	20151223T0706	HERMES	20151223T0715	HERMES	20151224T0524	HERMES
	20160127T0411	FIES	20160127T0536	FIES	20160128T0114	HERMES
	20160128T0126	HERMES	20160129T0339	HERMES	20160129T0510	HERMES
	20160129T0623	HERMES	20160131T0220	HERMES	20160131T0344	HERMES
	20160131T0451	HERMES	20160303T2343	HERMES	20160303T2348	HERMES
	20160304T0300	HERMES	20160304T0306	HERMES	20160304T2354	HERMES
	20160304T2359	HERMES	20160305T0307	HERMES	20160305T0314	HERMES
	20160306T0016	HERMES	20160306T0257	HERMES	20160307T0010	HERMES
	20160307T0213	HERMES	20160307T0224	HERMES	20160326T0138	FEROS
	20160326T0312	FEROS	20160326T0315	FEROS	20160326T0553	FEROS
	20160327T0252	FEROS	20160327T0449	FEROS	20160327T0454	FEROS
	20160327T0601	FEROS	20160328T0153	FEROS	20160328T0346	FEROS
	20160328T0548	FEROS	20160329T0218	FEROS	20160329T0340	FEROS
	20160329T0522	FEROS	20160511T2021	HERMES	20160511T2044	HERMES
	20160511T2054	HERMES	20160511T2105	HERMES	20160511T2116	HERMES
	20160511T2127	HERMES	20160511T2138	HERMES	20160511T2151	HERMES
	20160511T2202	HERMES	20160511T2213	HERMES	20160511T2224	HERMES
	20160511T2234	HERMES	20160511T2245	HERMES	20160511T2317	HERMES
	20160511T2327	HERMES	20160511T2338	HERMES	20160511T2349	HERMES
	20160512T0000	HERMES	20160512T0011	HERMES	20160512T0020	HERMES
β Leo	20151221T0631	HERMES	20160115T0157	HEROS	20160116T0157	HEROS
(326)	20160127T0220	FIES	20160127T0221	FIES	20160127T0640	FIES
	20160127T0642	FIES	20160127T0644	FIES	20160129T0517	HERMES
	20160131T0446	HERMES	20160131T0447	HERMES	20160326T0209	FEROS
	20160326T0211	FEROS	20160329T0130	FEROS	20160329T0131	FEROS
	20160711T2053	HERMES	20160712T2055	HERMES	20160713T2057	HERMES
	20160717T2129	FIES	20160718T2130	FIES	20160719T2133	FIES
HD 104731	20160326T0217	FEROS	20160329T0140	FEROS		
(271)						
hd 104860	20160127T0233	FIES	20160127T0305	FIES		
(154)						
EF Cha	20170402T0343	FEROS	20170403T0155	FEROS	20170404T0206	FEROS
(375)	20170405T0150	FEROS	20170406T0238	FEROS	20170407T0304	FEROS
	20170408T0159	FEROS	20170409T0314	FEROS		
HD 105850	20160326T0222	FEROS	20160329T0147	FEROS	20170309T0219	HERMES
(311)	20170329T0244	HERMES	20170331T0326	HERMES		
δ Crv	20151221T0636	HERMES	20151223T0619	HERMES	20160115T0245	HEROS
(324)	20160116T0513	HEROS	20160127T0407	FIES	20160129T0521	HERMES
	20160131T0253	HERMES	20160304T0149	HERMES	20160304T0151	HERMES
	20160305T0138	HERMES	20160305T0345	HERMES	20160305T0348	HERMES
	20160306T0142	HERMES	20160307T0146	HERMES	20160307T0204	HERMES
	20170307T0311	HERMES	20170329T0259	HERMES		
η crv	20151221T0647	HERMES	20151223T0623	HERMES	20160129T0526	HERMES
(138)	20160131T0302	HERMES				
HR 4796	20160326T0205	FEROS	20160326T0343	FEROS	20160327T0259	FEROS
(714)	20160327T0704	FEROS	20160327T0947	FEROS	20160328T0145	FEROS
	20160328T0356	FEROS	20160328T0734	FEROS	20160328T1012	FEROS
	20160329T0229	FEROS	20160329T0354	FEROS	20160329T0802	FEROS

Star	Date (UT)	Instrument	Date (UT)	Instrument	Date (UT)	Instrument
	20170402T0210	FEROS	20170402T0712	FEROS	20170403T0352	FEROS
	20170404T0346	FEROS	20170405T0449	FEROS	20170405T0621	FEROS
	20170406T0318	FEROS	20170407T0402	FEROS	20170407T0709	FEROS
	20170408T0238	FEROS	20170409T0339	FEROS		
HD 110058	20170402T0440	FEROS	20170403T0414	FEROS	20170404T0402	FEROS
(383)	20170405T0329	FEROS	20170406T0331	FEROS	20170407T0418	FEROS
	20170408T0251	FEROS	20170409T0410	FEROS		
HD 110411	20151221T0615	HERMES	20151221T0702	HERMES	20151221T0715	HERMES
(625)	20151223T0513	HERMES	20151223T0537	HERMES	20151224T0612	HERMES
	20160127T0423	FIES	20160127T0559	FIES	20160115T0201	HEROS
	20160116T0201	HEROS	20160129T0347	HERMES	20160129T0543	HERMES
	20160131T0231	HERMES	20160131T0238	HERMES	20160131T0359	HERMES
	20160131T0405	HERMES	20160131T0512	HERMES	20160131T0519	HERMES
	20160304T0135	HERMES	20160304T0142	HERMES	20160304T0314	HERMES
	20160304T0321	HERMES	20160304T0644	HERMES	20160305T0036	HERMES
	20160305T0325	HERMES	20160305T0336	HERMES	20160305T0626	HERMES
	20160306T0027	HERMES	20160306T0151	HERMES	20160306T0311	HERMES
	20160306T0327	HERMES	20160307T0021	HERMES	20160307T0032	HERMES
	20160307T0155	HERMES	20160711T2100	HERMES	20160712T2206	HERMES
	20160713T2124	HERMES	20160714T2054	HERMES	20160716T2231	FIES
	20160718T2137	FIES	20160719T2147	FIES	20170307T0220	HERMES
	20170307T0231	HERMES	20170307T0242	HERMES	20170307T0602	HERMES
	20170307T0613	HERMES	20170308T0519	HERMES	20170309T0455	HERMES
	20170312T0442	HERMES	20170313T0437	HERMES	20170329T0311	HERMES
	20170331T0341	HERMES	20170401T0312	HERMES	20170402T0151	FEROS
	20170403T0221	FEROS	20170404T0243	FEROS	20170404T0325	HERMES
	20170405T0216	FEROS	20170406T0303	FEROS	20170407T0329	FEROS
	20170408T0224	FEROS	20170409T0354	FEROS		
24 CVn	20170402T0318	HERMES	20170403T0320	HERMES		
(148)						
HD 121191	20170601T0121	FEROS				
(193)						
HD 121617	20170409T0238	FEROS	20170409T0611	FEROS		
(161)						
λ Böo	20151223T0524	HERMES	20151224T0627	HERMES	20160127T0435	FIES
(221)	20160127T0724	FIES	20160711T2048	HERMES	20160711T2353	HERMES
HD 131488	20170409T0219	FEROS	20170409T0551	FEROS		
(172)						
HD 131835	20160326T0408	FEROS	20160326T0755	FEROS	20160327T0322	FEROS
(568)	20160327T0544	FEROS	20160327T0754	FEROS	20160328T0315	FEROS
	20160328T0455	FEROS	20160328T0808	FEROS	20160329T0304	FEROS
	20160329T0429	FEROS	20160329T0836	FEROS	20170403T0519	FEROS
	20170407T0456	FEROS	20170408T0322	FEROS		
HR 5774	20170307T0324	HERMES	20170307T0445	HERMES	20170307T0455	HERMES
(427)	20170308T0359	HERMES	20170308T0615	HERMES	20170309T0237	HERMES
	20170310T0508	HERMES	20170311T0502	HERMES	20170312T0505	HERMES
	20170313T0455	HERMES	20170329T0330	HERMES	20170331T0359	HERMES
	20170401T0330	HERMES	20170402T0613	HERMES	20170404T0541	HERMES
α CrB	20160127T0442	FIES	20160127T0444	FIES	20160127T0656	FIES
(326)	20160127T0657	FIES	20160711T2359	HERMES	20160714T0041	HERMES
	20160716T2314	FIES	20160717T2356	FIES	20160718T2220	FIES
	20160719T0055	FIES	20160719T2331	FIES		
HIP 76310	20160304T0412	HERMES	20160304T0443	HERMES	20160305T0407	HERMES
(450)	20160305T0438	HERMES	20160305T0509	HERMES	20160306T0418	HERMES
	20160306T0449	HERMES	20160326T0424	FEROS	20160326T0817	FEROS
	20160327T0336	FEROS	20160327T0626	FEROS	20160327T0828	FEROS
	20160328T0421	FEROS	20160328T0833	FEROS	20160329T0506	FEROS
	20160329T0901	FEROS	20160711T2124	HERMES	20160712T2218	HERMES
	20160712T2249	HERMES	20160713T2133	HERMES	20160713T2204	HERMES
	20160714T2102	HERMES	20160716T2118	FIES	20160717T2133	FIES
	20160718T2147	FIES	20160719T2215	FIES	20170309T0503	HERMES

Star	Date (UT)	Instrument	Date (UT)	Instrument	Date (UT)	Instrument
	20170310T0555	HERMES	20170310T0626	HERMES	20170314T0437	HERMES
	20170314T0508	HERMES	20170314T0539	HERMES	20170403T0452	FEROS
	20170404T0421	HERMES	20170405T0505	FEROS	20170406T0443	FEROS
	20170408T0354	FEROS				
HIP 77815	20160326T0649	FEROS	20160716T2153	FIES	20170308T0415	HERMES
(127)	20170308T0446	HERMES	20170313T0555	HERMES	20170329T0356	HERMES
	20170330T0337	HERMES	20170330T0408	HERMES	20170331T0425	HERMES
	20170401T0452	HERMES	20170402T0636	FEROS	20170405T0401	FEROS
	20170406T0402	FEROS	20170407T0547	FEROS	20170408T0415	FEROS
HIP 77911	20160711T2107	HERMES	20160326T0701	FEROS	20170401T0419	HERMES
(372)	20170401T0557	HERMES	20170402T0342	HERMES	20170402T0412	HERMES
	20170402T0540	FEROS	20170405T0532	FEROS		
HIP 78099	20160326T0719	FEROS	20160327T0354	FEROS	20160714T2145	HERMES
(123)	20160714T2216	HERMES	20170403T0344	HERMES	20170404T0440	FEROS
HIP 78996	20160327T0424	FEROS	20160717T2210	FIES	20170311T0619	HERMES
(167)	20170330T0546	HERMES	20170403T0638	FEROS	20170409T0652	FEROS
HIP 79156	20160328T0724	FEROS	20160717T2255	FIES	20160719T2335	FIES
(168)	20170406T0532	FEROS				
HIP 79410	20160329T0556	FEROS	20160714T2248	HERMES	20160714T2319	HERMES
(150)	20170402T0445	HERMES				
HIP 79439	20160329T0630	FEROS	20160716T2251	FIES	20170309T0553	HERMES
(212)	20170329T0541	HERMES	20170329T0612	HERMES	20170330T0513	HERMES
	20170402T0824	FEROS				
HD 145964	20160304T0514	HERMES	20160304T0540	HERMES	20160305T0542	HERMES
(576)	20160306T0522	HERMES	20160306T0553	HERMES	20160326T0614	FEROS
	20160327T0649	FEROS	20160328T0622	FEROS	20160329T0747	FEROS
	20160711T2330	HERMES	20160713T2101	HERMES	20160713T2340	HERMES
	20160716T2054	FIES	20160717T2056	FIES	20160718T2056	FIES
	20160719T2058	FIES	20170307T0529	HERMES	20170307T0545	HERMES
	20170308T0541	HERMES	20170308T0557	HERMES	20170309T0536	HERMES
	20170310T0516	HERMES	20170311T0514	HERMES	20170312T0524	HERMES
	20170329T0428	HERMES	20170330T0441	HERMES	20170331T0458	HERMES
	20170402T0516	FEROS	20170402T0517	HERMES	20170403T0435	HERMES
	20170403T0614	FEROS	20170404T0349	HERMES	20170404T0453	HERMES
	20170404T0540	FEROS	20170404T0745	FEROS	20170405T0635	FEROS
	20170405T0824	FEROS	20170406T0603	FEROS	20170407T0528	FEROS
	20170408T0602	FEROS	20170409T0627	FEROS		
HIP 79797	20160328T0530	FEROS	20170404T0630	FEROS	20170405T0605	FEROS
(324)	20170407T0716	FEROS	20170408T0544	FEROS		
HIP 79878	20160711T2225	HERMES	20160719T2249	FIES	20170403T0555	FEROS
(150)	20170409T0435	FEROS				
HD 146624	20160328T0650	FEROS	20160716T2141	FIES	20170405T0553	FEROS
(246)						
HIP 79977	20160712T2100	HERMES	20160712T2131	HERMES	20170405T0702	FEROS
(165)	20170405T0733	FEROS	20170407T0726	FEROS	20170407T0756	FEROS
	20170930T0017	FEROS	20170930T0048	FEROS	20171001T0012	FEROS
	20171001T0042	FEROS				
HIP 80088	20160326T0522	FEROS	20160718T2224	FIES	20160718T2256	FIES
(220)	20170406T0709	FEROS	20170406T0735	FEROS	20170408T0730	FEROS
	20170408T0756	FEROS				
HIP 80130	20160713T2236	HERMES	20160713T2307	HERMES	20170401T0525	HERMES
(139)	20170403T0759	FEROS	20170409T0726	FEROS	20170409T0747	FEROS
HR 6123	20150903T2033	HERMES	20150903T2133	HERMES	20150903T2235	HERMES
(642)	20150903T2336	HERMES	20150904T2032	HERMES	20150904T2130	HERMES
	20150904T2222	HERMES	20150904T2230	HERMES	20150905T2036	HERMES
	20150905T2043	HERMES	20150905T2141	HERMES	20150905T2148	HERMES
	20150905T2315	HERMES	20150905T2321	HERMES	20150906T2028	HERMES
	20150906T2034	HERMES	20150906T2145	HERMES	20150906T2152	HERMES

Star	Date (UT)	Instrument	Date (UT)	Instrument	Date (UT)	Instrument
	20150906T2302	HERMES	20150906T2309	HERMES	20160127T0449	FIES
	20160127T0502	FIES	20160127T0611	FIES	20160127T0624	FIES
	20160129T0423	HERMES	20160129T0435	HERMES	20160129T0554	HERMES
	20160129T0606	HERMES	20160131T0417	HERMES	20160131T0430	HERMES
	20160131T0530	HERMES	20160131T0542	HERMES	20160304T0230	HERMES
	20160304T0246	HERMES	20160304T0334	HERMES	20160304T0347	HERMES
	20160304T0631	HERMES	20160305T0229	HERMES	20160305T0250	HERMES
	20160305T0609	HERMES	20160306T0235	HERMES	20160306T0349	HERMES
	20160306T0620	HERMES	20160307T0248	HERMES	20160307T0315	HERMES
	20160712T0003	HERMES	20160712T2322	HERMES	20160713T0218	HERMES
	20160714T0013	HERMES	20160714T2352	HERMES	20160715T0206	HERMES
	20160716T2330	FIES	20160717T2245	FIES	20160718T0226	FIES
	20160718T2329	FIES	20160719T0201	FIES	20160719T2201	FIES
	20160720T0127	FIES	20170308T0527	HERMES	20170308T0644	HERMES
	20170309T0249	HERMES	20170310T0540	HERMES	20170311T0547	HERMES
	20170312T0557	HERMES	20170313T0513	HERMES	20170403T0549	HERMES
HIP 84881	20151022T0514	FEROS	20160326T0438	FEROS	20160326T0838	FEROS
(567)	20160327T0441	FEROS	20160327T0902	FEROS	20160328T0520	FEROS
	20160328T0858	FEROS	20160329T0655	FEROS	20160329T0925	FEROS
	20170402T0931	FEROS	20170405T0839	FEROS	20170406T0619	FEROS
	20170408T0717	FEROS				
HD 157728	20160127T0545	FIES	20160127T0711	FIES	20160712T0146	HERMES
(476)	20160717T0210	FIES	20160718T0235	FIES	20160719T0239	FIES
HR 6507	20170401T0352	HERMES	20170402T0542	HERMES	20170403T0410	HERMES
(190)	20170404T0516	HERMES				
HD 162003	20160127T0519	FIES	20160127T0702	FIES	20160129T0534	HERMES
(365)	20160131T0501	HERMES				
hd 162917	20160712T0111	HERMES	20160713T0317	HERMES	20160717T0219	FIES
(126)	20160718T0247	FIES	20160719T0248	FIES		
HD 164249	20151022T0355	FEROS	20151023T0035	FEROS		
(225)						
HR 6864	20170402T0607	FEROS	20170403T0713	FEROS	20170404T0658	FEROS
(318)	20170405T0650	FEROS	20170405T0832	FEROS	20170406T0654	FEROS
	20170407T0701	FEROS	20170408T0638	FEROS	20170409T0643	FEROS
HD 172555	20151022T0356	FEROS	20151023T0238	FEROS	20160326T0534	FEROS
(468)	20160326T0849	FEROS	20160327T0715	FEROS	20160327T0958	FEROS
	20160328T0638	FEROS	20160328T0943	FEROS	20160329T0706	FEROS
	20160329T0934	FEROS	20170402T0629	FEROS	20170403T0721	FEROS
	20170404T0707	FEROS	20170405T0657	FEROS	20170406T0703	FEROS
	20170407T0656	FEROS	20170408T0647	FEROS	20170924T0127	FEROS
	20170928T0135	FEROS	20170930T0133	FEROS	20171001T0128	FEROS
110 Her	20150903T2053	HERMES	20150903T2141	HERMES	20150903T2145	HERMES
(423)	20150903T2156	HERMES	20150903T2259	HERMES	20150903T2302	HERMES
	20150904T0035	HERMES	20150904T2041	HERMES	20150904T2138	HERMES
	20150904T2239	HERMES	20150904T2243	HERMES	20150904T2337	HERMES
	20150904T2341	HERMES	20150905T2051	HERMES	20150905T2054	HERMES
	20150905T2157	HERMES	20150905T2200	HERMES	20150906T2059	HERMES
	20150906T2102	HERMES	20150906T2217	HERMES	20150906T2220	HERMES
ζ Aql	20160305T0637	HERMES	20160306T0651	HERMES	20160328T1001	FEROS
(467)	20160712T0142	HERMES	20160713T0248	HERMES	20160714T0410	HERMES
	20160717T0242	FIES	20160718T0013	FIES	20160719T0124	FIES
	20160720T0425	FIES	20170307T0650	HERMES	20170308T0639	HERMES
	20170312T0634	HERMES	20170313T0533	HERMES	20170329T0633	HERMES
	20170329T0638	HERMES				
HD 181296	20151022T0357	FEROS	20151023T0041	FEROS	20151024T0309	FEROS
(415)	20160326T0620	FEROS	20160326T0855	FEROS	20160327T0719	FEROS
	20160327T1004	FEROS	20160328T0644	FEROS	20160328T0949	FEROS
	20160329T0712	FEROS	20160329T0942	FEROS	20170403T0726	FEROS
	20170404T0739	FEROS	20170405T0815	FEROS	20170406T0802	FEROS

Star	Date (UT)	Instrument	Date (UT)	Instrument	Date (UT)	Instrument
	20170407T0840	FEROS	20170408T0652	FEROS	20170924T0132	FEROS
	20170928T0143	FEROS	20171001T0122	FEROS		
HD 181327	20170403T0731	FEROS	20170404T0713	FEROS	20170406T0806	FEROS
(221)	20170407T0845	FEROS	20170408T0657	FEROS		
δ Aql	20160328T0957	FEROS	20160711T2303	HERMES		
(206)						
5 Vul	20150905T2209	HERMES	20150905T2216	HERMES	20150905T2331	HERMES
(438)	20150905T2338	HERMES	20150906T2044	HERMES	20150906T2051	HERMES
	20150906T2203	HERMES	20150906T2210	HERMES	20150906T2334	HERMES
	20150906T2341	HERMES	20160304T0602	HERMES	20160304T0614	HERMES
	20160305T0649	HERMES	20160306T0639	HERMES	20160712T0016	HERMES
	20160712T0400	HERMES	20160712T2341	HERMES	20160713T0236	HERMES
	20160714T0027	HERMES	20160714T0246	HERMES	20160715T0005	HERMES
	20160715T0219	HERMES	20160716T2341	FIES	20160717T0231	FIES
	20160717T0417	FIES	20160717T2337	FIES	20160718T0315	FIES
	20160719T0059	FIES	20160719T0314	FIES	20160720T0432	FIES
	20170307T0627	HERMES	20170307T0638	HERMES	20170308T0626	HERMES
	20170309T0626	HERMES	20170311T0604	HERMES	20170312T0617	HERMES
	20170313T0537	HERMES	20170407T0914	FEROS	20170409T0922	FEROS
HD 183324	20160711T2202	HERMES	20160712T0043	HERMES	20160712T0341	HERMES
(337)	20160713T0004	HERMES	20160714T0044	HERMES	20160714T0337	HERMES
	20160715T0018	HERMES	20160715T0301	HERMES	20160716T2241	FIES
	20160717T0130	FIES	20160717T0330	FIES	20160718T0208	FIES
	20160718T0406	FIES	20160718T2339	FIES	20160719T0229	FIES
	20160719T2321	FIES	20160720T0201	FIES	20170329T0514	HERMES
	20170331T0526	HERMES	20170404T0530	HERMES	20170404T0819	FEROS
	20170405T0807	FEROS	20170407T0831	FEROS	20170409T0851	FEROS
α Aql	20150903T2058	HERMES	20150903T2200	HERMES	20150903T2309	HERMES
(329)	20150904T2045	HERMES	20150904T2046	HERMES	20150904T2148	HERMES
	20150904T2150	HERMES	20150905T2058	HERMES	20150905T2059	HERMES
	20150906T2105	HERMES	20150906T2106	HERMES	20150907T0001	HERMES
	20150907T0002	HERMES	20160711T2308	HERMES		
HD 188228	20151022T0359	FEROS	20151023T0252	FEROS	20151024T0328	FEROS
(147)	20160328T1019	FEROS				
HR 7731	20150903T2244	HERMES	20150903T2355	HERMES	20150904T0202	HERMES
(410)	20150904T2250	HERMES	20150904T2256	HERMES	20150904T2348	HERMES
	20150904T2354	HERMES	20150905T0224	HERMES	20150905T0231	HERMES
	20150905T2244	HERMES	20150905T2250	HERMES	20150906T0001	HERMES
	20150906T0006	HERMES	20150906T2234	HERMES	20150906T2239	HERMES
	20150906T2350	HERMES	20150906T2356	HERMES	20150907T0219	HERMES
	20150907T0225	HERMES	20151223T1911	HERMES	20151223T1922	HERMES
	20160711T2317	HERMES	20160713T0022	HERMES	20160715T0031	HERMES
	20160716T2352	FIES	20160718T0001	FIES	20160719T0111	FIES
	20160720T0442	FIES	20170329T0454	HERMES	20170330T0614	HERMES
	20170403T0503	HERMES	20170404T0558	HERMES		
29 Vul	20170402T0559	HERMES	20170403T0526	HERMES	20170404T0550	HERMES
(329)	20170924T0139	FEROS				
HR 7959	20170404T0800	FEROS	20170405T0854	FEROS	20170407T0905	FEROS
(297)	20170924T0158	FEROS				
HR 7960	20170404T0809	FEROS	20170924T0213	FEROS	20170926T0754	FEROS
(190)	20170927T0742	FEROS				
HD 199143	20151022T0358	FEROS	20151023T0054	FEROS	20160326T0917	FEROS
(353)	20160327T0936	FEROS	20160328T0933	FEROS	20160329T1016	FEROS
α Cep	20150903T2103	HERMES	20150903T2150	HERMES	20150903T2251	HERMES
(285)	20150904T2053	HERMES	20150904T2055	HERMES	20150904T2144	HERMES
	20150904T2302	HERMES	20150904T2304	HERMES	20150905T2104	HERMES
	20150905T2105	HERMES	20150905T2224	HERMES	20150905T2225	HERMES
	20150906T2111	HERMES	20150906T2112	HERMES	20150906T2225	HERMES
	20150906T2227	HERMES	20160711T2312	HERMES		
HD 202917	20151022T0359	FEROS	20151023T0325	FEROS	20151024T0402	FEROS
(248)						

Star	Date (UT)	Instrument	Date (UT)	Instrument	Date (UT)	Instrument
τ PsA (351)	20151022T0400	FEROS	20151023T0332	FEROS	20151024T0408	FEROS
HD 210418 (558)	20160712T0336	HERMES	20160712T0442	HERMES	20160713T0339	HERMES
	20160715T0254	HERMES	20160717T0204	FIES	20160717T0412	FIES
	20160717T0502	FIES	20160718T0202	FIES	20160718T0354	FIES
	20160719T0149	FIES	20160719T0434	FIES	20160720T0343	FIES
ϵ Cep (363)	20150903T2107	HERMES	20150903T2123	HERMES	20150903T2225	HERMES
	20150903T2327	HERMES	20150903T2347	HERMES	20150904T0156	HERMES
	20150904T2100	HERMES	20150904T2104	HERMES	20150904T2157	HERMES
	20150904T2310	HERMES	20150904T2315	HERMES	20150905T0239	HERMES
	20150905T2111	HERMES	20150905T2116	HERMES	20150905T2231	HERMES
	20150905T2236	HERMES	20150905T2347	HERMES	20150905T2352	HERMES
	20150906T2117	HERMES	20150906T2122	HERMES	20150906T2248	HERMES
	20150906T2253	HERMES	20150907T0053	HERMES	20150907T0058	HERMES
	20160712T0134	HERMES				
HD 213617 (177)	20160712T0307	HERMES	20160713T0344	HERMES	20160714T0221	HERMES
	20160715T0330	HERMES	20160717T0146	FIES	20160717T0354	FIES
	20160718T0144	FIES	20160719T0211	FIES	20160720T0325	FIES
HD 217782 (526)	20150903T2114	HERMES	20150903T2208	HERMES	20150903T2318	HERMES
	20150904T0232	HERMES	20150904T2114	HERMES	20150904T2120	HERMES
	20150904T2205	HERMES	20150904T2212	HERMES	20150904T2323	HERMES
	20150904T2329	HERMES	20150905T2124	HERMES	20150905T2130	HERMES
	20150905T2259	HERMES	20150905T2305	HERMES	20150906T0103	HERMES
	20150906T0108	HERMES	20150906T0431	HERMES	20150906T2130	HERMES
	20150906T2136	HERMES	20150906T2318	HERMES	20150906T2324	HERMES
	20150907T0233	HERMES	20150907T0239	HERMES	20151222T1949	HERMES
	20151222T2005	HERMES	20151223T2044	HERMES	20160712T0030	HERMES
	20160712T0413	HERMES	20160713T0143	HERMES	20160713T0432	HERMES
	20160714T0206	HERMES	20160714T0358	HERMES	20160715T0240	HERMES
	20160717T0108	FIES	20160717T0312	FIES	20160718T0126	FIES
	20160718T0336	FIES	20160719T0129	FIES	20160719T0335	FIES
	20160720T0151	FIES	20160720T0405	FIES		
HD 221756 (326)	20151222T2302	HERMES	20151223T2212	HERMES	20151223T2354	HERMES
	20151224T0034	HERMES	20160130T1926	HERMES	20160130T1943	HERMES
	20160712T0057	HERMES	20160713T0158	HERMES	20160713T0445	HERMES
	20160714T0316	HERMES	20160714T0515	HERMES	20160715T0152	HERMES
	20160715T0508	HERMES	20160717T0120	FIES	20160717T0321	FIES
	20160718T0135	FIES	20160718T0345	FIES	20160719T0138	FIES
	20160719T0350	FIES	20160720T0139	FIES	20160720T0414	FIES
HD 222368 (335)	20160712T0330	HERMES	20160713T0210	HERMES	20160713T0459	HERMES
	20160714T0330	HERMES	20160715T0232	HERMES	20160717T0247	FIES
	20160717T0455	FIES	20160718T0219	FIES	20160718T0443	FIES
	20160719T0154	FIES	20160719T0439	FIES	20160720T0348	FIES
HD 224392 (280)	20151023T0108	FEROS	20151023T0444	FEROS	20151024T0437	FEROS
	20170923T0446	FEROS	20170924T0146	FEROS	20170925T0649	FEROS
	20170925T0658	FEROS				